UC San Diego

UC San Diego Electronic Theses and Dissertations

Title

Improving Understanding of Earthquake Source Mechanics through Stress Drop and High-Frequency Radiation Content Analysis

Permalink

https://escholarship.org/uc/item/0wh4d8vp

ISBN

9798173720979

Author

Vandevert, Ian

Publication Date

2026-10-30

Peer reviewed|Thesis/dissertation

eScholarship.org Powered by the California Digital Library
University of California

UNIVERSITY OF CALIFORNIA SAN DIEGO

Improving Understanding of Earthquake Source Mechanics through Stress Drop and High-Frequency Radiation Content Analysis

A dissertation submitted in partial satisfaction of the
requirements for the degree
Doctor of Philosophy

in

Earth Sciences

by

Ian Vandevert

Committee in charge:

Professor Peter M. Shearer, Co-Chair
Professor Wenyuan Fan, Co-Chair
Professor Alice-Agnes Gabriel
Professor Ahmed Elgamal

2026

Copyright

Ian Vandevert, 2026

All rights reserved.

The Dissertation of Ian Vandevert is approved, and it is acceptable in quality and form for publication on microfilm and electronically.

University of California San Diego

2026

DEDICATION

To my mother and grandmother

EPIGRAPH

And no one showed us to the land
And no one knows the where's or why's
But something stirs and something tries
And starts to climb toward the light

Echoes, Pink Floyd

Science is a way of thinking much more than it is a body of knowledge.

Carl Sagan

If my words did glow with the gold of sunshine
And my tunes were played on the harp unstrung
Would you hear my voice come through the music?
Would you hold it near as it were your own?

Ripple, Grateful Dead

TABLE OF CONTENTS

Dissertation Approval Page . . . iii

Dedication . . . iv

Epigraph . . . v

Table of Contents . . . vi

List of Figures . . . viii

List of Tables . . . x

Acknowledgements . . . xi

Vita . . . xiv

Abstract of the Dissertation . . . xv

Chapter 1 Introduction . . . 1

Chapter 2 Ridgecrest Aftershock Stress Drops from P- and S-Wave Spectral Decomposition . . . 9
2.1 Introduction . . . 9
2.2 Data . . . 11
2.3 Methods . . . 13
2.3.1 P-wave Analysis . . . 16
2.3.2 S-wave Analysis . . . 18
2.4 Results . . . 19
2.5 Discussion . . . 23
2.5.1 Spatial Variation of Source Parameters . . . 28
2.6 Conclusions . . . 31
2.7 Data Availability and Resources . . . 31
2.8 Supplementary Materials . . . 33

Chapter 3 Using a High- to Low-Frequency Spectral Ratio to Distinguish Variations in Earthquake Source Properties . . . 41
3.1 Introduction . . . 41
3.2 Data . . . 43
3.3 Methods . . . 44
3.3.1 Uncertainty Quantification . . . 49
3.4 Results . . . 50
3.5 Discussion . . . 54
3.5.1 Relation between nFI and Stress-Drop Estimates . . . 54
3.5.2 nFI and Frequency Index . . . 59

3.5.3 Synthetic Experiments and Uncertainty 61
3.5.4 Parameter Choices 64
3.6 Conclusions 66
3.7 Data Availability and Resources 67
3.8 Supplementary Materials 68

Chapter 4 Distinguishing Spatial Variations in California Earthquake Dynamics Using a High- to Low-Frequency Spectral Ratio 70
4.1 Introduction 70
4.2 Data 72
4.2.1 Station Gain Changes 75
4.3 Methods 75
4.4 Results 79
4.4.1 Stress drop comparison 81
4.4.2 Hypocentral depth 82
4.4.3 Focal mechanism 82
4.4.4 Heat flow 84
4.4.5 Spatial variation 85
4.5 Discussion 85
4.5.1 nFI in geothermal regions 87
4.5.2 Ridgecrest sequence 89
4.5.3 Hector Mine sequence 91
4.5.4 Central San Andreas Fault 93
4.5.5 Temporal variation 95
4.5.6 Other possible sources of variation 96
4.6 Conclusions 97
4.7 Data Availability Statement 98

Chapter 5 Conclusion 100

Bibliography 104

LIST OF FIGURES

Figure 2.1. Map of Ridgecrest seismicity and seismic stations 12

Figure 2.2. Signal-to-noise for P and S records 13

Figure 2.3. Magnitude versus estimated seismic moment 17

Figure 2.4. S-wave versus P-wave M_0 and $\Delta\sigma$ 20

Figure 2.5. Corner frequency versus M_0 21

Figure 2.6. Magnitude scaling of $\Delta\sigma$ for varying n 22

Figure 2.7. Maps of Ridgecrest P-wave and S-wave $\Delta\sigma$ 24

Figure 2.8. Cross sections of $\Delta\sigma$ 25

Figure 2.S1. Example waveforms and their spectra from spectral decomposition . 34

Figure 2.S2. Spectral decomposition example 35

Figure 2.S3. Empirical correction spectrum computation example 36

Figure 2.S4. Temporal plot of stress drop vs. time 37

Figure 2.S5. Correlation between P and S wave results 38

Figure 2.S6. Correlation between P and S wave results in cross section 39

Figure 2.S7. Stress drop comparison to various slip models 40

Figure 3.1. Map of Ridgecrest seismicity and dataset (4–18 July 2019) 45

Figure 3.2. $\log\beta$ computation example 46

Figure 3.3. Corrections process from $\log\beta$ to nFI 51

Figure 3.4. S-wave versus P-wave nFI 52

Figure 3.5. Maps of Ridgecrest nFI and $\Delta\sigma$ 53

Figure 3.6. Relationships between f_c and $\Delta\log\beta$, and $\Delta\sigma$ and nFI 56

Figure 3.7. Synthetic corrections process from $\log\beta$ to nFI 63

Figure 3.8. Synthetic $\Delta\log\beta$ scaling relationship with magnitude 64

Figure 3.S1. Stress drop vs. nFI comparison for different frequency bands (P-waves) 68

Figure 3.S2. Stress drop vs. nFI comparison for different frequency bands (S-waves) 68

Figure 3.S3. Stress drop vs. nFI comparison for many different studies 69

Figure 4.1. Map of California seismicity and dataset (1995–2024) 73

Figure 4.2. $\log \beta$ computation example 77

Figure 4.3. Corrections process from $\log \beta$ to nFI 78

Figure 4.4. California nFI for different event types 80

Figure 4.5. California nFI versus stress drop 81

Figure 4.6. California nFI versus hypocentral depth 82

Figure 4.7. California nFI versus focal mechanism 83

Figure 4.8. California nFI versus surface heat flow 85

Figure 4.9. nFI in three geothermal regions 88

Figure 4.10. nFI near the Long Valley Caldera 88

Figure 4.11. nFI of the Ridgecrest sequence, map and cross sections 90

Figure 4.12. nFI of the Hector Mine sequence, map and cross sections 92

Figure 4.13. nFI of the central San Andreas Fault, map and cross section 94

LIST OF TABLES

Table 2.1. Ridgecrest spectral decomposition parameters 19

ACKNOWLEDGEMENTS

During my time at IGPP, I have been lucky to work with some of the best researchers in seismology and geophysics. I am especially grateful to my advisors, Peter Shearer and Wenyuan Fan. Peter is a seemingly endless source of knowledge. His door is always open, and he provides supportive and constructive comments on whatever questions I bring, however disorganized they are. Thanks to him and Wenyuan, I was able to attend many conferences and meet hundreds of people from all over the world in seismology and related fields. Early on in my PhD program, I realized that apparently everyone in seismology has some connection to Peter – whether they were his graduate student, a student of one of his graduate students, or a coauthor. Because of this, it felt as if I was joining a kind of "academic family", which made collaboration at conferences much less daunting. I will be forever grateful to him for his mentoring and guidance.

Wenyuan was also a graduate student of Peter's, so it makes sense that he has a similar advising style: he always makes time for his students, is insightful, and obviously cares about us. He is also a master at presenting science. I remember, early on, bringing Wenyuan a very rough set of slides for an upcoming presentation. Although I was stressed about their initial condition, he helped me turn them into something clear and professional in a short time. I became a confident presenter during my time at IGPP mainly thanks to Wenyuan, to whom I will alway be grateful. He has earned many awards, but in my opinion deserves many more.

The ongoing Community Stress Drop Validation Study began in 2021, so my entire PhD journey has paralleled this collaboration. The two people that organized the various workshops, group meetings, and various projects are Rachel Abercrombie and Annemarie Baltay. Rachel has a deep understanding of all things relating to earthquake source mechanics, while being kind and supportive. The highlights of the many conferences we attended together were when she stopped by my poster or talk to understand my recent work and share her insights. Annemarie also brings vast expertise, and my research

improved because of her constructive comments. She also seems to know everyone, and I am grateful that she introduced me to countless people when I was a new conference-goer.

Our 2021 cohort was the largest in IGPP's history, beginning during an uncertain time of Zoom lectures and meetings. Anupam, Chance, Evan, Guilherme, Jeena, Jeremy, John, Matt, Nicolas, Ray, Rebecca, and Xiaoyu — you're all great scientists, and I'm looking forward to seeing where you go next. While we began at different times, I am also grateful to Taiga and Yonatan for their friendship.

To the people at NetOps: thank you for always keeping things running smoothly. And to Christine, Sofia, and the others in administration: thank you for dealing with my confusion and struggles with expense reports.

I wouldn't be here without the many great, enthusiastic teachers and professors I've been lucky enough to learn from over the years. There are too many to thank fully here, but I am especially grateful to: Larry Newberry, for clearly explaining difficult mathematics with a sense of humor; Maziar Afshar, who made physics approachable; Francisco Gago, who introduced me to field work; John Gerz, who made graduate school seem attainable; and Toshiro Tanimoto and Robin Matoza, who both introduced me to seismology.

And of course, I am grateful to my family, who made this possible. To my mother, who has always believed in me. She encouraged my inclination towards science from a young age – helping me do "science experiments" with household items, and teaching me the value of education. To Mike and Joanne, who helped motivate me toward higher education and pushed me to achieve it. And finally, to Kim and Dave, for being a constant source of support.

Lastly, I am grateful to my partner Erica, for being supportive even when I had little time to spare. And of course, to our dog Daisy for her infinite love.

This dissertation consists of two papers that have been published, and one that has been submitted for publication. The dissertation author was the primary investigator and author of each of the three papers.

Chapter 2, in full, is a reprint of the material as it appears in *Bulletin of the Seismological Society of America*. Vandevert, I. C., Shearer, P. M., & Fan, W. (2025). Ridgecrest Aftershock Stress Drops from P- and S-Wave Spectral Decomposition. *Bulletin of the Seismological Society of America*, 115(3), 792-804. https://doi.org/10.1785/0120240133.

Chapter 3, in full, is a reprint of the material as it appears in *Bulletin of the Seismological Society of America*. Vandevert, I., Shearer, P. M., & Fan, W. (2026). Using a High- to Low-Frequency Spectral Ratio to Distinguish Variations in Earthquake Source Properties. *Bulletin of the Seismological Society of America* (Early Access). https://doi.org/10.1785/0120250171.

Chapter 4, in full, is a reproduction of the material submitted to *Journal of Geophysical Research: Solid Earth*. Vandevert, I., Shearer, P. M., & Fan, W. (2026). Distinguishing Spatial Variations in California Earthquake Dynamics Using a High- to Low-Frequency Spectral Ratio.

VITA

2021–2026 Ph. D. in Earth Sciences, University of California San Diego

2016–2019 B. S. in Earth Science, University of California Santa Barbara

PUBLICATIONS

I. Vandevert, P. M. Shearer, and W. Fan, "Distinguishing Spatial Variations in California Earthquake Dynamics Using a High- to Low-Frequency Spectral Ratio", *Journal of Geophysical Research: Solid Earth* [submitted], 2026.

I. Vandevert, P. M. Shearer, and W. Fan, "Using a High- to Low-Frequency Spectral Ratio to Distinguish Variations in Earthquake Source Properties", *Bulletin of the Seismological Society of America*, doi: 10.1785/0120250171, 2026.

R. E. Abercrombie, A. Baltay, S. Chu, [...], **I. Vandevert**, [...], "Overview of the SCEC/USGS Community Stress Drop Validation Study using the 2019 Ridgecrest Earthquake Sequence", *Bulletin of the Seismological Society of America*, 115(3), 734–759, doi: 10.1785/0120240158, 2025.

P. M. Shearer, **I. Vandevert**, W. Fan, R. Abercrombie, D. Bindi, G. Calderoni, X. Chen, W. Ellsworth, R. Harrington, and Y. Huang, "Earthquake Source Spectra Estimates Vary Widely for Two Ridgecrest Aftershocks Because of Differences in Attenuation Corrections", *Bulletin of the Seismological Society of America*, 115(3), 777–791, doi: 10.1785/0120240134, 2024.

I. C. Vandevert, P. M. Shearer, and W. Fan, "Ridgecrest Aftershock Stress Drops from P- and S-Wave Spectral Decomposition", *Bulletin of the Seismological Society of America*, 115(3), 792–804, doi: 10.1785/0120240133, 2024.

ABSTRACT OF THE DISSERTATION

Improving Understanding of Earthquake Source Mechanics through Stress Drop and High-Frequency Radiation Content Analysis

by

Ian Vandevert

Doctor of Philosophy in Earth Sciences

University of California San Diego, 2026

Professor Peter M. Shearer, Co-Chair
Professor Wenyuan Fan, Co-Chair

Earthquakes produce damaging ground motions generally increasing with their size, or moment. Moment reflects the low-frequency energy that an earthquake radiates, but earthquakes of similar moment can produce very different amounts of high-frequency shaking that is destructive to infrastructure. Stress drop, the change in average shear stress across a fault due to a rupture, is a geophysical parameter often used to quantify this variation. For earthquakes without surface rupture or deformation, stress drop must be inferred from the earthquake's radiated waves. This inference requires assumptions about rupture models, attenuation models, and signal-processing parameter choices, such

that studies using similar methods can differ by an order of magnitude or more in their estimates of the same event. Relative stress drop between events is better constrained, and can reveal robust spatial variations in high-frequency content, but is still susceptible to bias due to model and parameter assumptions. The normalized frequency index (nFI) is an alternative measure of the relative amount of high-frequency radiation, computed directly from observed spectra and corrected empirically for path, station, and magnitude effects. The nFI requires fewer assumptions and is simpler to compute, especially for large datasets, yet still correlates with stress drop. Determining spatial patterns in high-frequency radiation content has direct implications for improving seismic hazard models.

In Chapter 2, we compute stress drops from P- and S-wave spectra of the 2019 Ridgecrest earthquake sequence.

In Chapter 3, we develop the normalized frequency index, which quantifies the variation in high-frequency radiation. We apply this method to the same dataset as in Chapter 2.

In Chapter 4, we compute the normalized frequency index for 30 years of California seismicity, explore its spatial variation, and compare it to several geophysical parameters.

Finally, Chapter 5 discusses conclusions and possible future work.

Chapter 1

Introduction

Earthquakes are among the most destructive types of natural disasters in modern times. Between 1980 and 2009, *Doocy et al.* (2013) estimated that over 61 million people were directly affected by earthquakes, including over 350,000 killed and nearly 1 million injured. Earthquakes cannot be predicted and while earthquake early warning systems can help protect lives and infrastructure by providing seconds to minutes of warning before damaging waves arrive, they trigger only after the first seismic waves are detected. Limiting earthquake risk before an event occurs instead requires characterizing where seismic hazard is concentrated (e.g. *Wesnousky*, 1986; *Field et al.*, 2014). Understanding the mechanics of how earthquakes rupture is crucial for refining seismic hazard maps.

The size of an earthquake is often quantified by its magnitude (M). Events smaller than about M3 are generally not felt by humans, while those above about M5.5 begin to cause significant damage. While large earthquakes are typically more damaging, smaller earthquakes are far more common; for each unit decrease in magnitude, the number of events increases by roughly a factor of 10 (*Richter*, 1935; *Utsu*, 2002b). Events smaller than M1 are routinely detected by seismic networks, so any regional earthquake catalog will be dominated by smaller events. Several different earthquake magnitude scales exist, but all are roughly connected to the local magnitude (M_L), an empirical scale introduced by *Richter* (1935) and colloquially known as the Richter scale, which remains common

in news and media coverage of earthquakes. It is related to peak observed seismogram amplitudes and is simple to compute, but has no direct physical interpretation and is prone to saturation, an effect that causes an underestimation of magnitude for large events (*Hanks and Kanamori*, 1979).

A better-defined measure of earthquake size is the scalar seismic moment (M_0), which relates earthquake size directly to rupture geometry:

$$M_0 = \mu A \overline{D} \tag{1.1}$$

where μ is the shear modulus, A is the fault area, and $\overline{D}$ is the average fault displacement. From the seismic moment, *Kanamori* (1977) and *Hanks and Kanamori* (1979) derived the moment magnitude (M_W),

$$M_W = \frac{2}{3}[\log_{10} M_0 - 9.1]. \tag{1.2}$$

Because M_W is based on seismic moment rather than peak shaking, it does not saturate and can describe an earthquake of any size. It is designed to agree approximately with the local magnitude scale for earthquakes $3 \leq M_L \leq 7$. For large earthquakes, M_0, and therefore M_W can be measured accurately from surface displacements, geodetic data, and long-period waves. For small earthquakes without geodetic constraints, estimating M_W is typically done using the long-period spectral level.

While magnitude describes the size of an event, earthquakes of the same magnitude can produce different amounts of high-frequency damaging ground motion. Some of this variation is related to station location with respect to the source, i.e., arising from the radiation pattern of a double-couple source or from directivity. However, some variation reflects actual differences in the average properties of the source radiation, which could arise from rupture dynamics and slip geometry. Moment magnitude alone cannot capture these differences. Because of tradeoffs between A and $\overline{D}$ (Equation 1.1), M_W does not

distinguish large slip on a small fault from small slip on a large fault, even though the two radiate different amounts of high-frequency energy. Characterizing source variability commonly falls to the earthquake stress parameter, or stress drop ($\Delta\sigma$), which is the average change in shear stress across a fault due to an earthquake. Higher $\Delta\sigma$ corresponds to relatively more high-frequency energy in an earthquake's spectrum.

For a circular fault of radius r, *Eshelby* (1957) derived

$$\Delta\sigma = \frac{7\pi\mu\overline{D}}{16r} = \frac{7M_0}{16r^3}, \tag{1.3}$$

where the second equality follows from Equation 1.1. This relation connects $\Delta\sigma$ to the rupture dimension (r for a circular rupture). For sufficiently large earthquakes, r can be constrained directly from geodetic data, so $\Delta\sigma$ follows from Equation 1.3. For smaller earthquakes where r is not directly observable, $\Delta\sigma$ must be inferred from the radiated seismic waves alone.

Brune (1970) introduced a model, now widely used, for the shape of the radiated far-field displacement spectrum, which has the form

$$u(f) = \frac{\Omega_0}{1 + (f/f_c)^n}, \tag{1.4}$$

where Ω_0 is the long-period spectral level, which is proportional to M_0, n is the high-frequency falloff rate ($n = 2$ for the standard Brune model), and f_c is the corner frequency. The corner frequency is the frequency at which the spectrum transitions from the flat long-period level to its high-frequency decay rate of f^{-n}. On average, observed spectra are well approximated by Brune spectra (e.g. *Abercrombie*, 1995; *Shearer et al.*, 2006). However, variations in how Equation 1.4 is fit to individual spectra greatly influences Ω_0 and f_c estimates, which in turn influence $\Delta\sigma$.

Dynamic rupture simulations connect the displacement spectrum of an earthquake

(Equation 1.4) to its stress drop (Equation 1.3). *Madariaga* (1976) was the first to derive the relation between f_c and r from a dynamic simulation of a circular expanding fault, and later studies have developed more sophisticated models (e.g., *Kaneko and Shearer*, 2014). Because such simulations specify the rupture geometry and stress drop, they predict the P and S waveforms and spectra that would be observed under idealized conditions with no path effects or attenuation. These rupture simulations relate the fault rupture dimension to the resulting spectrum's f_c, and allow $\Delta\sigma$ to be estimated:

$$\Delta\sigma = \frac{7}{16}\left(\frac{\overline{f}_c}{k\beta}\right)^3 M_0, \tag{1.5}$$

where $\overline{f}_c$ is the spherically-averaged corner frequency to average out azimuthal variations, β is the shear wave speed, and k is a parameter that depends on both the rupture model and seismic phase. Models generally predict a higher f_c for P-waves than for S-waves, so P-wave k values are lower than those for S-waves.

A complication in computing spectral stress drop is that the observed spectrum is a function of source, path, and station effects. This is generally modeled as a convolution in the time domain, or a product in the frequency domain. In logarithmic amplitude, it becomes a sum of log terms:

$$D(f) = E(f) + P(f) + S(f) \tag{1.6}$$

where $D(f)$ is the observed log spectrum; $E(f)$ is the event term representing source variability; $P(f)$ is the propagation term, which includes heterogeneity along the raypath, attenuation, and geometric spreading; and $S(f)$ is the station term representing station-specific effects, including near-site effects and instrument response. Recovering the event term $E(f)$, which carries the source information, therefore requires separating it from the path and station terms. This can be done using the empirical Green's function (EGF) or

spectral ratio method, where the spectra of colocated events are divided to cancel their shared path and station terms (e.g., *Mueller*, 1985; *Hough*, 1997; *Abercrombie et al.*, 2017; *Shimmoto*, 2022).

Another approach to extracting the event term from Equation 1.6 is to apply spectral decomposition, which is an empirical method to separate path and station effects from observed spectra (e.g. *Andrews*, 1986; *Shearer et al.*, 2006; *Oth et al.*, 2011; *Trugman*, 2020). The observed spectra are cast as an inverse problem that extends Equation 1.6:

$$d_{ij} = e_i + t_{k(i,j)} + s_j + r_{ij}, \tag{1.7}$$

where, for event i and station j, d_{ij} is the observed log displacement spectrum, e_i is the event term, s_j is the station term, $t_{k(i,j)}$ is the propagation term for ray path k between event i and station j, and r_{ij} is the residual term. The solution to Equation 1.7 is non-unique; for a pair of terms on the right side of the equation, a constant could be added to one and subtracted from the other without affecting d_{ij}. This ambiguity can resolved in different ways (e.g., *Andrews*, 1986; *Shearer et al.*, 2006; *Oth et al.*, 2011; *Trugman and Shearer*, 2017a; *Bindi et al.*, 2020a), all of which require making assumptions about the source or path properties that cannot be obtained directly from the data.

The last several decades have produced numerous stress-drop studies based on spectral decomposition, spectral ratio, and other methods. One common theme is that stress drop estimates are highly uncertain; even studies that use the same technique and dataset often produce stress drop estimates that differ by orders of magnitude. The Community Stress Drop Validation Study (*Baltay et al.*, 2024; *Abercrombie et al.*, 2025a) was designed to quantify this uncertainty by aggregating corner frequency and stress drop estimates from independent groups using a range of techniques on the Ridgecrest aftershock sequence. It is becoming clear that observational approaches to correcting attenuation and estimating $\Delta\sigma$ are unstable, and typically suffer too many parameter

tradeoffs to yield reliable results (*Shearer et al.*, 2019). The validation study also found, however, that although absolute $\Delta\sigma$ estimates are inconsistent between studies, relative $\Delta\sigma$ was consistent for M$\geq$ 2.5 earthquakes, in agreement with earlier work (*Shearer et al.*, 2019; *Pennington et al.*, 2021). Absolute $\Delta\sigma$ may therefore be unreliable, but whether an earthquake has higher- or lower-than-average $\Delta\sigma$ can still be resolved.

Informed by these insights, *Shearer et al.* (2022) developed a type of P-wave spectral decomposition which assumes a fixed corner frequency for small earthquakes near each target event. This eliminates the possibility of resolving the absolute level of stress drop for small earthquakes but has the advantage of stabilizing the spectral decomposition approach and ensuring that any observed spatial variations in larger earthquake stress drops are real and not an artifact of inaccurate path corrections. Chapter 2, in its entirety, is a reprint of *Vandevert et al.* (2024), which applies a similar spectral decomposition technique to the 2019 Ridgecrest aftershock sequence and extends the method to include both P and S waves.

Stress drop has long been used to quantify variability of earthquake high-frequency radiation, but it does so indirectly and imprecisely. Alternate methods of measuring earthquakes by their high-frequency radiation have some precedent, but have not been widely adopted. For example, noting the problems with stress drop, *Atkinson and Hanks* (1995) and *Atkinson and Beresnev* (1997) proposed a magnitude scale based on the high-frequency acceleration spectral level, as this is more closely related to ground motions. Building upon these ideas, we developed the normalized frequency index (nFI), a parameter that directly quantifies an earthquake's relative of high-frequency content. nFI requires no assumed spectral shape or rupture model, and removes path and station effects empirically rather than through an attenuation model. Although nFI is not intended as a proxy for $\Delta\sigma$, it correlates with previous stress drop estimates, indicating that it captures the relative high-frequency variation with fewer assumptions and using only the observed data.

Chapter 3, in its entirety, is a reprint of *Vandevert et al.* (2026). We computed P-

and S-wave nFI for the 2019 Ridgecrest aftershock sequence (*Baltay et al.*, 2024) and analyzed its spatial variation, depth dependence, and correlation with stress drop. We also conducted synthetic tests to characterize nFI's sensitivity to parameter changes. We found that nFI exhibited spatial variations consistent with $\Delta\sigma$ from *Vandevert et al.* (2024), and also consistent with the many other groups in the *Abercrombie et al.* (2025a) review of results for the Ridgecrest validation exercise. In addition, P- and S-wave nFI computed independently correlate well without any parameter tuning.

Chapter 4 extends the nFI method to seismicity across California over a 30-year period (1995–2024). Whereas Chapter 3 examined a single aftershock sequence, this study produces the first statewide characterization of high-frequency source variability, taking advantage of California's dense network coverage and diverse tectonic settings. We map the spatial distribution of nFI at regional and local scales and test whether it correlates with other geophysical properties, such as focal mechanism, heat flow, hypocentral depth, and timing of last slip on a fault. We find that nFI is lower in regions with high heat flow and geothermal features. We observe a small increase in nFI with depth and a decrease with the timing of last slip. Our results show that nFI resolves coherent, spatial variations in relative high-frequency earthquake radiation, and suggests its relevance for regional ground-motion and seismic hazard models.

Earthquakes of similar magnitude produce differing amounts of damaging high-frequency ground motion. The following chapters of this dissertation show that some of this variation is spatially coherent and correlates with other geophysical parameters, indicating that it reflects real differences in the earthquake source rather than measurement scatter or some processing artifact. Stress drop, the parameter most widely used to quantify this variation, has high uncertainty and is limited by the assumed spectral and rupture models it depends on. nFI offers a more direct, data-driven alternative, one that resolves these patterns without the modeling assumptions that can bias stress drop estimates. Understanding this variability and incorporating it into ground-motion and seismic hazard

models is a promising direction for reducing earthquake risk before an event occurs.

Chapter 2

Ridgecrest Aftershock Stress Drops from P- and S-Wave Spectral Decomposition

2.1 Introduction

Stress drop reveals earthquake rupture dynamics and faulting conditions and correlates with the associated strong ground motions (*Hanks and McGuire*, 1981; *Shearer et al.*, 2006; *Trugman and Shearer*, 2018). However, reliably obtaining stress drop for small earthquakes (M<5.5) is challenging, due to limitations in observations and an imperfect understanding of the Earth structure and earthquake rupture processes (*Abercrombie*, 2021; *Hardebeck*, 2020). In practice, stress drops of small earthquakes are often estimated in the frequency domain by fitting a theoretical model to the earthquake's source spectrum (e.g. *Prieto et al.*, 2004), which is obtained from observations after removing path effects, including attenuation and the near-surface site response. There are many theoretical models of the source spectrum, but they are all idealized and based on simple fault geometries and homogeneous slip, such as the Brune (*Brune*, 1970) and Boatwright (*Boatwright*, 1980) models. Both the model assumptions and the source-spectrum measurement procedure can introduce errors in stress-drop estimates (e.g., *Abercrombie*, 2021), and stress-drop estimates of similar-sized earthquakes can differ by up to three orders of magnitude (e.g.,

Allmann and Shearer, 2009). This large uncertainty hinders progress in resolving the true rupture variability and faulting conditions of earthquakes, consequently affecting hazard mitigation and risk assessment.

Various empirical approaches have been developed to remove path effects from seismic records to resolve the source spectrum (e.g. *Shearer et al.*, 2006; *Huang et al.*, 2016). Some approaches explicitly solve for a path term, while others use records of smaller, adjacent earthquakes to approximate the path term, which can cause differences in stress-drop estimates for the same earthquakes (e.g. *Shearer et al.*, 2019). Stress-drop estimates also differ when using different data types, such as P- and S-waves (*Trugman*, 2020; *Bindi et al.*, 2021), and different choices for the theoretical model can introduce additional variations in the estimates (e.g., *Cotton et al.*, 2013; *Fan and McGuire*, 2018). In general, P-wave spectra have good signal-to-noise extending to higher frequencies than S waves, allowing better resolution of high-frequency falloff rates and small-earthquake corner frequencies. S-wave spectra suffer from contamination from P coda, especially at closer distances, but typically have higher amplitudes, making them more directly related to strong ground motion measures (e.g., peak velocity) and earthquake moment estimates. To systematically investigate stress-drop estimate differences observed in different studies, the Ridgecrest stress drop validation study (*Baltay et al.*, 2024) aims to identify the sources of variability and quantify the uncertainty in earthquake stress drops by comparing results from different groups using a common set of data and earthquakes.

Here we contribute to the Ridgecrest validation exercise by applying the spectral decomposition method (*Shearer et al.*, 2006; *Trugman and Shearer*, 2017a) to both P- and S-waves for the same set of earthquakes and comparing the results step by step. Our specific approach has the advantage of resolving relative differences between estimates of larger earthquakes by fixing the corner frequencies of the smallest earthquakes in the analysis (*Shearer et al.*, 2022; *Ruhl et al.*, 2023). We examine our P- and S-wave stress-drop estimates as a function of magnitude and location, as well as the associated

source parameters such as seismic moment, corner frequency, and high-frequency falloff rate. We find that our average stress-drop estimates from P and S waves can be brought into approximate agreement through careful selection of the S-wave small-earthquake corner frequency and high-frequency falloff rate. The two sets of estimates share similar relative differences within each group and their spatial distributions are highly correlated, regardless of parameter choices.

2.2 Data

We participate in the Community Stress Drop Validation Study (*Baltay et al.*, 2024) and use the common dataset of the 2019 Ridgecrest earthquake sequence to estimate stress drops. The dataset includes both a relocated earthquake catalog and the associated waveforms, curated from the Southern California Earthquake Data Center (*Trugman*, 2020; *SCEDC*, 2013). We analyze 12,943 earthquakes with magnitudes (M) greater than 1, occurring between 4 and 18 July 2019 (Fig. 2.1), including the M 6.4 foreshock on 4 July and M 7.1 mainshock on 5 July. These earthquakes occurred within latitudes of 35.5° to 36.0° and longitudes of -117.75° to -117.33°. The earthquakes have different catalog magnitude types (Fig. 2.1; *SCEDC*, 2013); 120 M>3.3 earthquakes are assigned moment magnitude (M_W) and the remaining events have local magnitude (M_L). The P- and S-waveforms are from 61 seismic stations in the area. For the events of interest, we use three-component velocity records (EH and HH), sampled at 100 Hz, within one degree of epicentral distance to estimate their source parameters. Records with different sampling rates are resampled at 100 Hz. We use vertical components for the P-wave analysis and horizontal components for the S-wave analysis. The number of records that are eventually used to estimate stress drops is shown in Fig. 2.2. For P-waves, the median number of records per event is about 10 for M<2 earthquakes and 20 for M>2 earthquakes. For S-waves, the median number of usable records is about 20 for M>2 earthquakes (Fig. 2.2).

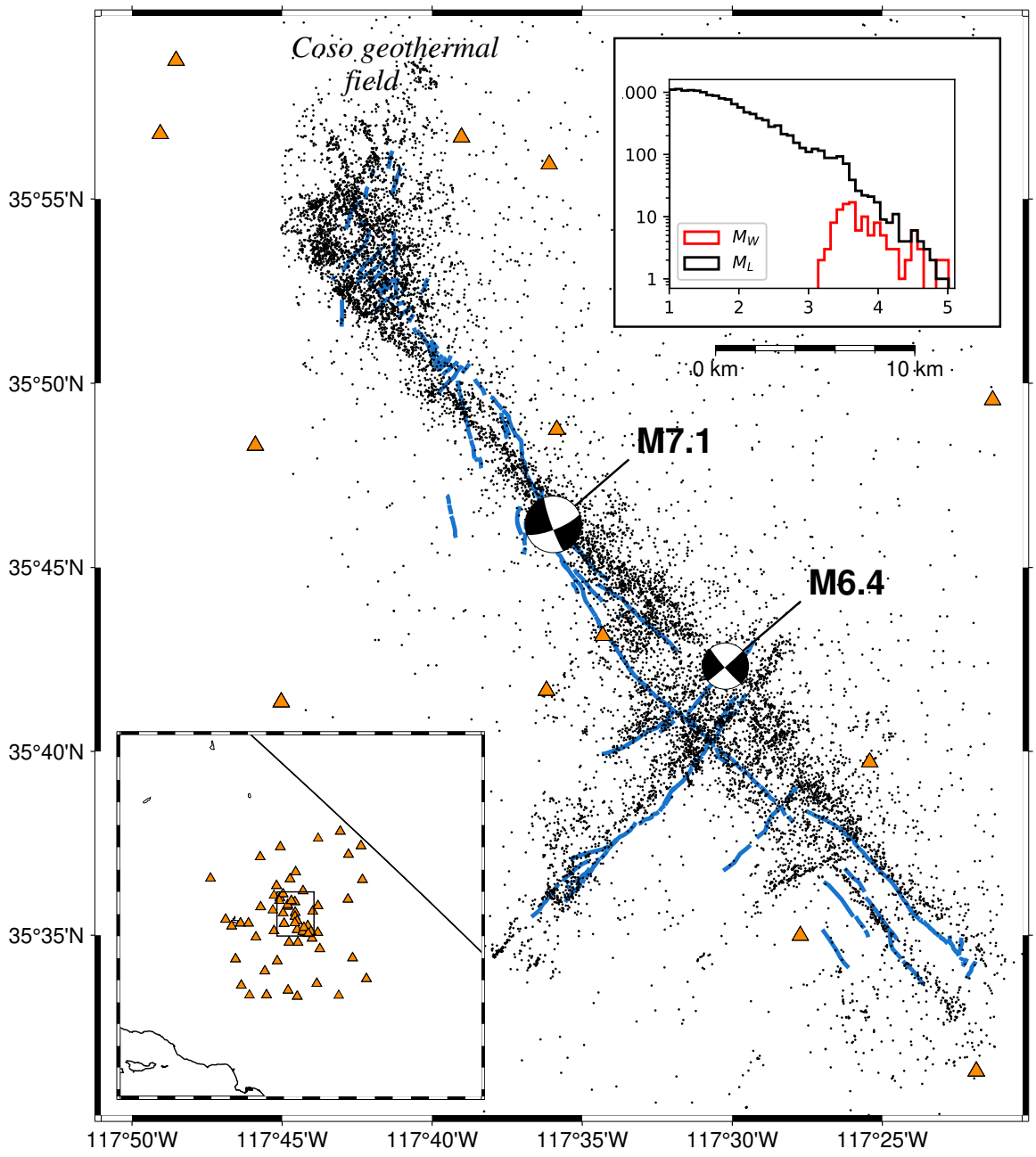


Figure 2.1. Spatial distribution of 12,943 events (black dots) in the 2019 Ridgecrest Earthquake Sequence dataset (*Baltay et al.*, 2024), the 61 nearby seismic stations (orange triangles), and the focal mechanisms of the two largest events from *SCEDC* (2013): the M7.1 mainshock and a M 6.4 foreshock. Blue fault traces are from *DuRoss et al.* (2020). The upper-right inset shows the magnitude distribution of the events below M 5. The lower-left inset shows the greater southern California region with all seismic stations used in this study, as well as the spatial extent of the main figure.

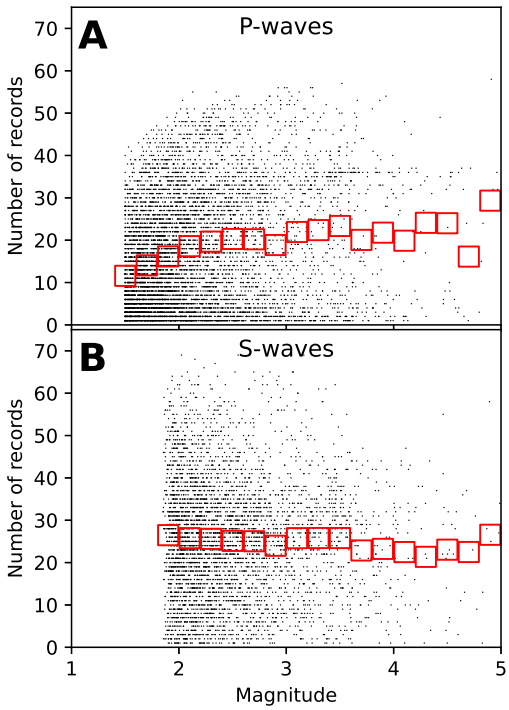


Figure 2.2. Number of records passing station-to-noise requirements used in spectral decomposition versus catalog magnitude for both P-waves (panel A) and S-waves (panel B). Red squares show binned medians for bin widths of M 0.2.

2.3 Methods

We apply a spectral decomposition method (*Shearer et al.*, 2022) to compute the earthquake source spectra and infer their source parameters, including corner frequency (f_c), scalar seismic moment (M_0), and stress drop ($\Delta\sigma$). We first compute the Fourier spectrum of the P- or S-wave record at each station, with a signal window starting 0.15 s before the phase arrival. The window length is 1.28 s for M$\leq$3.28 earthquakes and 2.56 s for larger events. Since we use a shorter time window than *Shearer et al.* (2022), who used 1.5 s windows for events below M3.4, we also use a lower magnitude cutoff of M3.28. We use catalog phase picks when available and compute the arrival times using the Hadley-Kanamori 1D velocity model for the others (*Hadley and Kanamori*, 1977). We detrend the time series using twice the length of the signal window with the second half as the

signal window and the preceding window defined as the noise window. We apply a Hann taper to the signal window before computing its displacement spectra from the velocity record. We measure the noise level by computing the noise-window Fourier spectrum following the same procedure. For S-wave spectra, the noise window may contain some of the P wavetrain. From the spectra, we compute an average signal-to-noise ratio (SNR) for each record to evaluate the data quality, which is defined as the ratio of the average signal spectrum amplitude to the average noise spectrum amplitude between 2.5 and 6 Hz. Spectra with SNR less than 5 are removed from further analysis. Following *Shearer and Abercrombie* (2021), we do not apply a signal-to-noise ratio requirement at frequencies above 6 Hz to reduce selection bias effects, which may lead to preferentially retaining records from higher stress drop earthquakes. An example of our waveform windowing and spectra computation process is shown in Fig. S1 in the electronic supplement. Although the multitaper approach (*Prieto*, 2022) has been widely used to analyze seismic spectra, we opt to use the Hann taper to avoid over-smoothing the spectra at low frequencies. Examples of multitaper smoothing effects are discussed in *Prieto et al.* (2007) and *Shearer and Abercrombie* (2021).

Using the displacement spectrum, we apply a spectral decomposition method (*Shearer et al.*, 2006) to separate the station and attenuation effects and the earthquake source spectra. The technique models the observed spectrum as a sum of log amplitude terms at each frequency,

$$d_{ij} = e_i + s_j + t_{k(i,j)} + r_{ij}, \tag{2.1}$$

where e_i is the event-specific source term for the ith earthquake containing information about rupture dimension and duration, s_j is the station-specific term for the jth station representing near-station effects and the station response, and d_{ij} is the displacement spectrum for the event-station pair. Here, and in the following sections, we take the

logarithm to be base-10. The travel-time term $t_{k(i,j)}$ is discretized at 1-s travel time intervals (estimated based on the same 1-D velocity model used for computing phase arrival times), the event-station distance, and the event depth. We aim to minimize the residual term r_{ij} using an iterative, robust inversion process to solve for the other terms (*Trugman and Shearer*, 2017a). This is similar to other generalized inversion methods that have been applied to analyze large datasets (e.g., *Oth et al.*, 2011; *Bindi et al.*, 2009), and is applied to all events across the entire study region. Source spectral estimates can be biased by directivity effects and incomplete averaging of spectra over the focal sphere (e.g., *Kaneko and Shearer*, 2014). However, station coverage around the Ridgecrest aftershocks is fairly uniform (see Fig. 2.1) without large azimuthal gaps, enabling us to use all records that meet our selection criteria.

With the formulation (Eqn. 2.1) in spectral decomposition, there are ambiguities between different terms in that a constant function could be added to one term and subtracted from another without changing the fit. This ambiguity can be removed by assuming certain properties for the average source spectra, such as a self-similar Brune source model (*Shearer et al.*, 2006). We use the general source spectral model

$$u(f) = \frac{\Omega_0}{1 + \left(\frac{f}{f_c}\right)^n}, \tag{2.2}$$

where $u(f)$ is the source spectrum, Ω_0 is the zero-frequency spectral level (proportional to $\log \mathrm{M}_0$), n is the high-frequency falloff rate ($n = 2$ for the Brune model), and f_c is the corner frequency. We assume that $M = 1.5 \pm 0.1$ and $M = 2 \pm 0.1$ earthquakes have average corner frequencies of 30 Hz and 17 Hz for P- and S-waves respectively, and use differences between their modeled spectra and the observations to estimate the empirical correction spectrum (ECS) that can be added to the event terms to resolve the ambiguities in Eqn. 2.1 (*Shearer et al.*, 2006, 2022).

The assumed average corner frequencies for the small magnitude calibration earth-

quakes are guided by the borehole seismometer results in *Abercrombie* (1995), which sample below the highly attenuating near-surface layers. By fixing small earthquake corner frequencies in this way, we reduce the number of unknowns and stabilize the inversion. Following *Shearer et al.* (2022), we allow the ECS function to vary with source location to accommodate the possibility of lateral variations in attenuation. This is done by selecting reference small-magnitude calibration events for each target event that are within 2 km in depth and 10 km horizontally. To ensure that the ECS is well-resolved, we require a minimum of 10 calibration events to include the target event in our final results. This approach dampens any spatial variations in the average stress drop of small earthquakes, but has the great advantage of being able to robustly resolve stress-drop variations of larger events.

2.3.1 P-wave Analysis

For the P-wave analysis, we use M 1.5 ± 0.1 earthquakes as calibration events for each target earthquake, and obtain an event-specific ECS by assuming their average corner frequency is $f_c = 30$ Hz with a high-frequency falloff rate of $n = 2$ (Eqn. 2.2). The target earthquake's source spectrum is then obtained using this ECS, and we measure the low-frequency spectral level Ω_0 as the relative moment and corner frequency f_c for the event by fitting a Brune model (Eqn. 2.2) with a high-frequency falloff rate of $n = 2$. The fitting procedure evaluates the difference between the modeled and observed source spectrum in a frequency range from 2.5 to 35 Hz where there is generally a good signal-to-noise ratio. Note that we allow the best-fitting target event corner frequency to be above 35 Hz, but these high corner frequencies are less reliably resolved that those found within the usable data bandwidth. However, it is important to retain these high-corner-frequency events when computing median stress drops to avoid possible selection bias. (*Shearer et al.*, 2006, 2022).

The seismic moment $M_0$is linearly proportional to Ω_0, and we compute a single

empirical scaling factor between catalog M_0 and our observed Ω_0 using events with catalog $M_W$values between 3.5 and 4.5 (Fig. 2.3). We compute the median estimated logM_0 for both $M_L$bins (red boxes) and $M_W$bins (blue boxes) of width 0.2 magnitude in Fig. 2.3, and fit lines separately to the small ($M < 3.4$) $M_L$earthquake bins, and medium ($3.4 \leq M < 5.1$) $M_W$earthquake bins. We find slopes of 0.98 and 0.92 for the $M_L$and $M_W$earthquakes respectively. Using the empirical scaling factor, we convert the relative moments (Ω_0) of all earthquakes to absolute moment estimates (M_0) and finally their corresponding $M_W$estimates (*Hanks and Kanamori*, 1979).

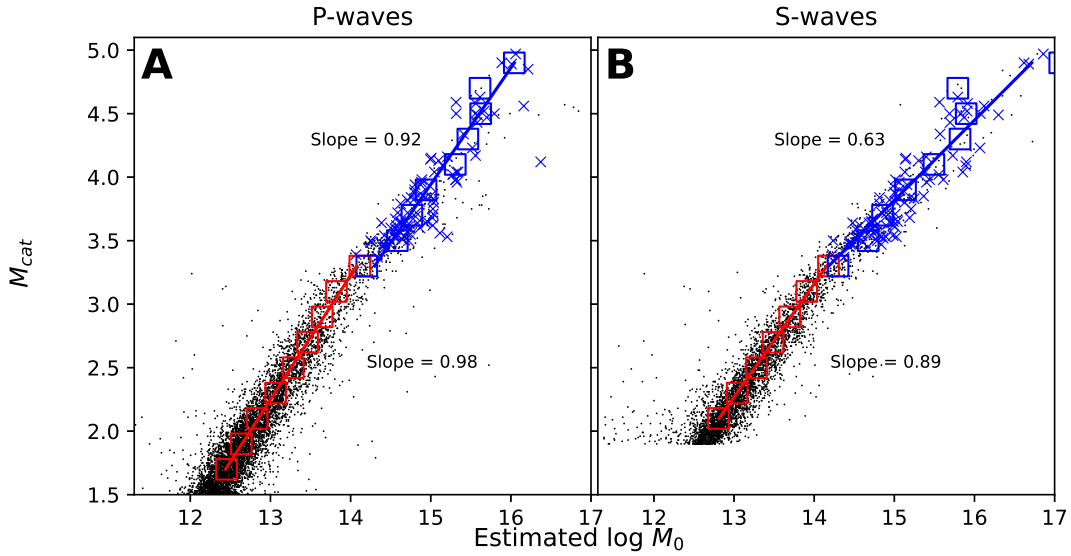


Figure 2.3. Catalog magnitude versus estimated log moment for P-wave (panel A) and S-wave (panel B) datasets, separated into two groups: earthquakes with only a local magnitude (black dots) and earthquakes with a catalog moment magnitude (blue Xs). Each group is binned separately using a bin width of M 0.2 (red and blue squares), and the best-fitting line to the resulting bins is shown for local magnitudes (red line) and moment magnitudes (blue line). The approximate slopes are shown next to each line. Note that local magnitude earthquakes above M 3.4 are not used in fitting the lines.

From the estimated f_c and M_0values, we estimate Brune stress drops (*Brune*, 1970; *Madariaga*, 1976; *Abercrombie*, 1995) as:

$$\Delta\sigma = \frac{7}{16}\left(\frac{f_c}{k\beta}\right)^3 M_0, \tag{2.3}$$

where we use values of $k^P = 0.38$ for P-waves and $k^S = 0.26$ for S-waves (*Kaneko and Shearer*, 2014), and S-wave velocity is taken as $\beta = 3.464$ km/s. The effects of using a fixed depth-independent β are explored further in the Discussion section below. Our P-wave analysis method is similar to that in *Shearer et al.* (2022). The two analyses differ in: the datasets used; the distance range for the ECS calibration earthquakes, within 10 km horizontally in this study instead of 5 km in *Shearer et al.* (2022); our use of the Hann taper rather than multitapers for computing spectra; and that we use catalog $M_W$values to determine the Ω_0 to M_0 scaling factor. A summary of model parameters is given in Table 2.1.

2.3.2 S-wave Analysis

We apply a similar method to analyze the S-waves, but with different processing parameters. Limited by the low signal-to-noise ratios observed at high frequencies for S-waves, we found the S-wave spectral decomposition results are unstable when using M 1.5 earthquakes as calibration events as in the P-wave analysis. Instead, we use M 2 ± 0.1 earthquakes as the calibration events with a fixed average corner frequency of $f_c = 17$ Hz and a falloff rate of $n = 1.8$ to compute event-based ECS terms (Eqn. 2.2). The f_c value is obtained by trial-and-error so that the average stress drops obtained from S-waves for M 2 events agree with the P-wave results, and $f_c = 17$ Hz is also within the range of values for M 2 earthquakes seen in the borehole results of *Abercrombie* (1995).

The S-wave source spectra have better signal-to-noise at lower frequencies than those of P-waves but have poorer signal-to-noise at high frequencies. We find that the S-wave spectra generally have reliable signals in the 1.5 and 15 Hz band, and we use this band to estimate corner frequency and relative moment. We estimate Ω_0 and f_c for each target event by fitting the model using a similar approach as applied to the P-waves, except the falloff rate is set to $n = 1.8$. As in the case of P waves, we allow the best-fitting corner frequency to be above the upper limit of the fit (15 Hz for S waves). The relative moment

Table 2.1. Model parameters used in this study.

	P-wave Analysis	**S-wave Analysis**
Window length ($\leq$ M3.28)	1.28 s	1.28 s
Window length ($>$ M3.28)	2.56 s	2.56 s
Seismogram component	vertical	horizontal
Calibration eq. size	M1.4–M1.6	M1.9–M2.1
Calibration eq. assumed f_c	30 Hz	17 Hz
Calibration eq. n	2.0	1.8
k	0.38	0.26
Model fit freq. range	2.5–35 Hz	1.5–15 Hz

Ω_0 is then converted to M_0using the same process as for the P-waves (Fig. 2.3). We find slopes of 0.89 and 0.63 for the the M_L($M < 3.4$) and M_W($3.4 \leq M < 5.1$) earthquakes respectively. The moment and corner frequency measurements from S-waves are finally used to estimate a second set of stress drops. The falloff rate of $n = 1.8$ produces a slower high-frequency decay than the standard Brune model with $n = 2$. This parameter choice was selected to have the S-wave moment and stress-drop estimates that roughly agree with the P-wave estimates on average. A summary of model parameters is given in Table 2.1. We discuss the details in the following sections.

2.4 Results

We find that the estimated relative log moment ($\log M_0$) scales differently with the catalog magnitudes for P- and S-waves. This difference appears marginal for the $M_L$earthquakes at lower magnitudes with slopes of 0.98 for the P-wave results and 0.89 for the S-wave results (Fig. 2.3). For M>3.4 earthquakes, the slopes are 0.92 for P-waves and 0.63 for S-waves (Fig. 2.3). Consequently, the estimated M_0agree well between the P-wave and S-wave results for small events, but this agreement breaks down for the larger $M_W$earthquakes. Relative to the S-wave results, the P-wave moment estimates increasingly underestimate $M_0$for larger events (Fig. 2.4a).

We compare the corner frequency f_c with the seismic moment $\log M_0$ in Fig. 2.5.

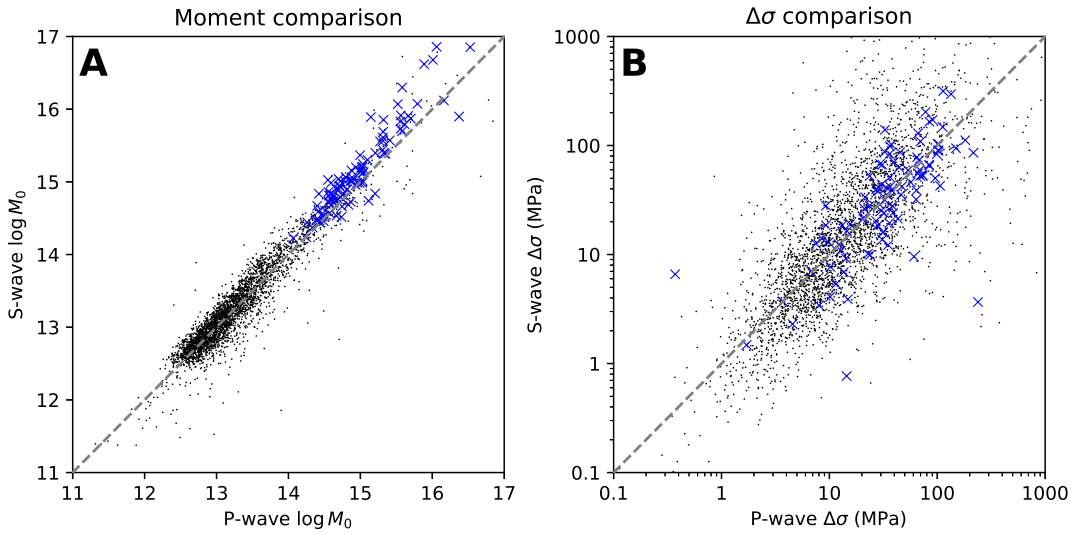


Figure 2.4. Comparison between P-wave and S-wave spectral decomposition estimates of log moment (panel A) and stress drop (panel B). Blue Xs depict earthquakes that have a catalog moment magnitude.

The corner frequency should scale with the seismic moment for self-similar earthquakes. To evaluate our results, we compute scaling lines (Eqn. 2.3) for constant stress drops ($\Delta\sigma$as 1, 10, and 100 MPa) with $k^P = 0.38$ and $k^S = 0.26$ for the P- and S-wave results (*Kaneko and Shearer*, 2014). Both results appear to deviate from the constant-$\Delta\sigma$scaling lines, and the deviation is more prominent in the P-wave results (Fig. 2.5).

Our median stress-drop estimates are 14.3 MPa and 16.9 MPa for the P- and S-wave results, respectively. For the same events, the P- and S-wave stress drops roughly agree, albeit with larger scatter in comparison to the relative moment differences (Fig. 2.3).

This agreement between our P- and S-wave estimates results from both choosing the calibration event corner frequencies as detailed above, and the choice of high-frequency falloff rates (Fig. 2.6). For example, when fitting S-wave spectra using n values ranging from 1.7 to 2, we find that the associated median stress drops increase with magnitude, with a more pronounced effect when using a larger n. While P-wave results with $n = 2$ agree well with S-wave results with $n = 2$ for the larger earthquakes (M > 3.4), we take stress drops for these earthquakes to be less reliable because of the apparent magnitude-$\Delta\sigma$scaling for

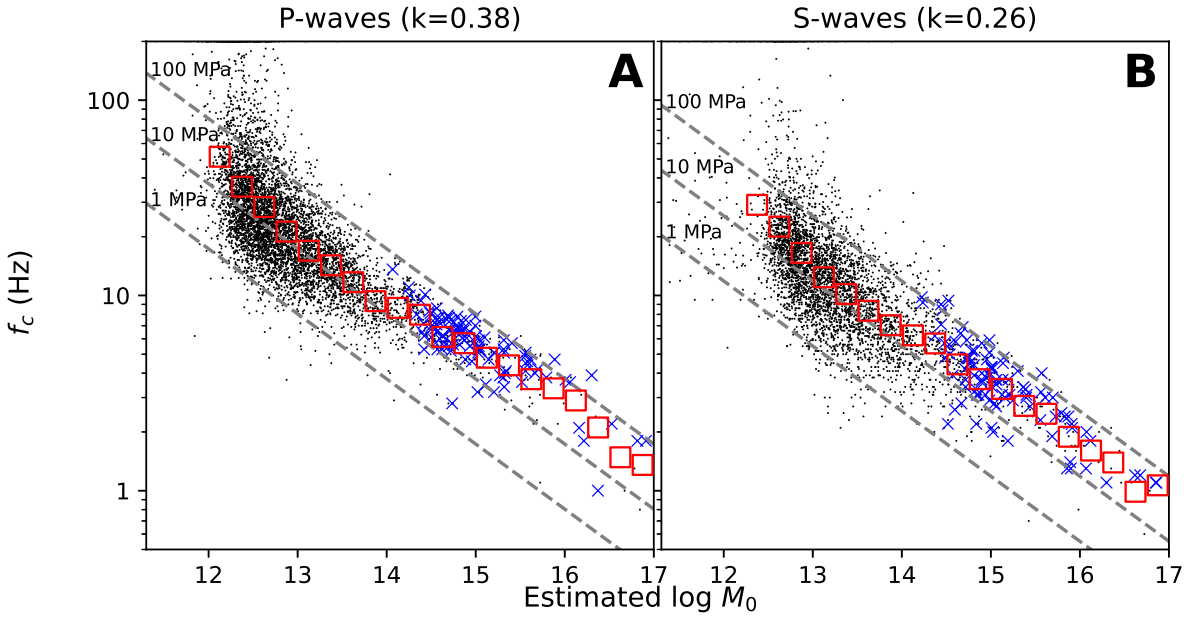


Figure 2.5. Corner frequency versus estimated log moment for both P-wave (panel A) and S-wave (panel B) trials. Blue Xs depict earthquakes that have a catalog moment magnitude. Results are binned by log moment with bin widths of 0.25. Equal stress drop lines are shown as dashed gray lines. Note that we use $k = 0.38$ for P-waves, and $k = 0.26$ for S-waves following *Kaneko and Shearer* (2014).

smaller earthquakes. We choose the S-wave falloff rate based on agreement for earthquakes smaller than M 3.4 and use the P-wave stress-drop estimates obtained with $n = 2$ as a reference (Fig. 2.6a). Using $n = 1.8$ for S-waves yields general consistency between the two groups of results. Additionally, we find that the median P-wave stress-drop estimates are nearly constant for M<3.4 earthquakes, while displaying a linear increase with magnitude for larger earthquakes. A similar stress-drop-magnitude relationship is also observed in the S-wave results for $n = 1.8$, with a constant stress drop for the smaller earthquakes (M< 3.4). However, $n = 1.7$ causes a slight decrease in stress drop with magnitude, and $n = 2$ causes a slight increase for the same range.

We find no significant temporal variation of average stress drop in our results (see Fig. S4 in the electronic supplement). However, our stress-drop estimates show structured patterns in their spatial distributions with large variations for both the P-wave and S-wave

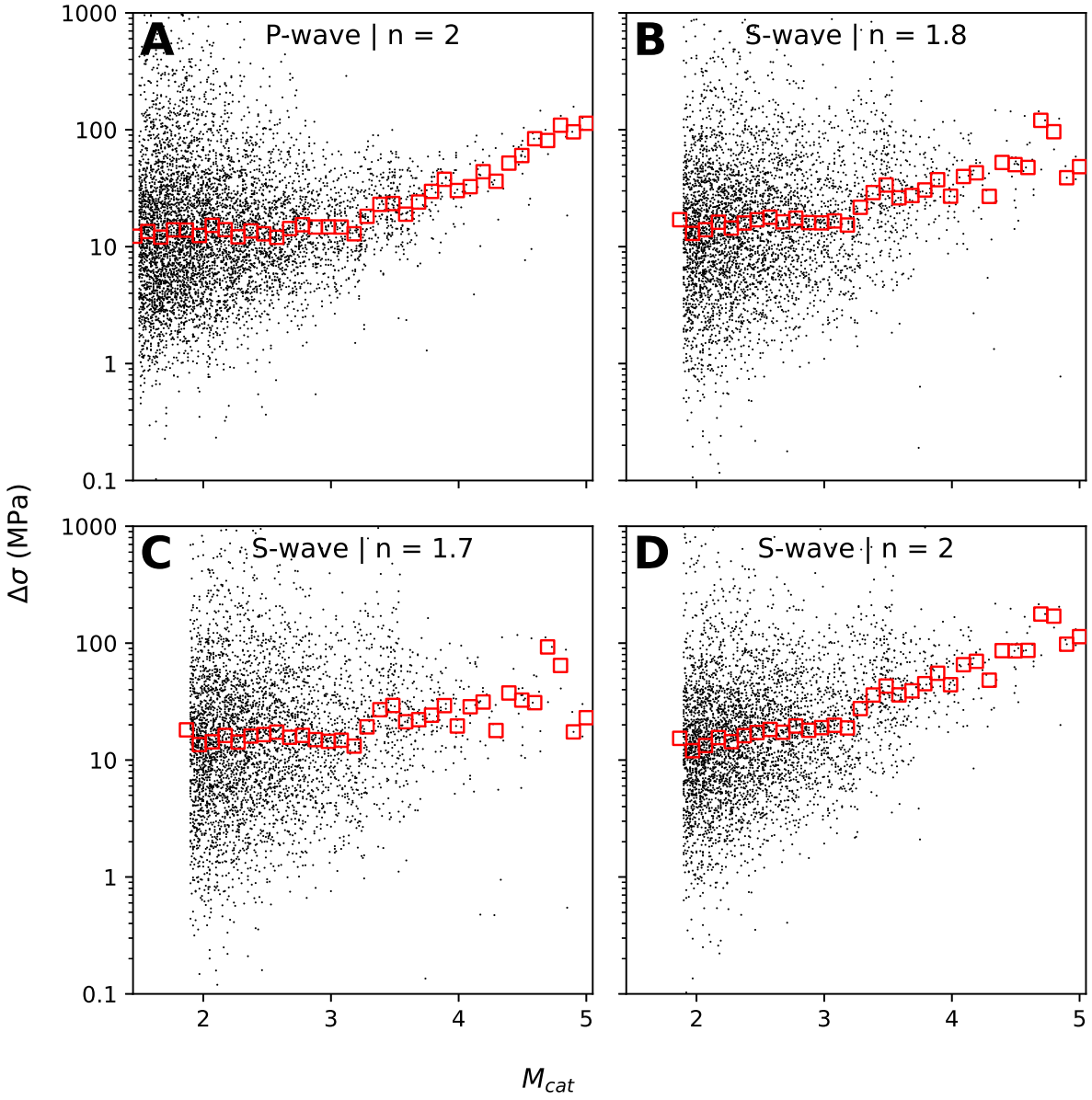


Figure 2.6. Comparison between (A) P-wave $\Delta\sigma$results for $n = 2$, (B) S-wave $\Delta\sigma$results for $n = 1.8$, (C) S-wave $\Delta\sigma$results for $n = 1.7$, and (D) S-wave $\Delta\sigma$results for $n = 2$. Red squares depict medians of bins of width M 0.1.

results (Figs. 2.7 and 2.8). The spatial patterns and the associated variations are consistent between the P-wave and S-wave results in both the along-strike and along-dip directions. Note that in Figs. 2.7 and 2.8, we present the spatial variations of M>2 P-wave results and M>2.5 S-wave results, i.e., not plotting the smallest magnitude events in each data

set. This is to emphasize the greater resolution of spatial variations obtained for the larger events, as the variations are suppressed near the calibration magnitudes of 1.5 and 2 for P and S waves, respectively, where the average corner frequencies are fixed. Fig. 2.4b shows that our P- and S-wave stress-drop estimates are highly correlated for events in common but with considerable scatter. To study the correlation in more detail, we compute local correlation coefficients between our P and S stress drops by using the nearest 20 events of $M \geq 2.5$ in common to each target event. These spatially-varying correlation coefficients are plotted in Figs. S5 and S6 in the electronic supplement and show that the P and S stress drops are correlated ($r > 0.5$) across most of the seismicity.

We find that earthquakes near the Coso geothermal field tend to have lower stress drops, while events near the M 7.1 mainshock and the fault intersection region have higher stress drops (Figs. 2.7). In Fig. 2.8, the along-dip profiles seem to suggest that there is an increase in stress-drop estimates with depth, although this apparent trend is not statistically significant, and the median stress-drop estimates at different depths are largely constant with both P- and S-waves. Events shallower than 2 km tend to have lower stress drops than the rest of the earthquakes. However, this apparent distinction may result from the ECS terms, and we further discuss the uncertainties in the following section.

2.5 Discussion

Local magnitude $M_L$and moment magnitude $M_W$scale differently with seismic moment M_0obtained from the source spectrum (e.g. *Utsu*, 2002a; *Shearer*, 2019). $M_L$was originally developed to quantify earthquake size in southern California (*Richter*, 1935). It is proportional to the maximum log amplitude of a bandpass-filtered seismogram at a fixed event-receiver distance. It is not defined based on physical rupture characteristics; $M_L$can only be related to M_0empirically. Studies based on small southern California earthquakes have found that $M_L$scales linearly with $\log M_0$ with a slope of approximately 1 (e.g. *Shearer*

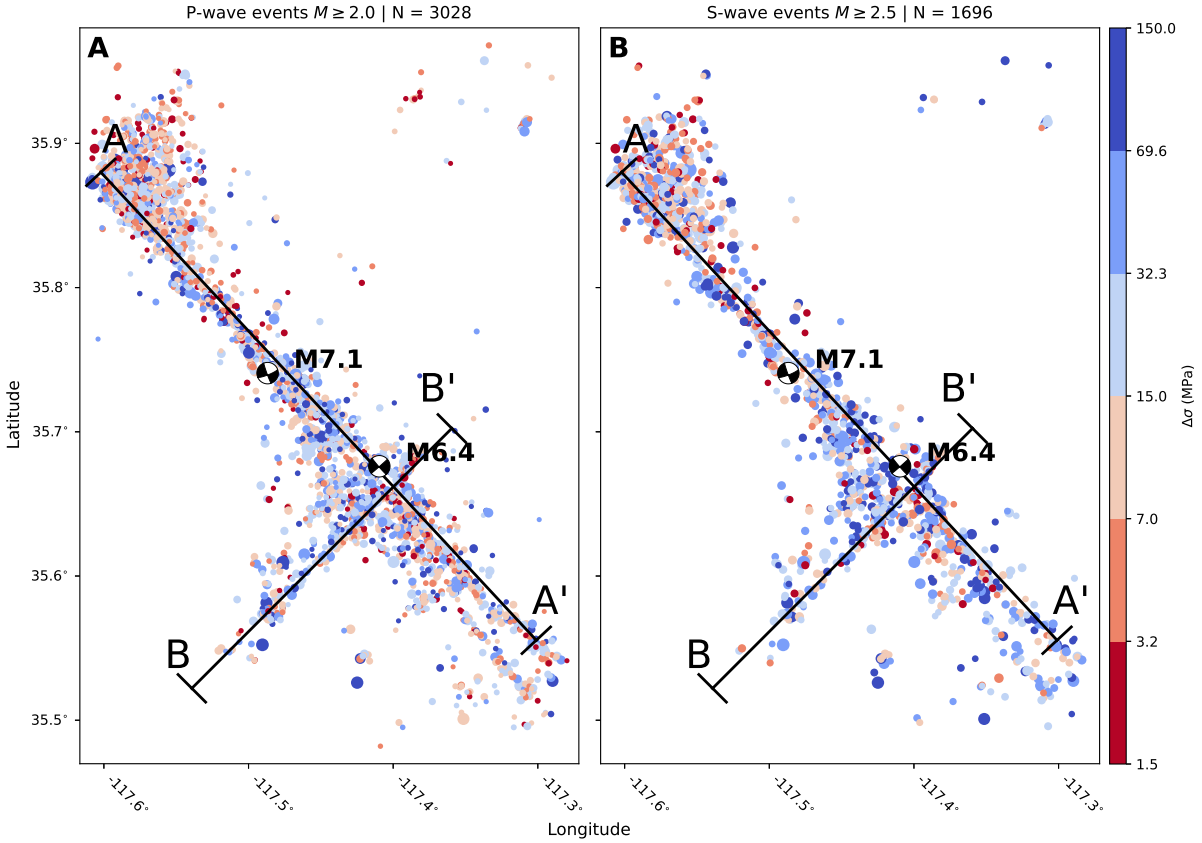


Figure 2.7. Spatial distribution of estimated stress drops from P-waves (panel A) and S-waves (panel B). Marker size is proportional to earthquake magnitude. Panel A only shows earthquakes greater than M 2, and panel B shows earthquakes over M 2.5. Earthquakes within 1500 meters of each cross-section, depicted by the length of the ticks at the ends of each line, are included in the cross-section plots. Since roughly the lowest and highest 5% of stress drops lie outside of [1.5, 150] MPa, these outliers are plotted as their respective end color.

et al., 2006; *Ross et al.*, 2016), so $M_L \approx \log M_0 + C$ where C is a constant. *Hanks and Kanamori* (1979) introduced moment magnitude M_W by defining an earthquake's moment, M_0, based on its rupture area, average slip, and shear modulus. M_W scales exactly as $\frac{2}{3}\log M_0$, so we expect a slope of $\frac{2}{3}$ when plotting moment magnitude versus $\log M_0$.

We find that small M_L earthquakes roughly obey the relationship $M_L \propto \log M_0$ in both types of data; i.e. the slope of the best-fit line through the median bins is close to unity. This agrees with the previous studies noted above, and confirms that the S-wave method works for estimating M_0 of these smaller earthquakes. However, the P-wave method

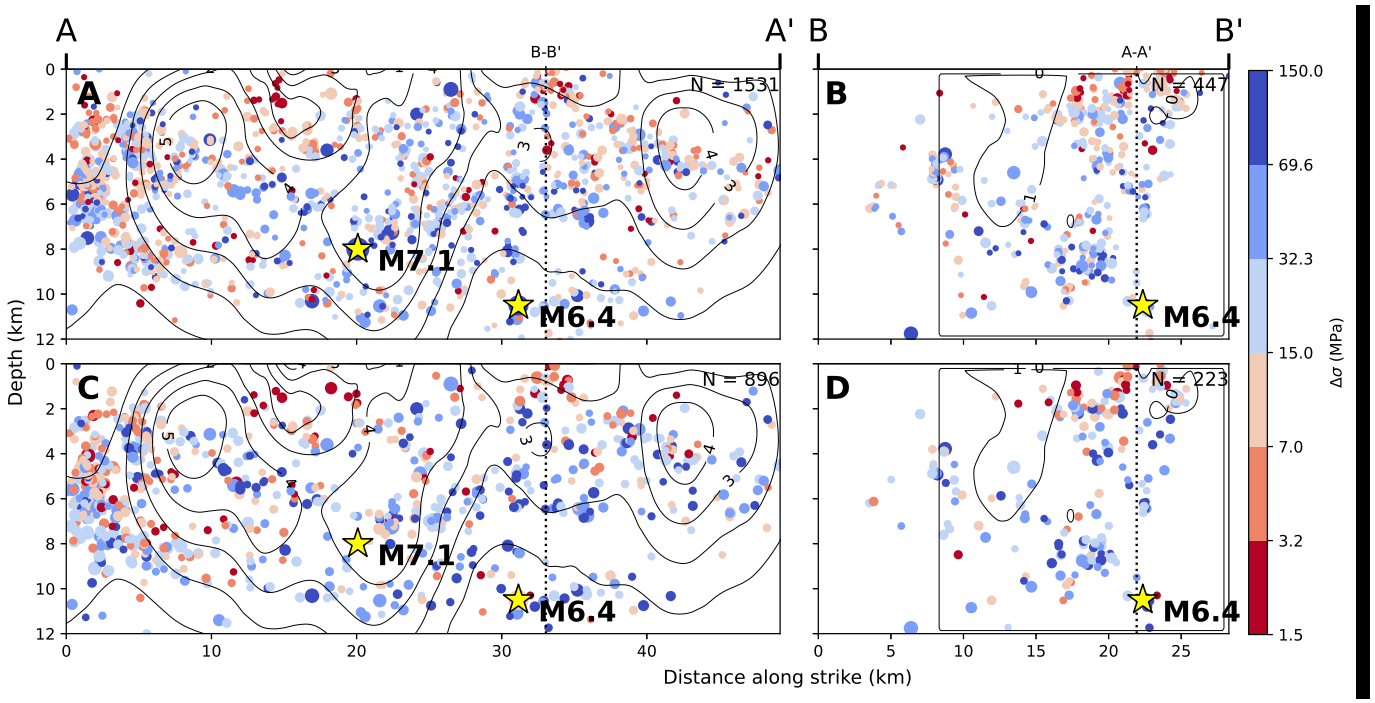


Figure 2.8. Cross sections depicting the spatial distribution of stress drops at depth for line A-A' (left panels) and line B-B' (right panels). The top two panels correspond to the P-wave results and the bottom two panels show S-wave results. Marker size is proportional to earthquake size. Depths are vertically exaggerated and not to scale. The M 6.4 foreshock and the M 7.1 mainshock are shown as yellow stars. Slip contours are derived from *Wang et al.* (2020), who uses a joint inversion process to estimate a slip model for the M 7.1 mainshock. To compute contours, slip data is projected onto the cross section and interpolated onto an equally-spaced grid using a cubic spline.

fails to capture the theoretical scaling relationship for the $M_W$earthquakes, as reported in *Shearer et al.* (2022). It was hypothesized that the M_0estimation method caused the mismatch, specifically that the low-frequency part of the spectrum is not a good estimate of the zero-frequency amplitude for large earthquakes because of their lower corner frequencies (*Shearer et al.*, 2022). In contrast, the $M_W$earthquakes roughly obey the theoretical $\frac{2}{3}$ scaling relationship from M 3.4 up to about M 4.2 when using S-waves. We also observe this one-to-one to $\frac{2}{3}$ scaling transition in Fig. 2.4a in the direct comparison of P-wave and S-wave estimated M_0, where the small $M_L$earthquakes have agreement, but for the larger $M_W$events the S-wave moment estimates are larger than the P-wave estimates. This $\frac{2}{3}$ scaling relationship seems to break down for $M_W \geq 4.2$ earthquakes when using S-waves.

While a Brune model likely oversimplifies the actual rupture process (*Abercrombie*, 2021), it can be a useful average model when studying large numbers of events. A falloff rate of 2 is commonly used for analyzing earthquake source spectrum, including in spectral decomposition studies, but models using different falloff rates can sometimes fit spectra equally well (e.g. *Shearer et al.*, 2019). For consistency, we fit P-wave spectra using simple Brune models ($n = 2$). We find that the P-wave $\Delta\sigma$is relatively constant up to about M 3.4, then steadily increases with magnitude (Fig. 2.6). In experiments using different falloff rates for the S-wave analysis, we find that a falloff rate of $n = 2$ results in increasing $\Delta\sigma$for all magnitudes (Fig. 2.6). Conversely, a falloff rate of $n = 1.7$ results in a slight decrease in $\Delta\sigma$through about M 3.4, then an increase with magnitude. Our parameter choices (e.g., $n = 1.8$) for analyzing S-waves are guided by these numerical experiments (Figs. 2.3–2.6). For M 2.5–4 events, the assumed high-frequency falloff rate n directly affects the trend in median stress drop, in that higher values of n translate into a greater increase in median $\Delta\sigma$with magnitude. In this magnitude range, $\Delta\sigma$moderately increases with magnitude when using $n = 1.8$, which is more consistent with the original P-wave results (Fig. 2.6d). However, all values of n we tested result in an increase in $\Delta\sigma$with magnitude. We note that the circular rupture modeling of *Kaneko and Shearer* (2014) predicts generally lower S-wave falloff rates, although the physical significance of different high-frequency falloff rates between P and S waves is unclear. However, the S-wave spectra are fitted between 1.5 to 15 Hz, and the $n = 1.8$ falloff rate used in this study could represent an interval at intermediate frequencies beyond which the spectrum steepens to $n = 2$ (*Ji and Archuleta*, 2022).

The longer source duration of larger magnitude earthquakes requires a longer window length in spectral source studies to capture the complete waveform. We use a window length of 1.28 s for earthquakes of M<3.29, and 2.56 s for earthquakes of M 3.29 and above. Spectra of the smaller earthquakes have a frequency resolution $df \approx 0.78$ Hz, and spectra of the larger earthquakes are resampled at the same frequencies. The earthquake seismic

moment is estimated from the average of the 4th through 6th spectral points, around 2.3 to 3.9 Hz. Earthquakes with f_c approaching this value will have higher uncertainty in both f_c and M_0, and therefore higher uncertainty in $\Delta\sigma$.

Self-similarity assumes that rupture size scales with magnitude for large and small earthquakes, suggesting that stress drop does not change with magnitude (*Aki*, 1967). This assumption has been challenged in recent years (e.g. *Abercrombie*, 2021; *Bindi et al.*, 2020a; *Goebel et al.*, 2015). We find that P-waves with $n = 2$ and S-waves with $n = 1.8$ (Fig. 2.6a,b) obey self-similarity with relatively high median stress drops of 13.6 MPa and 15.4 MPa for P- and S-waves for the smaller (M$<$ 3.4) earthquakes, but depart from similarity for larger earthquakes. Similar stress-drop-magnitude scaling has been reported in *Shearer et al.* (2022), from which our method is originated.

This stress-drop-magnitude scaling relationship of the Ridgecrest sequence has been reported in other studies that analyze P- and S- waves using similar spectral decomposition methods. *Trugman* (2020) used P-waves to analyze M_L 1.3–5.0 earthquakes and found stress drop increases with magnitude, with median stress drops of about 1.2 MPa for M2 events, up to about 10 MPa for M4 events. *Bindi et al.* (2020b) used S-waves to study M 2.5–7.1 events, and found a similar increase of stress drop with magnitude, with median stress drops of about 2.5 MPa for M 3 events and about 5 MPa for M 5 events, and an overall median stress drop of 3.0 MPa. In both studies, the median stress drops are less than 10 MPa for all magnitudes. These observed scaling relationships might be due to the choice of falloff rates (Fig. 2.6; *Trugman*, 2020) and the scaling is also likely related to the ECS correction and its estimation procedure. When the spectral decomposition event terms are stacked and averaged in bins by moment, the ECS gives the best fit of a theoretical Brune source model to the stacks. The possibility of non-self-similar scaling can be accommodated with a single parameter controlling a linear dependence of log stress drop to log moment (*Trugman*, 2020; *Trugman and Shearer*, 2017a). For example, using this approach, spectral data for five regions in southern California were best fit with models

in which stress drop increased with magnitude (*Trugman and Shearer*, 2017a). However, there are tradeoffs among the available parameters (e.g., small earthquake median stress drop, stress-drop scaling with magnitude, high-frequency falloff rate) used to estimate the ECS, challenging the ability of the method to reliably address the self-similarity issue (*Shearer et al.*, 2019). Following *Shearer et al.* (2022), we do not attempt to address the scaling issue for M 1.5 to 3.5 earthquakes directly, but do find that the Ridgecrest stress drops are approximately self-similar over this magnitude range when the average reference event corner frequencies are set as 30 Hz and 17 Hz for P and S waves, respectively. We observe an increase in stress drop with magnitude for $M > 3.5$, but, as discussed in *Shearer et al.* (2022), this increase is unrealistic when extrapolated beyond M 5 and would be reduced if smaller high-frequency falloff rates are assumed ($n < 2$), such as those seen in double corner frequency models *Ji and Archuleta* (2022); *Denolle and Shearer* (2016).

2.5.1 Spatial Variation of Source Parameters

Stress drops of Ridgecrest aftershocks are heterogeneous and vary in space (*Trugman*, 2020; *Bindi et al.*, 2021; *Shearer et al.*, 2022). We evaluate stress drop variations along two cross sections corresponding to the rupture planes of the M_W7.1 Ridgecrest mainshock and the M_W6.4 foreshock (profile lines A-A' and B-B' in Figs. 2.7 and 2.8). We observe spatially structured, lateral and vertical variations in average stress drops in both the P- and S-wave results. These variations are coherent between the two set of estimates, i.e., we find clusters of high- and low-stress drop earthquakes in similar locations.

As shown in Fig. 2.7, we find lateral variations on the scale of kilometers, most prominent in the cluster of low stress-drop earthquakes near the Coso geothermal field, and also in a cluster of high stress-drop earthquakes just southeast of the M 7.1 mainshock. Similar relative variations in stress drop are reported in *Trugman* (2020), albeit with different absolute stress drops. We find no strong correlation between median stress drop and depth for either cross section, except in the top 2 km where we observe clusters of low

stress drop. Lower stress drops in shallow earthquakes has been observed in other studies, which may result from inaccurate attenuation corrections (*Abercrombie et al.*, 2021). In our study, we implement an event-based ECS to correct the path effects, which could account for depth-varying attenuation. However, we assume a fixed shear velocity (β in Eqn. 2.3), not attempting to account for the slower S-wave velocities at shallow depths, and impose a fixed average corner frequency to the reference small-magnitude events independently of depth, which complicates the interpretation of the observed, apparent depth-dependent pattern. Determining whether the observed increase in median stress drop in the top 5 km is real would require accounting for the increase in shear velocity with depth (and likely corresponding increase in rupture velocity) and the effect of our ±2-km-in-depth reference event selection criteria in a region with strong vertical gradients and likely depth-dependent attenuation. These issues are discussed at greater length in *Abercrombie et al.* (2021) and *Shearer et al.* (2022) and deserve further study. Nonetheless, the observed low-stress-drop clusters at shallow depth are significant, in that they appear in the larger magnitude events in locations where the smaller magnitude events are constrained to have stress drops closer to the median values.

Slip due to the M 6.4 and M 7.1 Ridgecrest mainshocks would result in a low-stress zone where the slip occurred, bordered by a region of high-stress where rupture did not occur (*Harris*, 1998). This might impact the stress drop distributions of the aftershocks depending on their locations. By comparing to the Ridgecrest slip distribution from *Wang et al.* (2020) (Fig. 2.8), we find no clear correlation between the slip model and our stress-drop estimates. Further analysis of the stress drop versus slip relationship using other finite fault models is shown in Fig. S7 in the electronic supplement. We compare our estimates of stress drop to slip estimates from *Ross et al.* (2019), *Xu et al.* (2020), *Wang et al.* (2020), *Yue et al.* (2021), *Jin and Fialko* (2020), *Chen et al.* (2020), and *Liu et al.* (2019). Again, we find no clear correlation.

Woessner et al. (2006) found correlation between the mainshock stress drop dis-

tribution and aftershock location, however did not look at individual aftershock stress drops. A possible inverse correlation between fault slip and aftershock stress-drop was seen by *Shearer et al.* (2006) for some areas along the 1992 Landers earthquake rupture, but results were inconclusive for the entire fault. *Folesky et al.* (2024) examined stress drop across a subduction zone in northern Chile and found that earthquakes closer to the fault interface had lower stress drops than those above or below the interface. Another study, *Ruhl et al.* (2023), found that the rupture area of the M 4.9 Mogul, Nevada earthquake was preceded by high stress-drop foreshocks followed by fewer aftershocks in the same area, but bordered by zones containing some high stress-drop aftershocks. Contrary to the hypothesis that high-slip regions would have lower aftershock stress drops, we find examples of high-stress-drop clusters within large-slip patches and also low-stress-drop clusters near the edge of slip patches, such as at the north end of rupture and the shallow events discussed previously. However, the aftershock zone has some width perpendicular to the mainshock fault strike and aftershocks do not necessarily occur on the mainshock rupture plane, i.e., they could occur on parallel or cross-cutting faults. Thus, the relationship between mainshock slip and aftershock stress drop is likely complicated.

We find that the heterogeneous stress-drop distribution does not correlate with the uniform fault zone structure inferred from in-situ V_p/V_s estimates (*Lin and Fan*, 2024). Instead, we observe a qualitative correlation between our stress-drop distribution and the regional 3D P-wave velocity structure (*Zhang and Lin*, 2014). We find that regions of low P-wave velocity near the Coso geothermal field and at shallow depths above the M 6.4 hypocenter have low stress-drop estimates, while the area around the M 7.1 and M 6.4 hypocenters have high P-wave velocity and high stress drop, on average. This apparent correlation could be caused by either an increase in rupture velocity associated with the faster seismic velocities or a true increase in earthquake stress drop. This suggests that at least some of the spatial differences observed in our study could simply be due to using a constant β in Eqn. 2.3, where an overestimation would result in an underestimation of

$\Delta\sigma$, and vice-versa. This finding warrants further study for this and other datasets.

2.6 Conclusions

We apply a spectral decomposition method to estimate source parameters, including seismic moment, corner frequency, and stress drop, for the 2019 Ridgecrest earthquakes using both P and S-waves. We find that the P- and S-wave results are consistent in absolute values when assuming a high-frequency falloff rate of 2 and 1.8 for the two types of data, respectively. Our results provide an observational base for future exploration in physical causes of the different falloff rates between P- and S-waves. Although individual earthquakes can have different estimates between the P- and S-wave results, we find coherent spatial patterns and relative differences in the estimates, regardless of the parameter choices. These spatial patterns have distinct structures in the Ridgecrest fault system, with earthquakes near the Coso geothermal field showing lower stress drops, while earthquakes near the M 7.1 hypocenter have higher stress-drop estimates. We find no strong depth-dependence of the stress-drop estimates, or correlation with the M 7.1 Ridgecrest earthquake slip distribution. We show that P- and S-waves can yield consistent stress-drop estimates with careful parameter choices, and the observed stress-drop distributions likely result from either heterogeneous fault environments or the effects of 3D seismic velocity structures.

2.7 Data Availability and Resources

The results described here were obtained from the datasets for the Ridgecrest stress drop validation study, which can obtained from https://scedc.caltech.edu/data/stressdrop-ridgecrest.html.

Supplemental Material for this article includes estimated source parameter catalogs for both P- and S-waves, and several supplemental figures.

Acknowledgments

We thank the Editors and two anonymous reviewers for their constructive comments to help improve this paper. We also thank the Southern California Earthquake Center (SCEC) for supporting the Ridgecrest stress drop validation study. SCEC is funded by NSF Cooperative Agreement EAR-1033462 and USGS Cooperative Agreement G12AC20038. This is SCEC Contribution #13462.

Chapter 2, in full, is a reprint of the material as it appears in *Bulletin of the Seismological Society of America*. Vandevert, I. C., Shearer, P. M., & Fan, W. (2025). Ridgecrest Aftershock Stress Drops from P- and S-Wave Spectral Decomposition. *Bulletin of the Seismological Society of America*, 115(3), 792-804. https://doi.org/10.1785/0120240133. The dissertation author was the primary investigator and author of this paper.

2.8 Supplementary Materials

Note: Tables S1 and S2 in the supplementary materials are not included in this thesis, as they extend over 10,000 lines. Please see the published document for the full tables.

Table S1: The file ridgecrest_stressdrop_p.txt contains a list of the 6,108 earthquakes with stress drop estimates in this study using P-wave spectra. Using the first line of the file as an example, the format is as follows:

```
17850492 (event ID)
2019 7 4 20 32 34.33 (event year, mon, day, hr, min, sec)
2.05 (catalog magnitude)
35.64113 (event latitude)
-117.55272 (event longitude)
6.221 (event depth, km)
16 (number of records used to compute event term)
139 (number of nearby calibration events)
11.1 (estimated corner frequency, Hz)
2.669e+00 (estimated stress drop, MPa)
```

Event ID, year, month, day, hour, minute, second, catalog magnitude, latitude, longitude, depth (km), # of records in spectral decomposition, # of records in ECS calculation, corner frequency (Hz), stress drop (MPa)

Table S2: The file ridgecrest_stressdrop_s.txt contains a list of the 4,216 earthquakes with stress drop estimates in this study using S-wave spectra, and has the same format as Table S1.

Note for Tables S1 and S2: The maximum best-fit corner frequency is 200.0 Hz. As discussed in the text, spectra with this corner frequency are likely poorly-resolved, but we retain these events to prevent biasing our results.

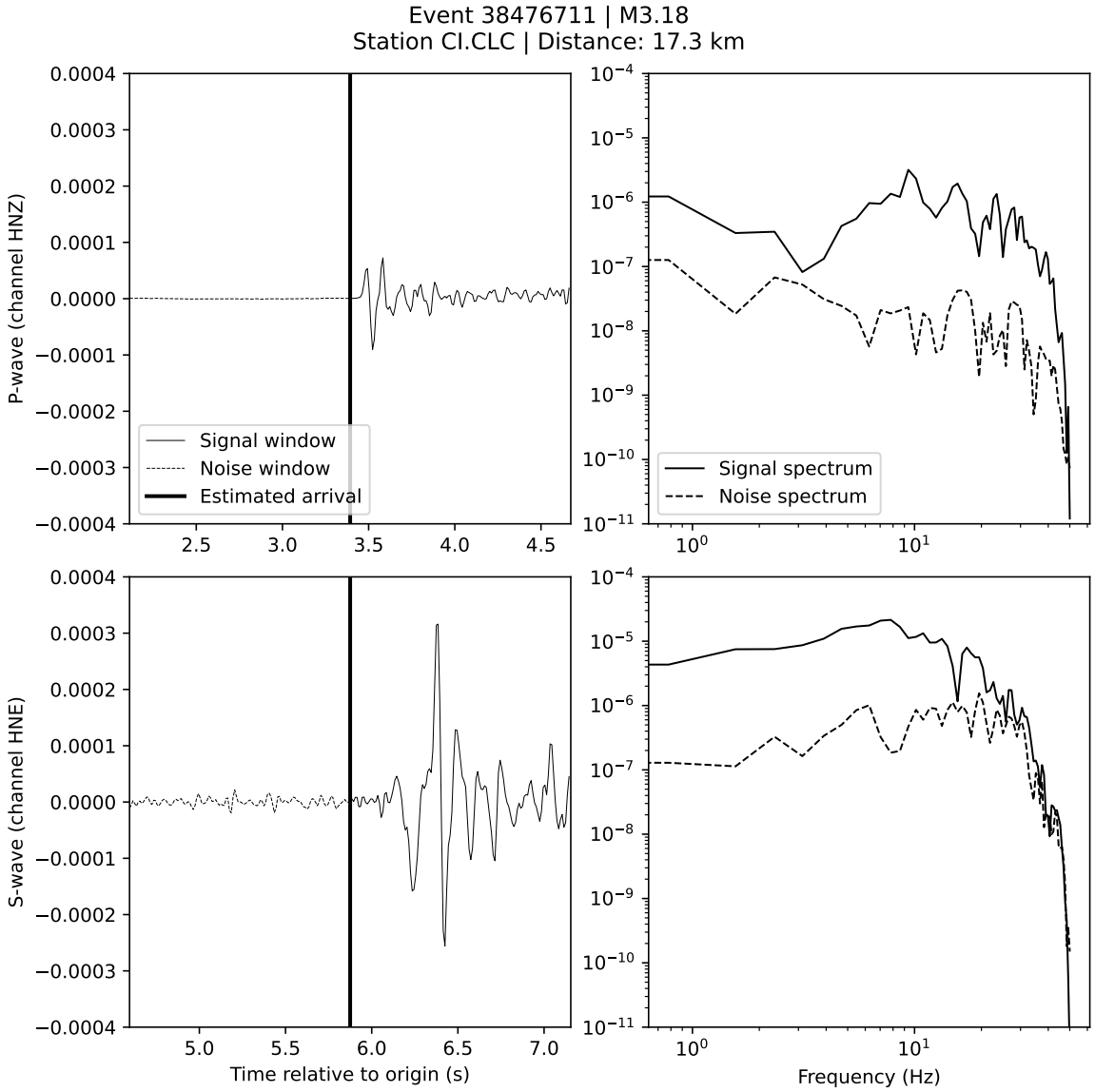


Figure 2.S1. Example showing waveforms (left panels) and their spectra (right panels).

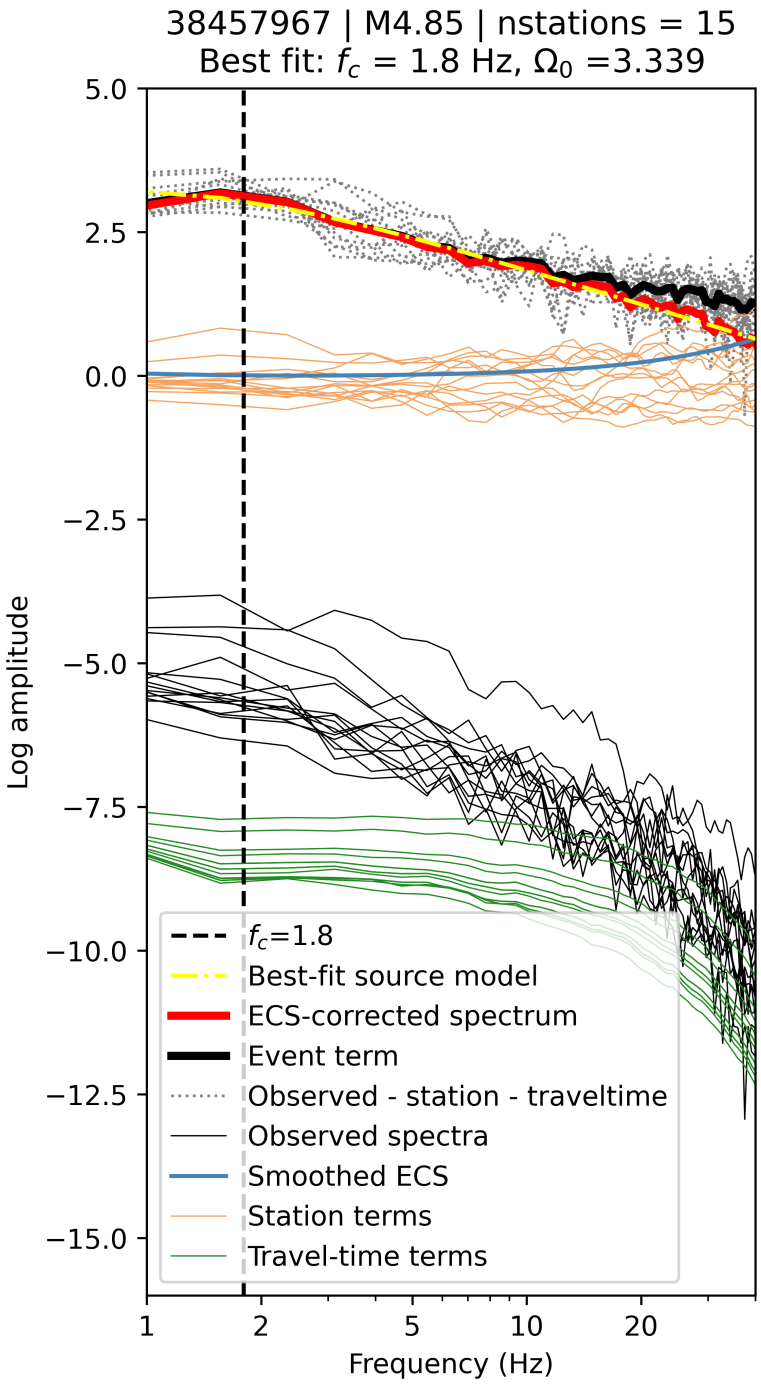


Figure 2.S2. P-wave spectral decomposition example, showing each of the components in Equation 2.1, as well as the empirical correction spectrum (ECS) corrected source spectrum, and the best-fit model parameters.

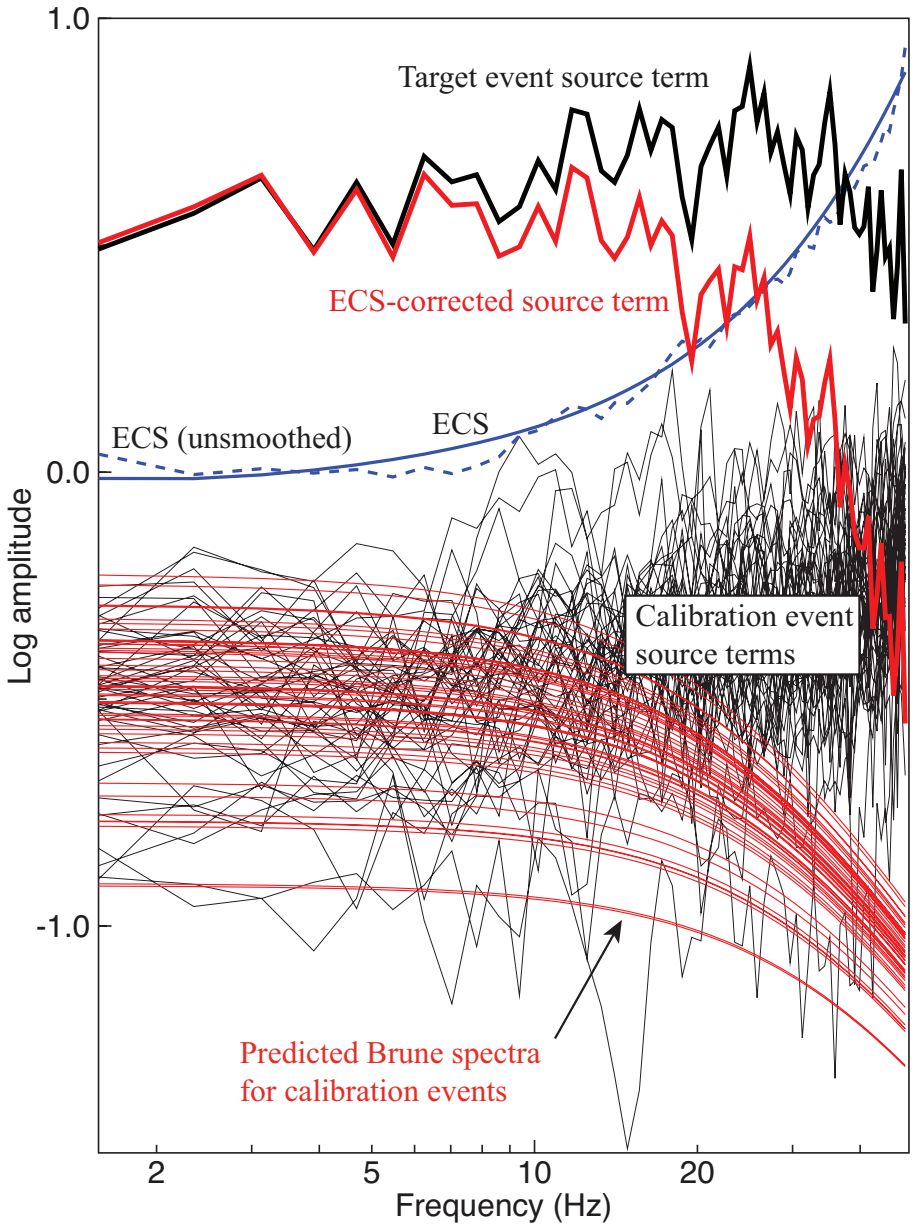


Figure 2.S3. Empirical correction spectrum (ECS) computation example, using small nearby calibration events to correct the spectrum of a larger event. The thick black line shows the source term from spectral decomposition for a M 2.5 earthquake (07/09/2024, SCSN event id 38494055). Note that this is a different earthquake than shown in Figure 2.S2. This event has 49 nearby smaller events of M 1.4 to 1.6. These calibration event source terms are plotted as the thin black lines. The thin red lines show predicted Brune spectra for these events, assuming fc = 30 Hz at M 1.5. The unsmoothed empirical correction spectrum (ECS), plotted as the dashed blue line, is the average difference between the observed source terms and their Brune predictions. The solid blue line shows the ECS following smoothing with a 4th degree polynomial. This ECS is then subtracted from the target event source term to generate the ECS-corrected source term (thick red line).

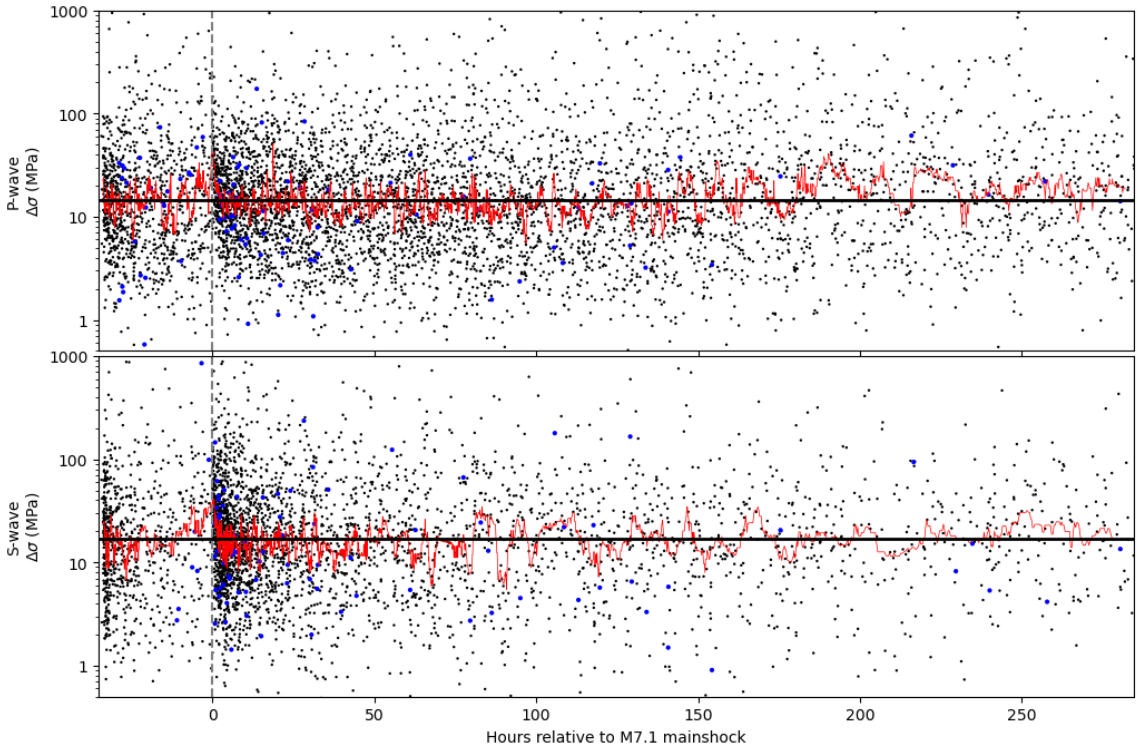


Figure 2.S4. Temporal plot of stress drop vs. time. The median stress drops of 14.3 MPa and 16.9 MPa for P- and S-wave analyses respectively are shown as horizontal black lines. A rolling average of 30 earthquakes is shown as a red line.

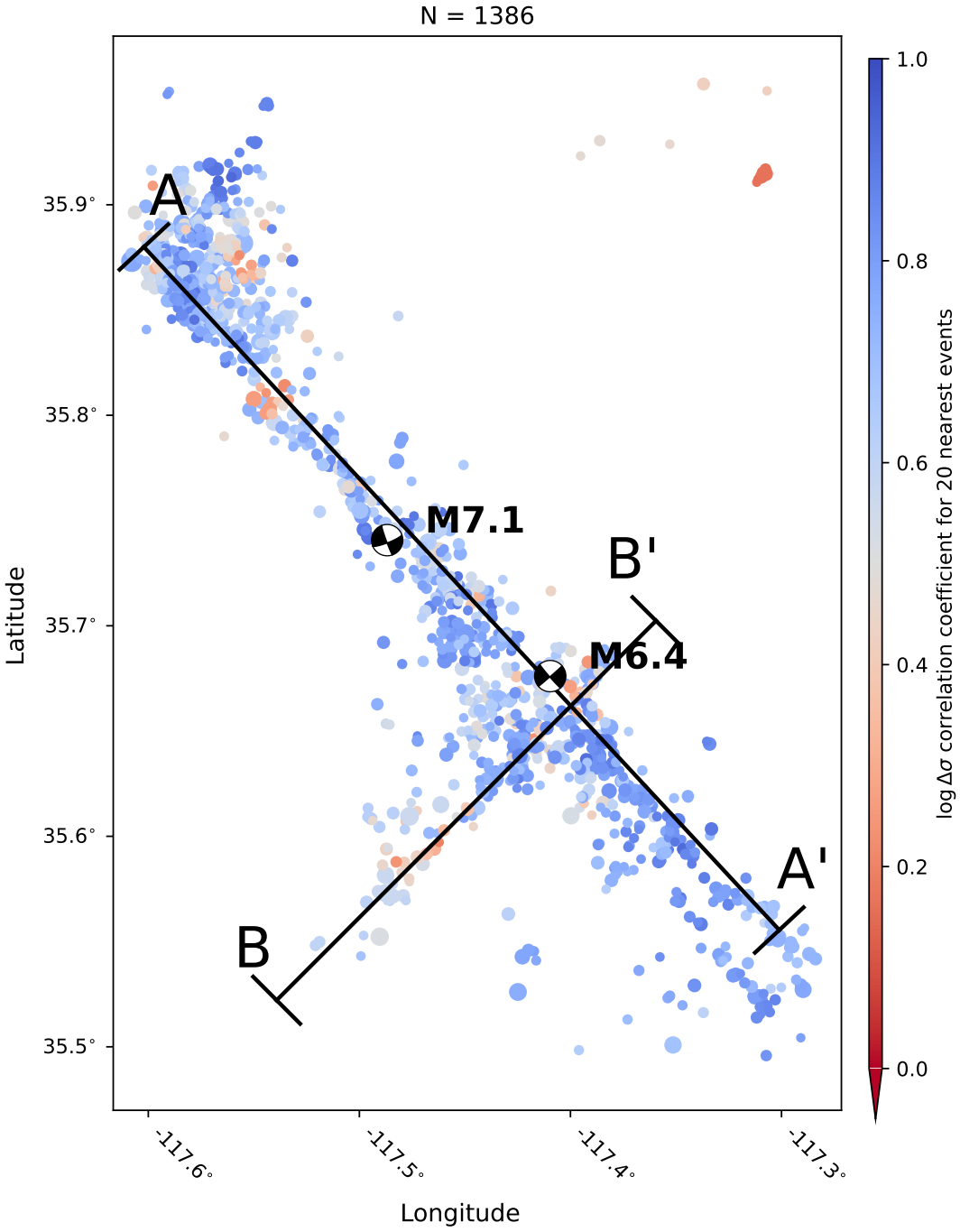


Figure 2.S5. Spearman correlation coefficients of P versus S for earthquakes that have stress-drop estimates for both P- and S-waves. The values shown are the correlation coefficients for each target earthquake and its 20 nearest neighbors. Note that the width of the cross-section is 1750 m, rather than 1500 m as in Figures 2.7 and 2.8 in the main text, to capture more events in cross-section. We use the Spearman correlation coefficient rather than Pearson's because it is more robust when outliers are present. While a few clusters have low correlation due to several outliers, most of the events seem to be correlated spatially.

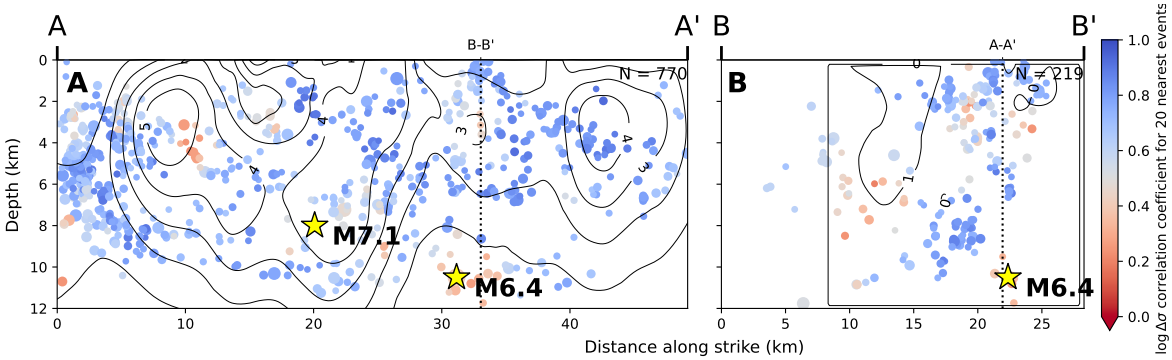


Figure 2.S6. Cross-sections of the Spearman correlation coefficients shown in Figure 2.S5.

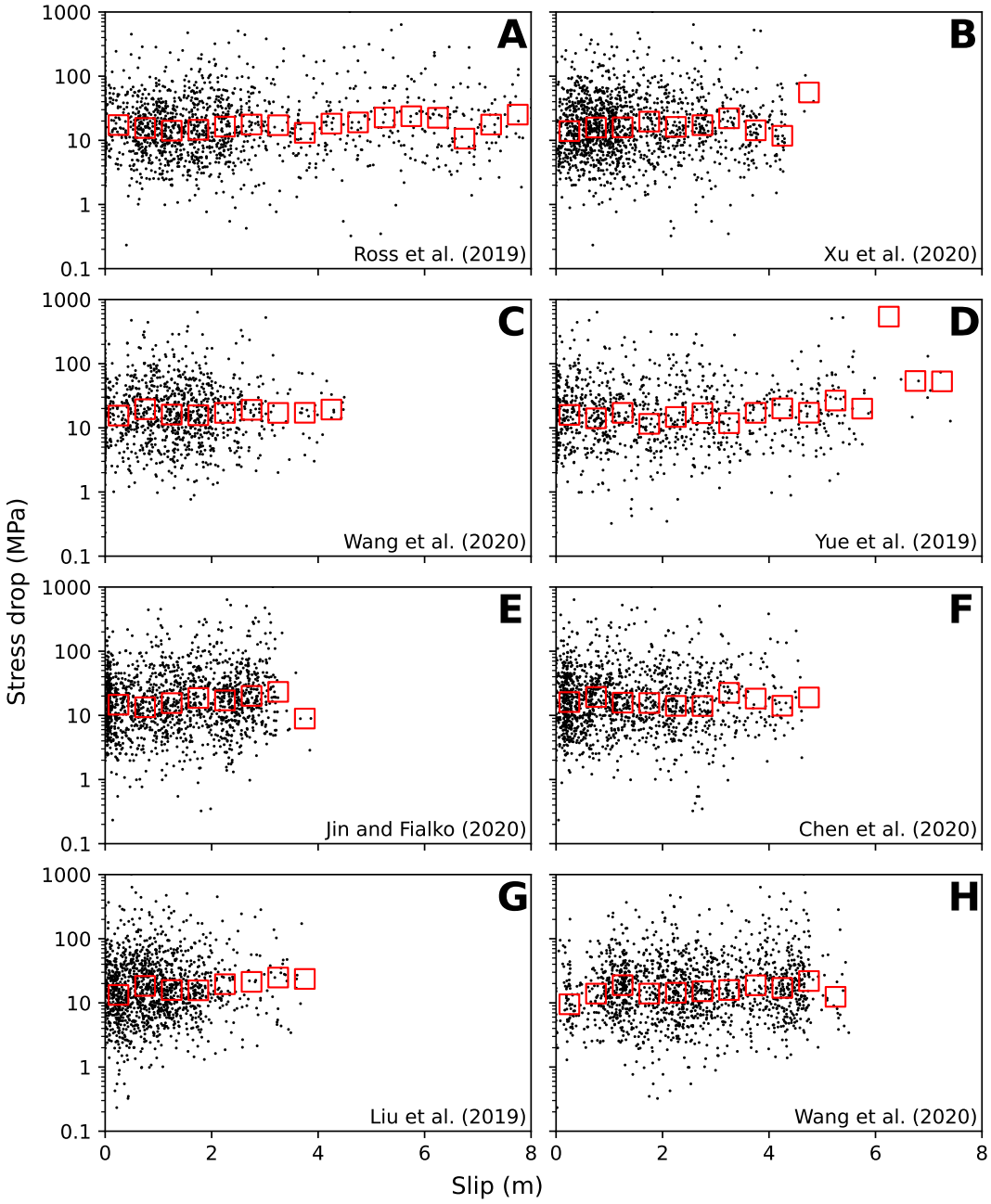


Figure 2.S7. Stress drop versus slip for eight different slip models. Models shown in panels A–C use geodetic data, and models shown in panels D–H use geodetic and seismic data in their inversions. Slip values are computed using the same technique in Figure 8 in the main text: slip data is projected onto the cross section and interpolated onto an equally-spaced grid using a cubic spline. Slip at each earthquake's location is then estimated by interpolating this smoothed grid to the earthquake's projection onto the cross section. The model in panel H is the same used to generate the slip contours in Figure 2.8.

Chapter 3

Using a High- to Low-Frequency Spectral Ratio to Distinguish Variations in Earthquake Source Properties

3.1 Introduction

Earthquakes can be extremely destructive because of strong ground motions, so understanding the physical causes in generating these ground motions is important for estimating seismic hazards and ultimately improving preparedness. Source spectra quantify the distribution of energy released by an earthquake at different frequencies and provide insights into rupture mechanics and ground motion modeling (*Madariaga*, 1976). Earthquake moment is related to the low-frequency level of the source spectrum, and is a fundamental measure of earthquake size (*Aki*, 1967). On average, larger earthquakes radiate more energy across all frequencies than small earthquakes. However, because of differences in their rupture dynamics, earthquakes of similar moment often vary in their high-frequency radiation output, leading to significant variations in observed peak ground velocity and acceleration (*Atkinson and Beresnev*, 1997).

Earthquake high-frequency radiation is often characterized in terms of stress drop, which is the average shear stress released over a fault during an earthquake. Earthquakes

with high stress drop generate relatively more destructive high-frequency energy than low-stress-drop earthquakes of the same magnitude, making this an important parameter in assessing seismic hazard (e.g., *Hanks*, 1979; *Hanks and McGuire*, 1981; *Boore*, 1983; *Baltay et al.*, 2013; *Baltay and Hanks*, 2014; *Yenier and Atkinson*, 2014; *Lior and Ziv*, 2017; *Trugman and Shearer*, 2018; *Abercrombie et al.*, 2021; *Parker et al.*, 2020). Stress drop is related to both the earthquake moment and fault rupture dimensions (*Kanamori and Anderson*, 1975). For many large earthquakes ($M > 5.5$), estimating stress drop is relatively straightforward because the rupture dimensions are apparent from surface offsets, geodetic constraints, aftershock patterns, and finite-slip modeling (*Hardebeck*, 2020). However, for smaller events without these observable constraints, the spectral stress drop must be estimated from seismic wave observations alone (*Brune*, 1970).

Various approaches to estimating spectral stress drops (hereafter stress drop) have been developed, including spectral decomposition (e.g., *Shearer et al.*, 2006; *Oth et al.*, 2008; *Bindi et al.*, 2009; *Trugman and Shearer*, 2017a; *Chen and Abercrombie*, 2020) and spectral ratio or empirical Green's function (EGF) methods (e.g., *Abercrombie*, 2014; *Abercrombie et al.*, 2017; *Pennington et al.*, 2021; *Huang et al.*, 2016, 2017; *Liu et al.*, 2020; *Shaw et al.*, 2016). While these methods can resolve relative stress drop among different events, many suffer from parameter tradeoffs that result in unreliable absolute levels of stress drop (*Shearer et al.*, 2019). Additionally, results from the recent Ridgecrest Stress Drop Validation Study (*Baltay et al.*, 2024) show large variations in absolute stress drop between studies, even when similar analysis methods are applied. While relative stress drop may be more reliable, *Abercrombie et al.* (2025b) found that even relative stress drops of small earthquakes ($M < 2.5$) between studies are unreliable. Further, much of the variation in absolute stress drop between studies results from differences in the correction for path effects (*Shearer et al.*, 2024). However, accurately determining these path corrections is challenging because of typically strong near-surface attenuation that is difficult to measure without deep borehole observations (*Abercrombie*, 1995).

Regardless of the approach, higher stress drops in these studies arise from stronger high-frequency radiation and higher spectral corner frequencies than average for a given magnitude. Thus, we can think of relative stress drop as a proxy for the relative amounts of high-frequency radiation (*Atkinson and Beresnev*, 1997), with both related to ground motion. However, as also discussed in *Atkinson and Beresnev* (1997), stress-drop estimates require many modeling assumptions, which compromise their use in characterizing high-frequency ground motions.

Motivated by this perspective, we introduce a data-driven approach to measure relative differences in the amount of high-frequency energy from earthquakes that requires no assumptions about the source dynamics or an attenuation model. We compute this quantity, which we term the normalized frequency index (nFI), for aftershocks of the 2019 Ridgecrest, California, and find coherent spatial variations in source properties. Our nFI values correlate strongly with stress-drop estimates from prior studies in the Ridgecrest Stress Drop Validation Study (*Abercrombie et al.*, 2025a), but are not intended to be a proxy for stress drop. Instead, nFI measurements can be used to directly quantify relative levels of high-frequency radiation from earthquakes and study their spatial variations. To put our results in context, we compare our Ridgecrest results to synthetic experiments, explore similarities and differences with stress-drop estimates, and consider implications for further study.

3.2 Data

We use the dataset from the Ridgecrest Stress Drop Validation Study (*Baltay et al.*, 2024; *Abercrombie et al.*, 2025a) to demonstrate our new approach. The dataset includes waveforms of 12,943 earthquakes above magnitude (M) 1 that occurred between 4 and 18 July 2019 near the M 7.1 Ridgecrest mainshock on 5 July 2019 (see Fig. 3.1). These earthquakes were relocated using waveform cross-correlation (*Trugman*, 2020), and their

waveforms are archived at the Southern California Earthquake Data Center (*SCEDC*, 2013). Most catalog magnitudes are assigned local magnitudes (M_L), while some larger ($M > 3.3$) events are assigned moment magnitudes (M_W). The Southern California Seismic Network operates both broadband and strong motion stations, which record velocity and acceleration waveforms, respectively. We resample all seismograms to 100 Hz.

We apply a multitaper method (*Prieto et al.*, 2009) to compute P- and S-wave spectra of all records, utilizing vertical components for the P-wave spectra and horizontal components for the S-wave spectra. Following *Shearer et al.* (2022), we use time windows of 1.5 seconds for $M \leq 1.4$ earthquakes, increasing linearly to 4.5 seconds for $M \geq 4.7$ events. If necessary, the spectra are resampled at a frequency interval of $\Delta f = 2/3$ Hz, corresponding to the frequency resolution of a 1.5 second time window, to ensure equally-sampled spectra. The signal window is defined as starting 0.15 seconds before a P- or S-wave arrival, and the associated noise window immediately precedes the signal window with equal length. Phase arrivals are obtained from the catalog picks when available or predicted using event origins and a local 1D velocity model (*Hadley and Kanamori*, 1977; *Vandevert et al.*, 2024). All spectra are converted to displacement spectra.

The spectra are screened for quality using the signal-to-noise ratio (SNR), computed from the spectral ratio of the signal and noise spectra for each record. We define the SNR as the median signal to noise spectral ratio between 2.67 and 6.00 Hz and discard spectra with SNR less than 3. To avoid selection bias towards events with stronger high-frequency radiation, we do not impose an SNR threshold above 6 Hz (*Shearer and Abercrombie*, 2021). Additionally, we exclude spectra with epicentral distances greater than 100 km.

3.3 Methods

We investigate relative differences in high-frequency radiation of the Ridgecrest earthquakes by computing the difference in logarithmic spectral level within high- and

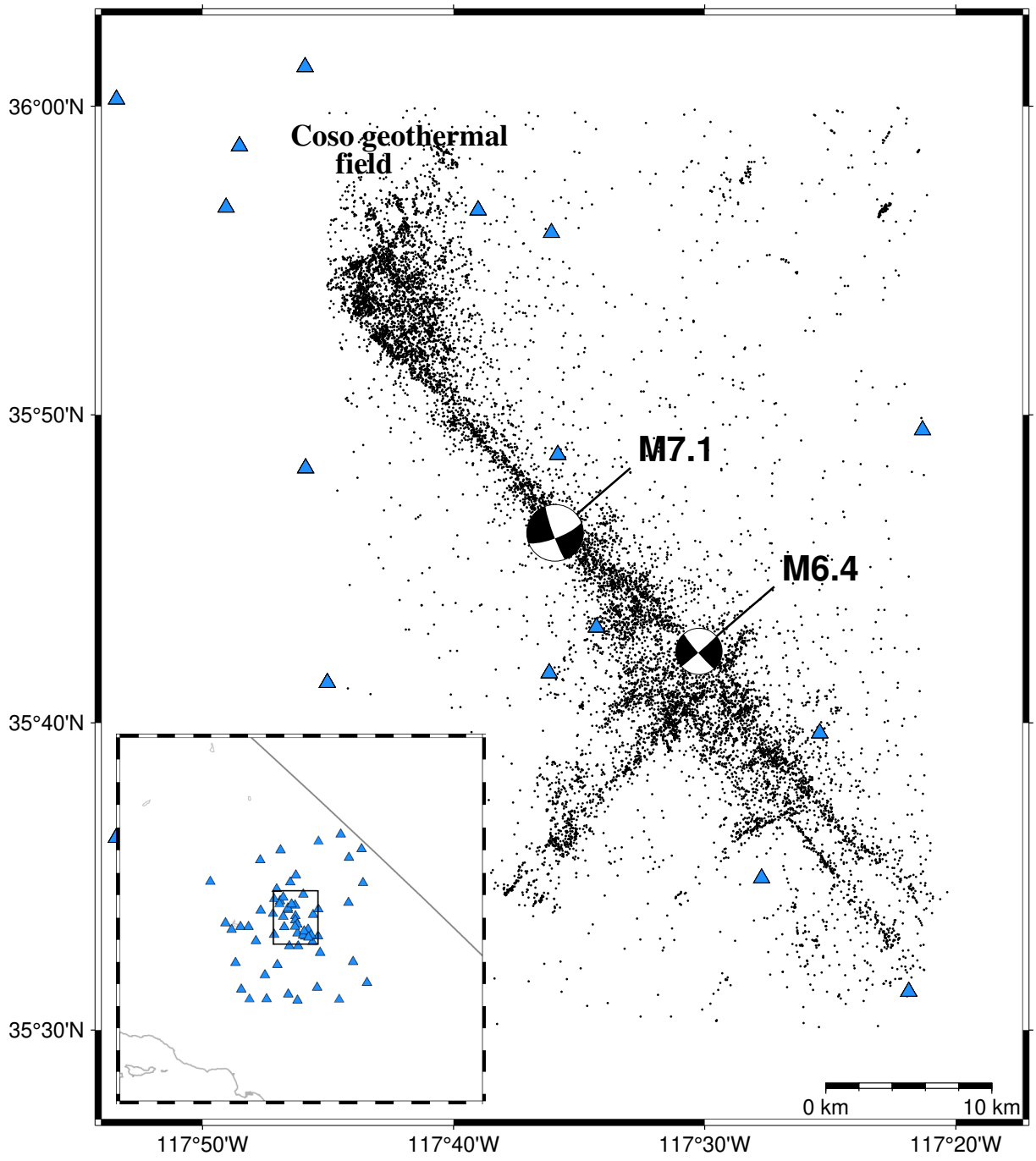


Figure 3.1. Map of the seismicity in the study area from 4 through 18 July 2019. The focal mechanisms of the M 7.1 and M 6.4 events are plotted at their epicenters. The greater southern California region is shown in the inset with locations of seismic stations used in this study.

low-frequency bands. For a given seismic spectrum, we define $\log \beta$ as:

$$\log \beta = \log_{10} \mathrm{A_{HF}} - \log_{10} \mathrm{A_{LF}}, \tag{3.1}$$

where A_{LF} and A_{HF} are the median spectral amplitudes in predefined low- and high-frequency bands, respectively (see Fig. 3.2). This parameter represents the relative amount of high-frequency amplitude compared to the low-frequency amplitude in an observed displacement spectrum. This definition of $\log \beta$ is nearly identical to the frequency index used in volcano seismology (FI, *Buurman et al.*, 2010), except that FI is instead computed using mean amplitudes. We differentiate the definitions here, as $\log \beta$ is an intermediate data product that will be corrected for various effects, while FI generally have few or no corrections applied. In the Discussion section we compare similarities between FI and our method.

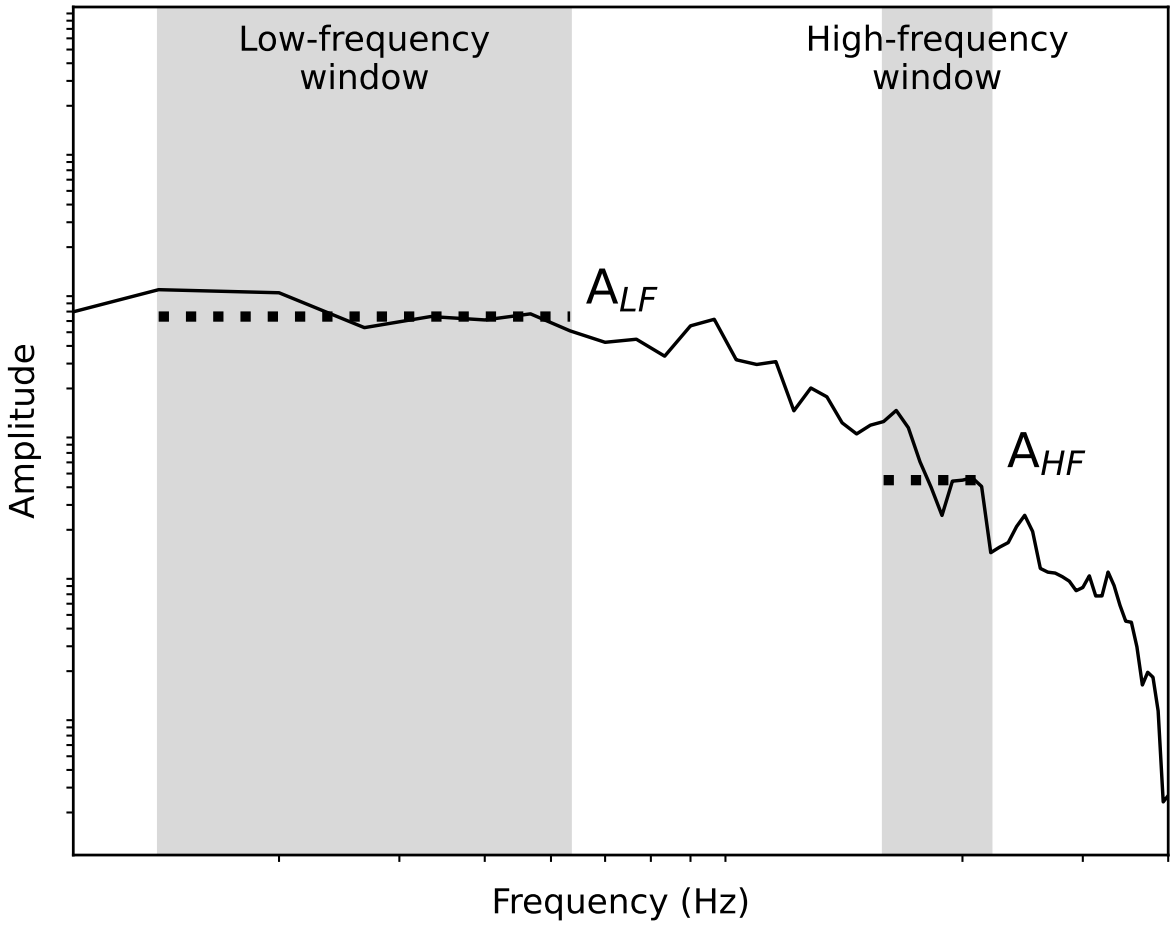


Figure 3.2. The normalized frequency index method compares the median amplitude in a high-frequency window (A_{HF}) to that in a low-frequency window (A_{LF}). Our study uses low- and high-frequency windows of 1.33–5.33 Hz and 15.33–22.0 Hz, respectively.

The choice of frequency bands for computing $\log \beta$ affects the functional magnitude range and the number of events that pass signal-to-noise criteria. For the Ridgecrest dataset, we choose a consistent low-frequency band of 1.33–5.33 Hz, and a high-frequency band of 15.33–22.0 Hz for both P and S waves. Both bands are generally recorded with good signal-to-noise in this dataset. We explore the impacts of these choices later in the Discussion section; however, this method is relatively insensitive to small changes in band.

Three main factors influence computed $\log \beta$ values: path effects and attenuation, site effects, and variations in source mechanics, including magnitude. A recorded spectrum of a distant earthquake will generally be more depleted of high-frequency energy and have a lower $\log \beta$ than that of a nearer earthquake, since high frequencies are more readily attenuated. Many spectra recorded at the same station are subject to similar near-station effects and the same instrument response, resulting in a corresponding shift in their $\log \beta$. For example, an area surrounding a station that attenuates high-frequencies more than average will result in systematically lower $\log \beta$. Further, smaller magnitude events generally have shorter source durations and therefore higher corner frequencies, resulting in larger $\log \beta$ values on average. The remaining variability is due to differences in rupture mechanics, which we attribute to differences in source duration, rupture speed, and slip area. These combined effects are typically reflected in earthquake corner frequency and spectral stress drop.

To begin isolating this source variability, we model observed spectra as a product of the earthquake's source spectrum, near-station effect term, and path effect term (e.g., *Andrews*, 1986; *Shearer et al.*, 2006; *Abercrombie*, 2021). In the logarithmic domain, this becomes a sum of each term. Here, we apply the same model but modified for $\log \beta$:

$$\Delta \log \beta_i = \log \beta_{ij} - S_j - P_{q(i,j)} \tag{3.2}$$

where $\log \beta_{ij}$ is the $\log \beta$ recorded from event i at station j, S_j is the near-station effect

term for station j, $P_{q(i,j)}$ is the path term between event i and station j, and $\Delta \log \beta_i$ is the source-specific contribution to $\log \beta$ representing source variability.

To determine $\Delta \log \beta_i$, we apply an empirical correction to each target event using smaller, nearby earthquakes termed "calibration events". This is analogous to methods applied in some spectral decomposition and spectral ratio studies for earthquake stress drops (e.g. *Abercrombie*, 2014; *Pennington et al.*, 2021; *Shearer et al.*, 2022; *Ruhl et al.*, 2023; *Vandevert et al.*, 2024), which have proven successful in correcting for path, attenuation, and site effects. For each target event, we select calibration events located within 10 km in epicentral distance and 2 km in hypocentral depth, with magnitudes between M 1.4 and 1.6 for P-wave calibration events and between M 1.9 and 2.1 for S-wave calibration events. The same calibration event parameters were used in *Vandevert et al.* (2024) to estimate stress drops of these earthquakes using a spectral decomposition method. This calibration process can be represented as the following:

$$\Delta \log \beta_{ij} = \text{median}_k \left(\log \beta_{ij} - \log \beta_{kj} \right), \tag{3.3}$$

where the station-specific $\Delta \log \beta_{ij}$ is defined as the median of pairwise differences between the target event and all nearby calibration events. This can be thought of as a single station's contribution to $\Delta \log \beta_i$. The $\log \beta_{ij}$ refers to target event i recorded at station j, and $\log \beta_{kj}$ represents the kth of the calibration earthquakes near event i, also recorded at station j. By computing $\Delta \log \beta_{ij}$ for all stations that record event i and with sufficient calibration earthquakes, we compute the $\Delta \log \beta$ for the target earthquake as:

$$\Delta \log \beta_i = \text{median}_j(\Delta \log \beta_{ij}). \tag{3.4}$$

This procedure is applied to all earthquakes in the dataset, including those used as calibration events for other target events. We require target earthquakes to be recorded by

at least 10 stations and have 10 or more nearby calibration events for robustness. For a single target event and multiple calibration events, the computed $\log \beta$ at a single station will contain similar path and station effects. This approximation relies on the calibration events being sufficiently close to the target event to have the same path effects, and allows us to obtain $\Delta \log \beta$ for each target earthquake. Some path, site, or station effects could remain even after this procedure, however, especially in regions with heterogeneous subsurface effects.

The $\Delta \log \beta$ are magnitude-dependent, mainly due to larger earthquakes releasing less high-frequency energy relative to their low-frequency energy on average. To compare earthquakes across different magnitudes, we apply a single, global magnitude correction curve to $\Delta \log \beta$ to obtain nFI. This magnitude correction is constructed as the median $\Delta \log \beta$ of earthquakes within magnitude bins of width M 0.2, smoothed with a Savitzky-Golay filter of order 3. The nFI for each earthquake is obtained by subtracting the magnitude correction from each $\Delta \log \beta$. These nFI estimates characterize relative differences in earthquake high-frequency radiation, providing a model- and magnitude-independent metric of source properties. Negative nFI values indicate lower-than-average high-frequency radiation relative to earthquakes of the same magnitude, while positive values suggest the opposite. However, due to the difficulty in removing near-source or near-surface attenuation, we cannot wholly rule out their contribution to variability in nFI.

3.3.1 Uncertainty Quantification

An earthquake's computed nFI depends upon the specific set of stations that record it and the calibration events used to correct for path and station effects. Since the magnitude correction from $\Delta \log \beta$ to nFI for a single event is additive, uncertainty in $\Delta \log \beta$ directly translates to uncertainty in nFI. We take advantage of this to estimate

uncertainty in $\Delta \log \beta$ empirically using residuals from the median $\Delta \log \beta_{ij}$ (Eqn. 3.3),

$$\mathrm{U}_i = \bigcup_{j=1}^{N_j} \{[\log \beta_{ij} - \log \beta_{kj}] - \Delta \log \beta_{ij}\}, \tag{3.5}$$

where U_i is the zero-median uncertainty distribution, and N_j is the number of stations. Note that $[\log \beta_{ij} - \log \beta_{kj}] - \Delta \log \beta_{ij}$ simply represents the zero-median set of differences between $\log \beta$ of a target earthquake and $\log \beta$ of its calibration events at a single station. Combining the residuals of all stations produces U_i, to which an event's $\Delta \log \beta$ or nFI may be added to obtain uncertainty distributions.

3.4 Results

We obtain nFI estimates for 10,690 earthquakes using P-wave spectra, which includes 1,582 calibration earthquakes. The processing steps are illustrated in Fig. 3.3, with panel (a) showing all 296,418 P-wave $\log \beta$ measurements from individual seismograms as a function of magnitude. The $\log \beta$ values decrease with magnitude and have large scatter, reflecting the presence of path, station, and source effects. The scatter is greatly reduced after applying path and station corrections to obtain $\Delta \log \beta$ (Fig. 3.3b), but a clear magnitude dependence remains. We subtract the magnitude correction (see Methods section) to get magnitude-independent nFI values (Fig. 3.3c).

The nFI values are approximately normally distributed with a standard deviation of 0.16, and 1st and 99th quantiles of -0.45 and 0.32 respectively. The spread of nFI varies with magnitude, with a larger spread observed for earthquakes between magnitudes 2 and 4. This pattern likely reflects the influence of the selected high- and low-frequency bands, which bracket the high-frequency fall-off transition for $M2$—4 earthquakes. We further examine this effect in the Discussion section using synthetic tests.

Using S-wave records, we resolve nFI estimates for 11,274 earthquakes, which includes 1,083 calibration earthquakes. We do not show a separate S-wave version of

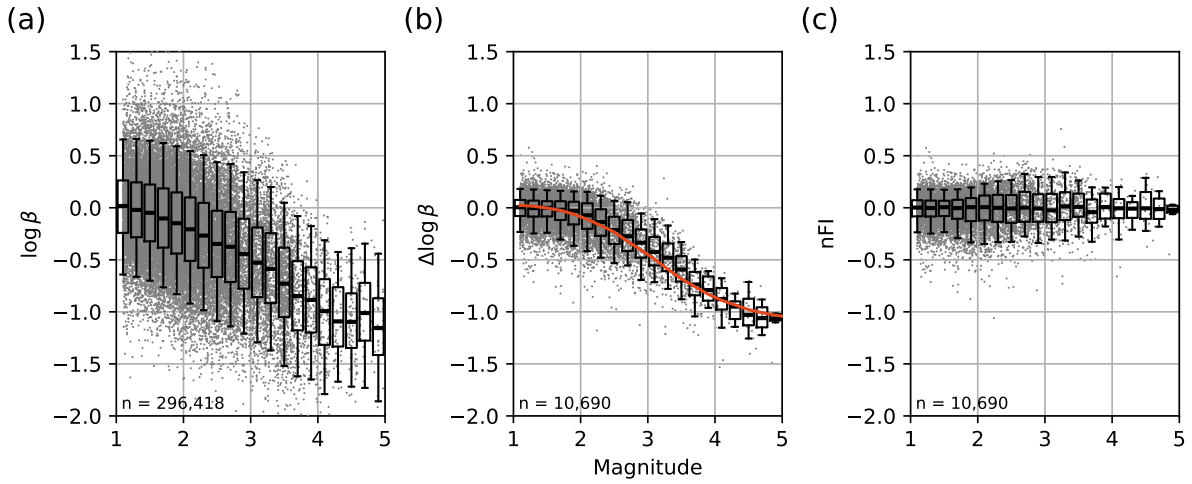


Figure 3.3. Different processing stages to obtain nFI for P waves: (a) all $\log \beta$ values from 296,418 individual spectra before any corrections; (b) station- and path-effect-corrected $\Delta \log \beta$ values for 10,690 events; and (c) magnitude-corrected nFI values. Black boxes show the 25th and 75th percentiles of the plotted data, and whiskers represent the 5th and 95th percentiles. For clarity, only every 10th record is plotted in panel (a). The red curve in panel (b) depicts $\Delta \log \beta$ of M-1.7N synthetic spectra with falloff rates of n=1.7 and added seismic noise.

Fig. 3.3 since the S-wave results have similar trends with respect to magnitude. The nFI values have a similar normal distribution, with a standard deviation of 0.15 and 1st and 99th quantiles of -0.41 to 0.36, respectively. The S-wave nFI are positively correlated with the P-wave nFI with a slope of approximately one (Fig. 3.4). For earthquakes with $M > 2$, the correlation coefficient is stronger with $r = 0.655$, while earthquakes with $M < 2$ have $r = 0.600$, suggesting that nFI differences are better resolved for larger earthquakes. This is expected, given that the calibration process locally forces the small calibration events to have the same average nFI.

Both the P-wave and S-wave results display similar, coherent spatial variations on the scale of kilometers (Fig. 3.5a-b). A region near the Coso geothermal field (polygon P1, Fig 3.1) exhibits low average nFI values, indicating that the corresponding earthquakes are relatively depleted in high-frequency radiation. In contrast, the central section of the Ridgecrest fault system is characterized by positive nFI values (polygon P2, Fig. 3.5,

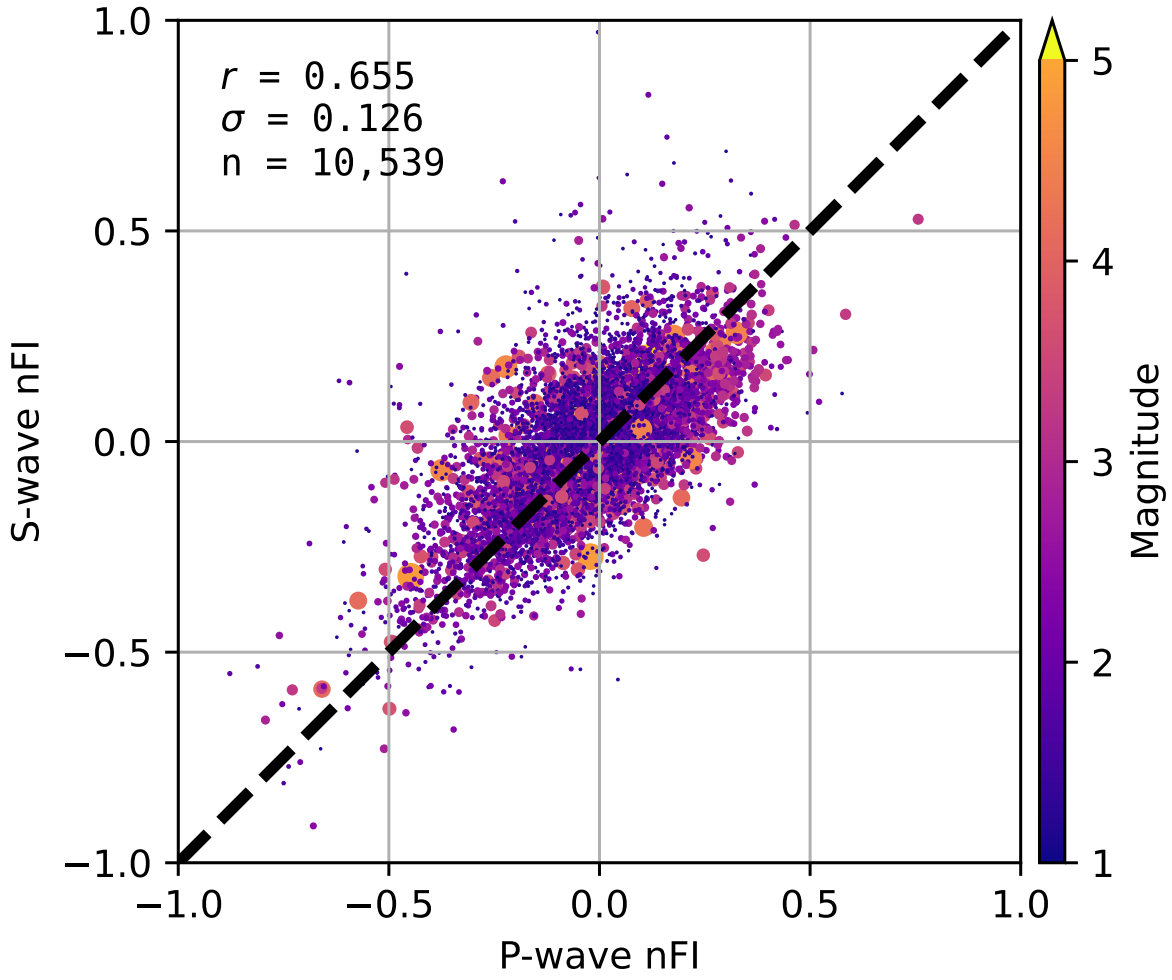


Figure 3.4. Comparison of P-wave and S-wave nFI values. The dashed diagonal line has a slope of one. The Pearson's correlation coefficient ($r = 0.655$) and the standard deviation ($\sigma = 0.126$) are computed for all earthquakes ($n = 10,539$) that have both P- and S-wave estimates of nFI. Earthquakes between about M 2 and M 3.5 have the highest correlation ($r \approx 0.73$), while outside this range correlation falls off to about $r = 0.55$ near M 1 and about $r = 0.6$ near M 4.5. Marker size is proportional to catalog magnitude.

suggesting earthquakes here are enriched in high-frequencies. These spatial patterns are locally coherent and do not appear to be random. We do not find a significant correlation with hypocentral depth in either dataset.

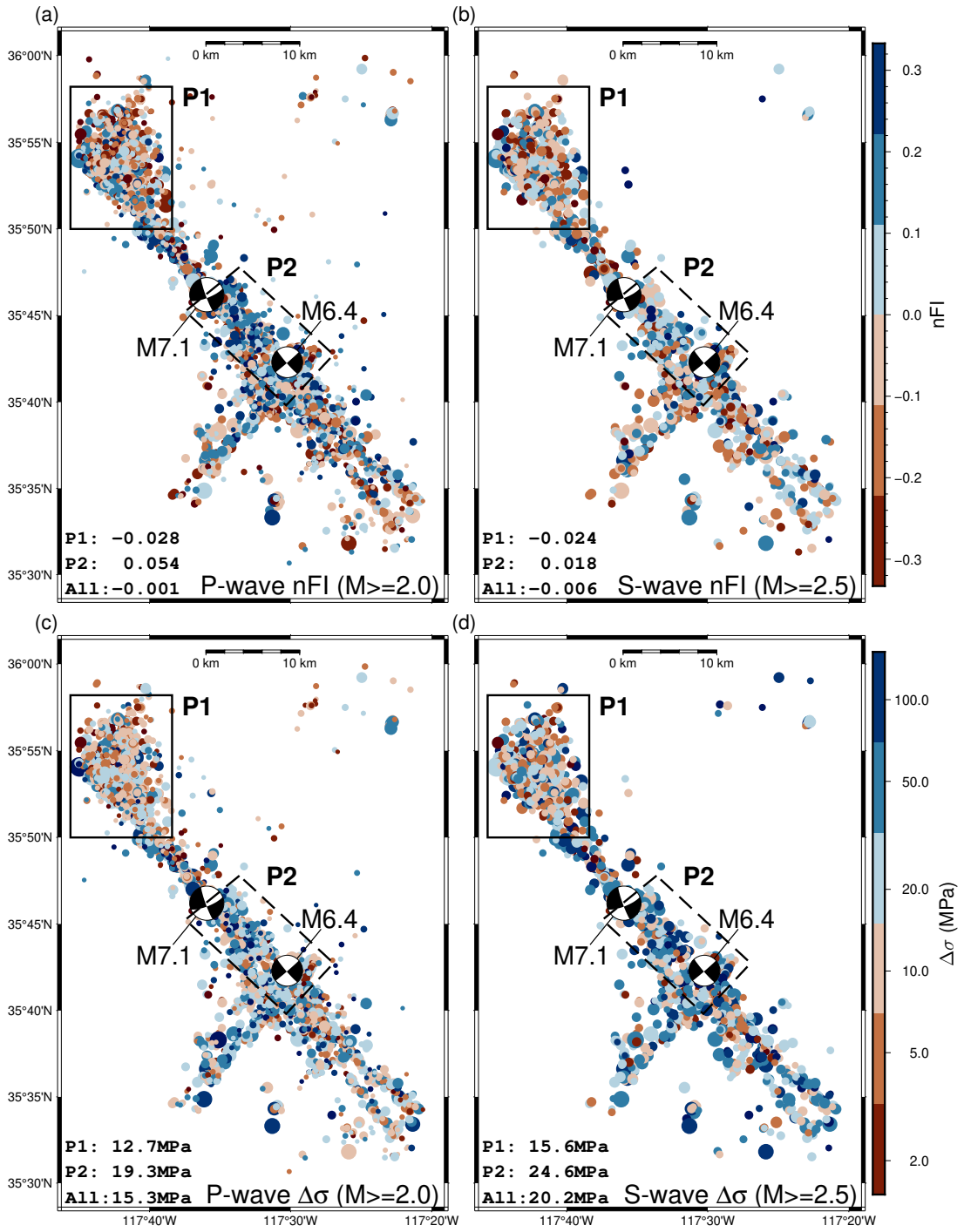


Figure 3.5. Maps showing spatial variations in earthquake high-frequency radiation for the Ridgecrest aftershocks as measured by the normalized frequency index (nFI) parameter and stress drop ($\Delta\sigma$) from *Vandevert et al.* (2024). Blue and red indicate, respectively, greater and lesser nFI and stress drop. (a) P-wave nFI results; (b) S-wave nFI results; (c) P-wave $\Delta\sigma$; and (d) S-wave $\Delta\sigma$. Only $M \geq 2$ events are plotted for P waves and $M \geq 2.5$ events for S waves. The annotations in the bottom left of each panel represent average nFI or $\Delta\sigma$ for polygons P1 and P2, and all events plotted. Marker size is proportional to catalog magnitude.

3.5 Discussion

Fundamentally, nFI is an empirical quantification of the relative intensity of earthquake high-frequency radiation. While some parameters are required to compute nFI, such as the frequencies of the bands and calibration earthquake search parameters, no physical rupture model is required in this process. As such, it quantifies relative high-frequency enrichment and ground motions more directly than model-dependent approaches, such as stress-drop estimation techniques. However, it is not designed to be a proxy for other source parameters, and absolute nFI values have a complex physical meaning dependent on parameter choices. Due to the novelty of this method and the uncertainties in existing source parameter estimation methods, it is difficult to design an independent validation of the meaning of nFI variations. In principle, nFI could correlate with ground motion metrics like peak ground acceleration since it is more closely related to ground motion than stress drop is, but we defer these comparisons to future work. Because nFI is a measure of the relative strength of high-frequency radiation from each target event compared to small calibration events in nearly the same location, to first-order it should be insensitive to path and site effects. However, because the calibration events are not in exactly the same locations as the target events, some leakage of non-source effects may occur and could contribute to observed variations in nFI.

3.5.1 Relation between nFI and Stress-Drop Estimates

The purpose of our nFI method is to characterize variations in earthquake high-frequency radiation, not to estimate stress drop. However, not surprisingly, both P- and S-wave nFI correlate with the stress-drop estimates of the Ridgecrest earthquakes from several groups. We directly compare our nFI to available results from *Abercrombie et al.* (2025a) in the electronic supplement, Fig. S3, and compare to the *Vandevert et al.* (2024) stress drops in Fig. 3.6c-d. The correlation between nFI and stress drop also depends on

event magnitude range, spatial distribution of earthquakes and stations, and the stress-drop catalog and its assumed source model parameters. Although maximizing correlation with stress drop is not the primary goal of this study, the observed correlations confirm that nFI is useful in distinguishing relative levels of high-frequency radiation of earthquakes. For P-wave nFI, the correlation coefficient is $r = 0.704$, and $r = 0.616$ for S-wave nFI. Correlation is observed between nFI and stress-drop estimates from different methods (see *Abercrombie et al.*, 2025a, for individual study descriptions), and is stronger in spectral decomposition studies. In general, the medium-sized events ($M2$–$M5$) correlate better than the smaller events.

Spatially, our nFI results agree with regional patterns in stress-drop estimates found in both *Vandevert et al.* (2024) and *Abercrombie et al.* (2025a). Many of those groups found low values of $\Delta\sigma$ near the Coso geothermal field and high $\Delta\sigma$ along the cross-fault section of the Ridgecrest fault system, as also observed in the nFI distributions (Fig. 3.5). For simplicity, further comparison with $\Delta\sigma$ and f_c solely uses results from *Vandevert et al.* (2024), who analyzed the same spectral dataset with the spectral decomposition approach from *Shearer et al.* (2022). This method assumes a fixed f_c for a narrow magnitude range of small, nearby calibration events for every target event, thus stabilizing the spectral decomposition method. This approach likely dampens the scale of true $\Delta\sigma$ variations by forcing the small calibration events to have the same average $\Delta\sigma$ everywhere, but has the advantage that any remaining variations in relative $\Delta\sigma$ must be real. *Shearer et al.* (2022) applied this method to analyze southern California seismicity between 1996 and 2019 and identified clear spatial variations in average $\Delta\sigma$, reflecting differences in the amount of high-frequency radiation among similar sized earthquakes.

The strong correlation between corner frequency and the magnitude-dependent $\Delta \log \beta$ is primarily due to f_c scaling with earthquake magnitude. The correlation is approximately linear when the estimated f_c is between the outer limits of the two frequency windows (1.33–22 Hz), corresponding roughly to earthquakes of $2 < M < 4.5$. This linearity

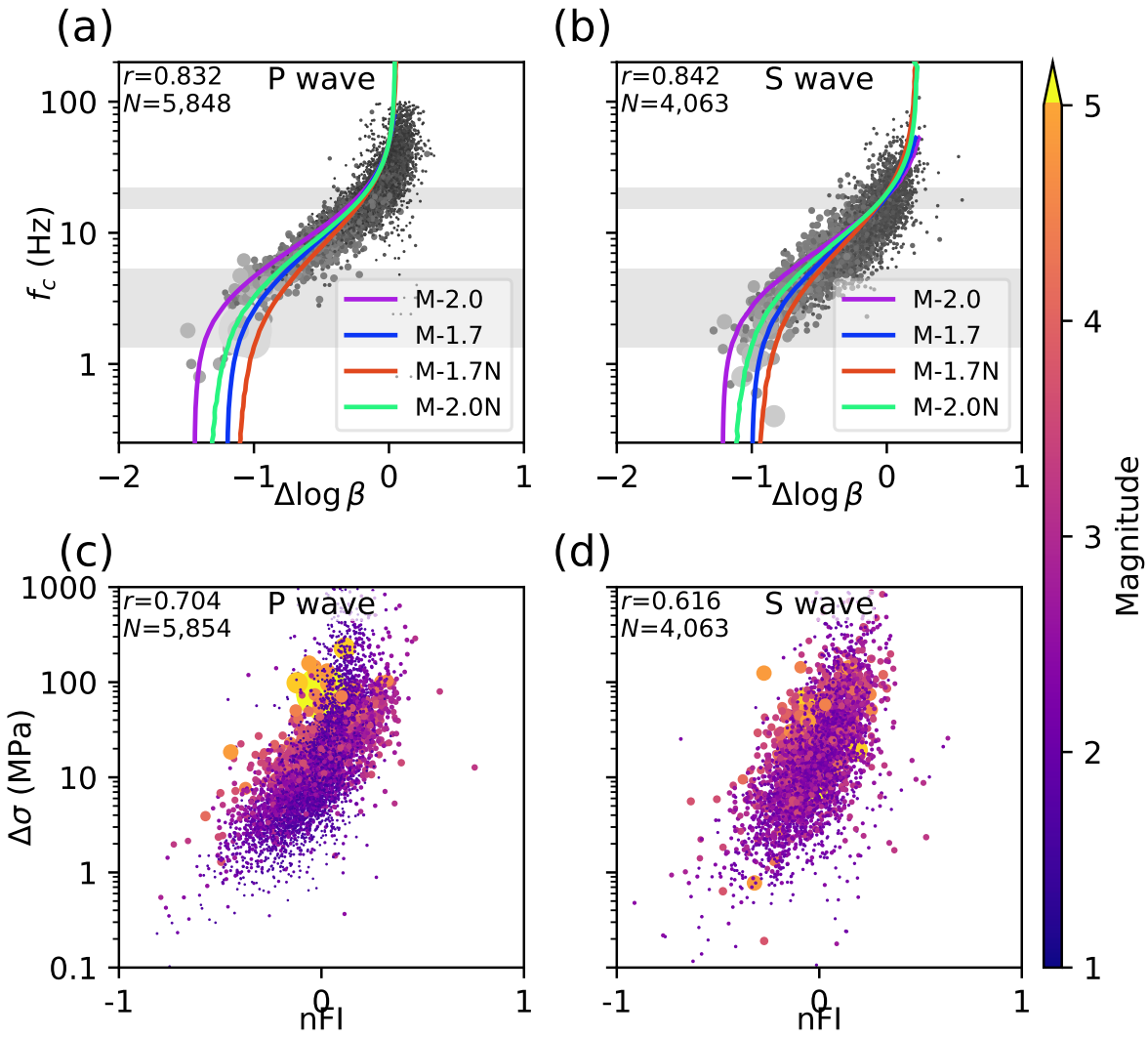


Figure 3.6. Relationships between corner frequency and stress drop from *Vandevert et al.* (2024) compared to the $\Delta \log \beta$ and nFI values obtained in this study. P-wave results are presented in the left column, and S-wave results in the right. The top row compares f_c to the magnitude-dependent $\Delta \log \beta$, and the bottom row compares $\Delta\sigma$ to the magnitude-corrected nFI. Outlier populations of high $\Delta\sigma$ events ($\Delta\sigma > 1$ GPa; $n = 245$ for P waves, $n = 133$ for S waves) are not shown in any panel, mostly consisting of small events with high uncertainty in $\Delta\sigma$. Median f_c versus $\Delta \log \beta$ from the four synthetic models are shown as color lines in panels (a) and (b). Pearson correlation coefficients (r) and number of events plotted (N) are shown in each panel. In panels (a) and (b), gray rectangles represent the low- and high-frequency bands used to compute $\log \beta$, and the markers are converted to grayscale to better show the synthetic curves. Marker size is proportional to catalog magnitude.

breaks down for earthquakes beyond this range, as seen most clearly in Fig. 3.6 a-b for the smallest earthquakes above the high-frequency band (gray box). For these events, $\Delta \log \beta$ exhibits little change for increasingly higher corner frequencies. This behavior is expected when f_c begins to well-exceed the 15.33–20 Hz upper frequency band, where increasingly higher f_c produces diminishing changes in amplitude in the band. A similar saturation effect is seen for values of f_c below our 1.33 to 5.33 Hz low-frequency band, in which both the high- and low-frequency bands are within the f^{-n} part of the displacement spectrum. Later we will show how this behavior is predicted in synthetic experiments that produce the curves in Fig. 3.6 a-b. Indeed, an advantage of our approach for characterizing high-frequency radiation differences among earthquakes is that $\Delta \log \beta$ directly scales with these differences, while f_c and inferred stress drop have a strong non-linear dependence on high-frequency radiation in any fixed band.

The correlation between nFI and stress-drop estimates varies with magnitude and seismic phase. For intermediate magnitudes (approximately $2.5 < M < 5$), $\Delta\sigma$ estimates scale linearly with nFI, while both larger and smaller magnitudes have more complex scaling due to their f_c lying outside the $\log \beta$ frequency bands. Within the intermediate range, P-wave $\log \Delta\sigma$ scale with nFI at a shallower slope than S-wave $\log \Delta\sigma$ (Fig. 3.6c-d). This slope difference is likely due to how $\Delta\sigma$ was estimated in *Vandevert et al.* (2024), in which P-wave spectra were fit with Brune models and S-wave spectra were fit with $n = 1.8$ falloff rate models. This falloff difference followed *Kaneko and Shearer* (2014) who found that, for a circular fault model, S-wave spectra have a lower falloff rate than P-wave spectra. Based on our synthetic results below, spectra with systematically lower falloff rates result in a steeper slope for $\Delta\sigma$ versus nFI, which appears to explain the difference between the P-wave and S-wave results in Fig. 3.6. However, the exact relationship between stress drop and nFI is complicated and magnitude-dependent, so we do not estimate it quantitatively here.

The nFI is a more direct measurement of high-frequency variation between events

than stress drop. We note that the smaller $M < 2$ earthquakes span a wide range of the P-wave stress-drop values, including cases exceeding 100 MPa, whereas their corresponding nFI values derived from P waves have less scatter (see Fig. 3.3). The S-wave results display a similar effect, although fewer $M < 2$ earthquakes have $\Delta\sigma$ estimates as shown in Fig. 3.6d. Perhaps unsurprisingly, the populations of earthquakes with abnormally large stress drops also have higher uncertainty in nFI. While the stress-drop estimates of earthquakes under $M2.5$ are largely unreliable due to their high f_c (*Abercrombie and Baltay*, 2025), we find coherent spatial variation in nFI similar to Fig. 3.5a-b even in earthquakes less than $M2.5$.

Variation in nFI and relative $\Delta\sigma$ are both strongly related to differences in high-frequency earthquake radiation, demonstrated above and through the close agreement between our nFI map (Fig. 3.5) and spatial $\Delta\sigma$ distributions obtained by several independent methods (e.g., *Trugman*, 2020; *Bindi et al.*, 2020b; *Knudson et al.*, 2025; *Ahn et al.*, 2025). We show these comparisons not to validate or invalidate our approach, as spectral stress-drop estimates are only indirectly related to high-frequency radiation intensity, but to test whether the spatial variations seen in some stress-drop studies of Ridgecrest are also visible in our nFI maps. Even though it does not result from a physical rupture model, the nFI provides a direct measure of relative differences in high-frequency radiation among earthquakes without making assumptions about the dynamics of the source, such as required for traditional stress-drop estimates. We find correlation between the P-wave and S-wave datasets without parameter tuning. The intermediate data product $\Delta \log \beta$ scales with magnitude (Fig. 3.3). In the Synthetic Experiments and Uncertainty section, we compare this relationship to theoretical predictions to infer average source spectral properties. However, since we empirically remove magnitude dependence to obtain nFI, the resulting values retain no information regarding how nFI scales with magnitude (comparable to stress drop versus magnitude scaling).

3.5.2 nFI and Frequency Index

Aspects of the nFI parameter resemble those of the frequency index (FI), which is commonly used for studying long-period earthquakes at volcanoes (e.g., *Ketner and Power*, 2013; *Matoza et al.*, 2014). FI quantifies relative frequency content of seismic events, first defined in *Buurman et al.* (2010) as:

$$FI = \log_{10} \frac{\text{mean}(\text{A}_{\text{HF}})}{\text{mean}(\text{A}_{\text{LF}})}, \tag{3.6}$$

where A_{LF} and A_{HF} are the spectral amplitudes in low- and high-frequency windows. In this format, FI is the same as $\log \beta$ (Eqn. 3.1), except that FI is computed using mean spectral amplitudes and $\log \beta$ is computed using median spectral amplitudes. *Buurman et al.* (2010) set the low- and high-frequency windows to 1-2 Hz and 10-20 Hz, respectively, in their study of $M < 1.5$ earthquakes below an Alaskan volcano. Similar frequency bands are common in other studies using FI, but are often modified to accommodate the dataset (event magnitude, station distribution, etc.).

Spatial patterns of anomalously high- or low-FI have been associated with subsurface structure and activity. At volcanoes with active magmatism, low-FI events correlate with explosive volcanic eruptions and geothermal activity due to rising fluids in the magma chamber (*Chouet*, 1996; *Buurman et al.*, 2010; *Matoza et al.*, 2014). Additionally, swarms due to induced seismicity have been found to have low-FI on average (*Salvage and Eaton*, 2022). High-FI events tend to occur in volcanic "precursory swarms", or those just before explosive eruptions, and are hypothesized to be due to rock fracturing along previously-unfractured surfaces (*Buurman et al.*, 2010). These correlations suggest that $\log \beta$ can also be associated with subsurface processes like magmatism and fluid-induced activity. The northwestern corner of our study area (Fig. 3.5) is an area with relatively low nFI values, and is part of the Coso geothermal field which has abundant geothermal features

including fumaroles and hot springs. We therefore interpret the lower nFI values in this area to be associated with these geothermal features.

Other studies have explored FI of earthquakes and its relationship with source and subsurface properties. *Matoza et al.* (2014) introduced a more robust FI metric that averaged FI computed at multiple seismic stations, indirectly correcting station and path effects in a region less than 11 by 22 km and using low- and high-frequency bands of 1-5 Hz and 5-15 Hz, respectively. Path effects and attenuation are stronger in our study because of its larger geographic scale, so we adopted a technique that directly corrects these effects. *Nakajima and Hasegawa* (2021) measured FI and stress drop of continental plate earthquakes smaller than M 2.5 in Japan. They found a correlation between stress drop and FI, and proposed high pore pressure as the mechanism controlling regions with low-FI earthquakes. *Sundod* (2024) examined long-period earthquakes that tend to appear in geothermal fields in Italy, which were identified using the frequency index technique. Together, results from these studies suggest that spatial patterns in dominantly high- or low-frequency earthquakes, and therefore nFI, can indicate fluid content or source parameter variation.

Perhaps most similar to this study, *Tsuchiyama et al.* (2022) computed FI and compared with previous corner frequency and stress-drop estimates for M $1-3$ events in the Ridgecrest area between 2015 and 2020. Their study uses different frequency bands than ours (2–5 Hz and 10–15 Hz for the low- and high-frequency bands, respectively) and does not correct station and path effects, so directly comparison to our study is difficult. However, they find that small events approach an FI of 0 and f_c versus FI is roughly linear for medium-sized events, analogous to our f_c versus $\Delta \log \beta$ results shown in Fig. 3.6 a. They also hypothesize that the presence of nearby subsurface fluids cause events to have low FI.

3.5.3 Synthetic Experiments and Uncertainty

To test our method and quantitatively evaluate the measurement uncertainties in nFI and its relation to corner frequency and stress drop, we generate synthetic displacement spectra of the form,

$$u(f) = \frac{\Omega_0}{1 + (f/f_c)^n}, \tag{3.7}$$

where Ω_0 is proportional to seismic moment M_0 and n is the high-frequency falloff rate. We consider four combinations of source models and noise, with indicated color consistent through all relevant figures:

1. M-2.0: Brune spectra with $n = 2$ and constant stress drop 5 MPa (purple),
2. M-2.0N: the same as M-2.0, but with added seismic noise (green),
3. M-1.7: a reduced-falloff model with $\Delta\sigma = 5$ MPa and $n = 1.7$ (blue), consistent with observed falloff rates in some studies (e.g., *Trugman and Shearer*, 2018),
4. M-1.7N: the same as M-1.7, but with log-normal scatter added to the stress drop and real seismic noise added to the resulting spectra (red).

No path or attenuation effects are simulated, but we generate event and station locations in a compact spatial region so that each target event has ample nearby calibration events. We simulate 100 stations and 10,000 synthetic events with moment magnitudes ranging from M_W 1.0 to 7.1. Event magnitudes follow a Gutenberg-Richter relation using $a = 1.0$ and $b = 0.3$. The unrealistically low b value ensures a sufficient number of synthetic events in each magnitude bin up to M 5.

For the M-1.7N dataset, events are assigned a stress drop drawn from a log-normal distribution with a median of 5 MPa and a standard deviation of 0.8, which is on the same order as the standard deviation of the stress-drop catalog reported in *Vandevert et al.* (2024). We then add real seismic noise to each spectrum by choosing random noise

spectra that have a corresponding signal window with a high signal-to-noise ratio. This prevents using noise windows that may contain arrivals from other events, since signal windows that passed SNR criteria are less likely to have a contaminated noise window. We then scale the noise spectrum such that the resulting spectrum has an SNR typical for a recording of an earthquake of that size. For the Ridgecrest dataset, the median SNR for M 1–2 events is about 2, while M 5 events have an SNR of about 25. We scale the seismic noise spectra accordingly and add them to the synthetic spectra.

From moment magnitude, $\mathrm{M_W}$, we compute M_0, and from stress drop we compute corner frequency,

$$f_c = \left(\frac{16}{7}\frac{\Delta\sigma}{M_0}\right)^{1/3} kV_s, \tag{3.8}$$

assuming $V_s = 3,464$ m/s for the shear-wave velocity and $k = 0.38$ for P-wave models and $k = 0.26$ for S-wave models (*Kaneko and Shearer*, 2014). While this equation and these k-values rely on assumptions of rupture model and self-similarity, the approximation that $f_c \propto M_0^{-1/3}$ has been observed in many studies (see *Abercrombie et al.*, 2025a) and is sufficient for these simple synthetic tests. Finally, using M_0 (where $\log_{10} M_0 \propto \Omega_0$) and f_c we compute the various source spectra with Eqn. 3.7 and then apply the nFI technique to each synthetic dataset.

A synthetic illustration of the corrections is shown in Fig. 3.7, where we present the results of the M-1.7N dataset. The four synthetic models are compared directly to the real data in Fig. 3.8. Visually, M-1.7N is the best-fitting model to the real data, and we plot its median $\Delta \log \beta$ versus magnitude in Fig. 3.3 as as comparison. Since the synthetic data have no station or path effects, their $\log \beta$ have much less scatter compared to the real data, and any scatter is due to either the added seismic noise or the variation in $\Delta\sigma$. The $\Delta \log \beta$ have less scatter for the smallest and largest events, which is also observed in the real data (Fig. 3.3). This effect is due to the low- and high-frequency bands used to compute nFI and the earthquake's corner frequency, f_c. Referring back to Fig. 3.6a,

between the two frequency bands (1.33–22 Hz) absolute $\Delta \log \beta$ are mostly between -1.25 and 0.25. However, outside these frequency bands $\Delta \log \beta$ varies much less, about ± 0.25 from the median for most events. This suggests that the variability of f_c for moderate magnitude earthquakes leads to more pronounced scatter in their nFI estimates.

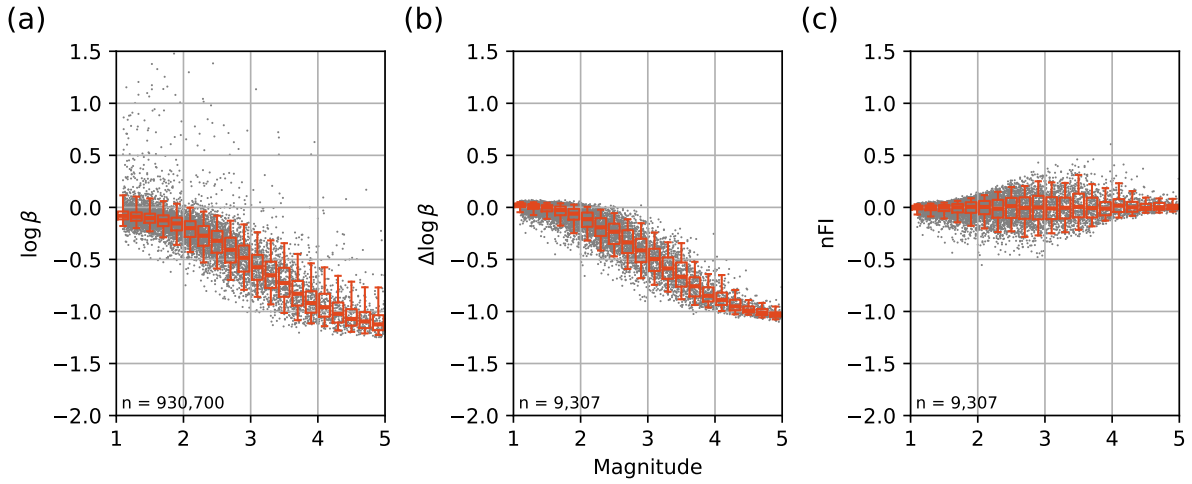


Figure 3.7. Synthetic version of Fig. 3.3 using the M-1.7N spectra. The same processing used for the real data was applied to the synthetic dataset with $n = 1.7$ falloff rate, log-normal scatter in $\Delta\sigma$, and added realistic seismic noise: (a) all $\log \beta$ records before any corrections; (b) station- and path-effect-corrected $\Delta \log \beta$ values; and (c) magnitude-corrected nFI. Box extent indicates the 25th and 75th percentiles of the plotted data, and whiskers represent the 5th and 95th percentiles. For clarity, only every 100th record is plotted in panel (a). Panel (a) has much less scatter than its real-data counterpart (Fig. 3.3 a) because there are no simulated path or station effects.

Considering $\Delta \log \beta$ versus magnitude, the M-1.7N model appears to be the closest synthetic model to the real data (see Fig. 3.8). From this figure, we find that the M-2.0 (purple) and M-2.0N (green) models under predict the amount of high-frequency energy observed in the larger real earthquakes (black dashed). Adding seismic noise to the synthetic spectra increases $\Delta \log \beta$ for the larger magnitudes (see Fig. 3.8). Increasing the noise levels strengthens this effect, however, this represents unrealistically high noise that is not observed in the Ridgecrest dataset. This indicates that in the Ridgecrest area, larger earthquakes radiate more high-frequency energy than predicted by a self-similar Brune model, in agreement with results from *Trugman and Shearer* (2017a) and *Shearer*

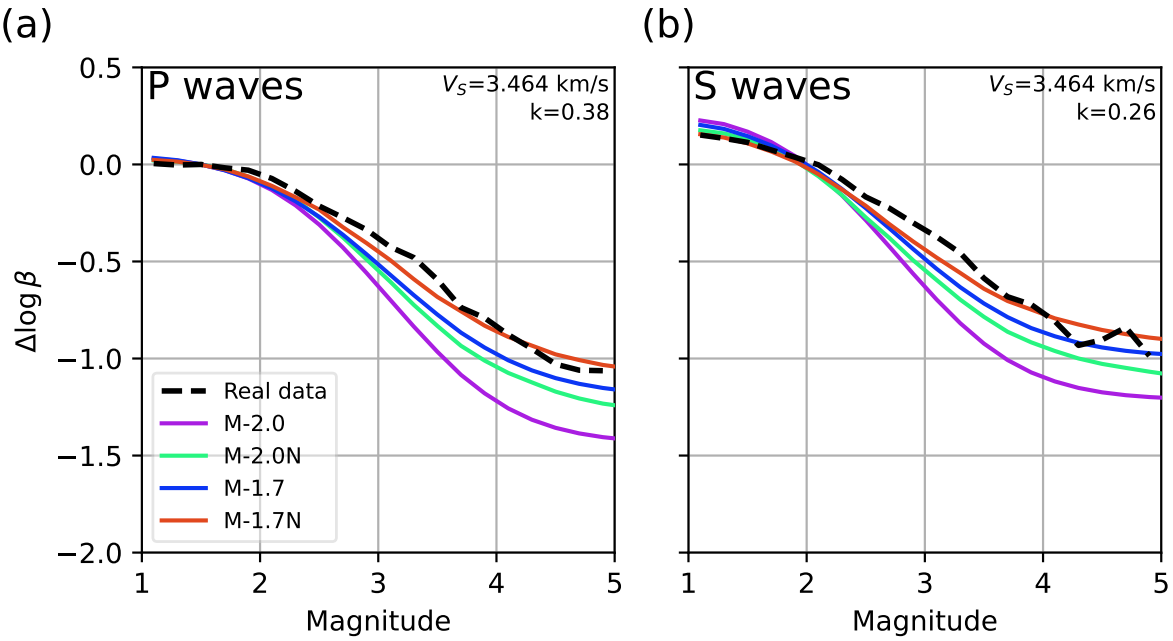


Figure 3.8. Comparison of median $\Delta \log \beta$ values in magnitude bins of M 0.2 width for real data (black dashed lines) and the four different synthetic models (color solid lines). A median stress drop of 5 MPa and P-wave and S-wave k-values from *Kaneko and Shearer* (2014) are used in the synthetics.

et al. (2019) for other regions in southern California. However, a caveat is that these synthetic models assume a constant median stress drop with respect to magnitude, i.e. self-similarity. Comparable fits to the high-frequency energy for large earthquakes can be obtained using a non-self-similar Brune model, where earthquake stress drop increases with magnitude (e.g., *Trugman and Shearer*, 2017a).

3.5.4 Parameter Choices

The final nFI values and associated correlation with stress drop are insensitive to modest changes in the frequency bands. We select low- and high-frequency bands of 1.33–5.33 Hz and 15.33–22.0 Hz, respectively, based on noise levels, physical constraints, and to have consistency between P- and S-wave datasets. These bands were initially selected to maximize the correlation between nFI and the Ridgecrest stress-drop estimates in *Vandevert et al.* (2024), for which P waves favor low and high bands of about 0.67–5.33 Hz

and 20–27.33 Hz, and S waves favors 0–4.67 Hz and 17.33–24.67 Hz. Shifting these bands by several frequency points has only a minor impact on the correlation. With high-frequency bands approaching the Nyquist frequency, the nFI values still correlate with stress drop, but with significant scatter for small events due to lower signal-to-noise ratios in the higher band. Similarly, decreasing the low-frequency band increases scatter in nFI for smaller events, though to a lesser degree. These behaviors reflect a tradeoff in which larger separation between low- and high-frequency bands broadens the effective magnitude range, at the cost of increased scatter in nFI due to noise levels in each band. Figs. S1 and S2 summarize the effects of frequency bands on the nFI and stress-drop correlation. These window choices may be region- or dataset-dependent, and some experimentation might be necessary to properly utilize available data. For example, regions with densely recorded seismicity and a lower magnitude-of-completeness than the Ridgecrest dataset could possibly use a high-frequency window higher than used here, if smaller calibration earthquakes with higher corner frequencies are used.

Based on our tests of the nFI calculation, we suggest the following guidelines before applying the procedure to new datasets:

1. Calibration magnitude range: affected by the number of calibration events, quality of records, noise level, and the high-frequency window choice. There should be ample, well-recorded, low-noise records to correct for path and station effects. Further, if the high-frequency window is too low, the high-frequency falloff of small calibration events will not be captured properly. A test using $M1 - 1.2$ calibration events produced spatial results very similar to those in Fig. 3.5a-b, even for target events under $M2$.

2. Minimum number of calibration events: if too few calibration events are used, path and station corrections could be affected by noise or calibration earthquake source effects. If too many are required, more target events will be discarded.

3. High- and low-frequency bands: ideal choices depend upon desired calibration event magnitude, noise levels, and magnitude range of dataset. The corner frequency of target earthquakes should be between the two bands; i.e., between the two bands, the spectrum should display some low-frequency level-off and some high-frequency fall-off. For the Ridgecrest dataset, this corner frequency range translates to approximately $M2$–5. Of course, this range may depend on regional geology or tectonic setting, and will need careful evaluation.

We chose the calibration event parameters used in this study to match those in the *Vandevert et al.* (2024) study for ease of comparison. Although we suggest using parameters similar ours as a starting point, ideal calibration event parameters will depend upon the data quality, catalog magnitude of completeness, distribution of stations and seismicity, sampling rate, noise levels, among other factors.

3.6 Conclusions

We have developed a new quantity, termed the normalized frequency index (nFI), for studying relative differences in high-frequency radiation from earthquakes, which requires few modeling assumptions concerning attenuation or earthquake rupture properties and is closely tied to observational data. The nFI measures the strength of source radiation within a high-frequency band relative to that in a low-frequency band, using small-magnitude calibration events near each target event to remove path and station effects. Our computed nFI values are closely related to ground motion and correlate strongly with stress-drop estimates from previous studies of aftershocks of the 2019 Ridgecrest earthquakes, but can be computed much more easily. Because we explicitly remove any magnitude dependence in our results, our nFI results cannot directly address questions of stress drop versus magnitude scaling. However, we find that spatial variations in average nFI are robust with respect to magnitude. This could prove advantageous for ground

motion modeling: some regions have systematically high or low nFI values, suggesting that those regions produce earthquakes with relatively stronger or weaker high-frequency amplitudes than average.

3.7 Data Availability and Resources

The earthquake datasets used in this study are from the Ridgecrest stress drop validation study, which can be obtained from https://scedc.caltech.edu/data/stressdrop-ridgecrest.html (last accessed July 2025).

We have archived code for this method on GitHub (https://github.com/ivandevert/py-nfi).

Acknowledgments

We thank the editors, and Annemarie Baltay and the other reviewer for their thoughtful comments, which have helped improve the study. We thank the Southern California Earthquake Center (SCEC) for supporting the Ridgecrest stress drop validation study and associated programs. SCEC is funded by National Science Foundation (NSF) Cooperative Agreement EAR- 1033462 and U.S. Geological Survey (USGS) Cooperative Agreement G12AC20038. This is SCEC Contribution 14230.

Chapter 3, in full, is a reprint of the material as it appears in *Bulletin of the Seismological Society of America*. Vandevert, I., Shearer, P. M., & Fan, W. (2026). Using a High- to Low-Frequency Spectral Ratio to Distinguish Variations in Earthquake Source Properties. *Bulletin of the Seismological Society of America* (Early Access). https://doi.org/10.1785/0120250171. The dissertation author was the primary investigator and author of this paper.

3.8 Supplementary Materials

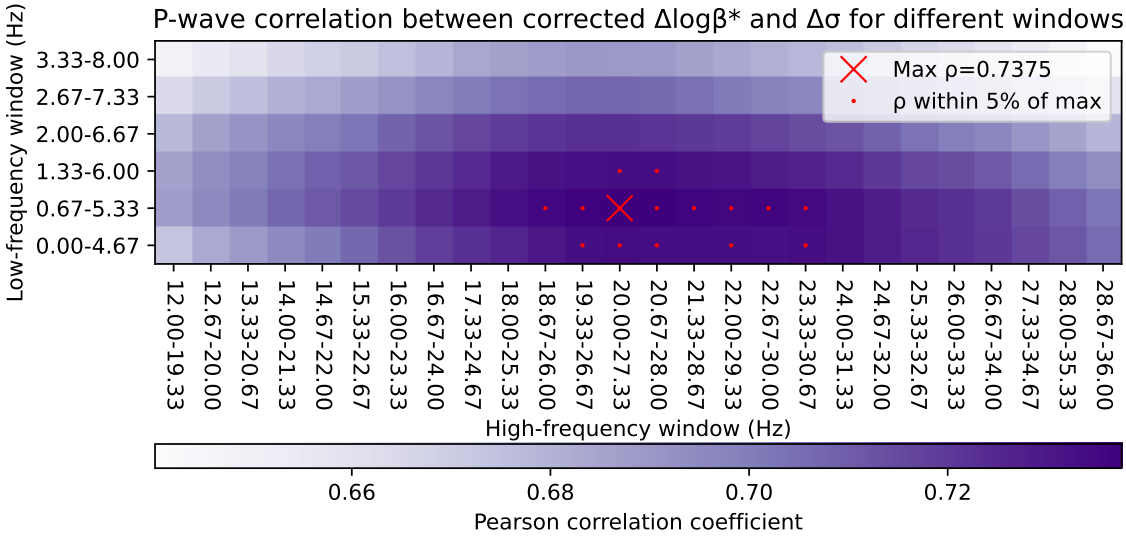


Figure 3.S1. We computed Pearson's correlation coefficient for different combinations of high- and low-frequency windows of P-wave spectra. Outliers with $\Delta\sigma$ greater than 1000 MPa or less than 0.5 MPa are discarded.

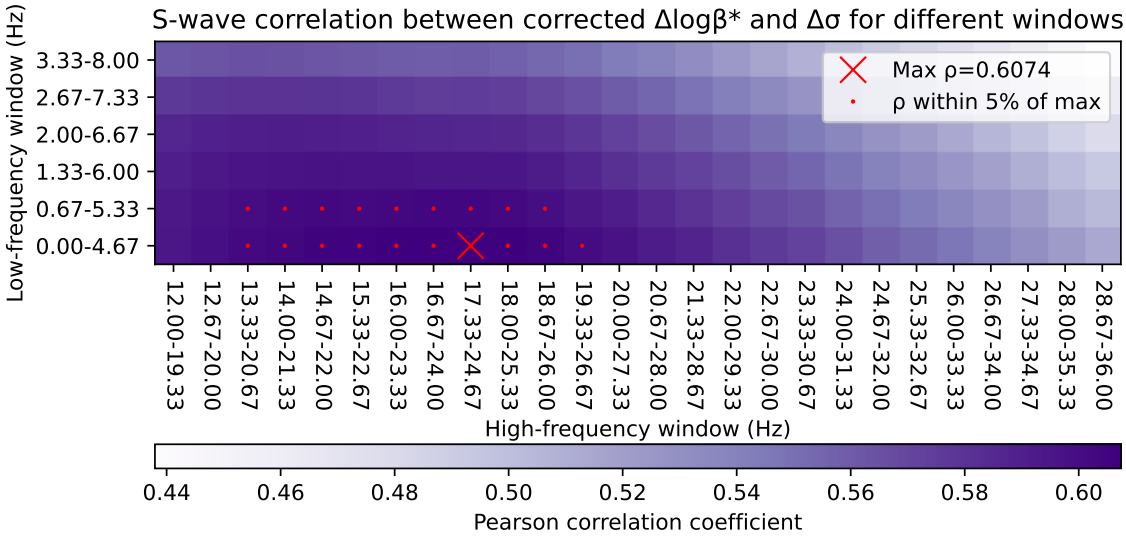


Figure 3.S2. Pearson's correlation coefficient for different combinations of high- and low-frequency windows of S-wave spectra. Outliers with $\Delta\sigma$ greater than 1000 MPa or less than 0.5 MPa are discarded.

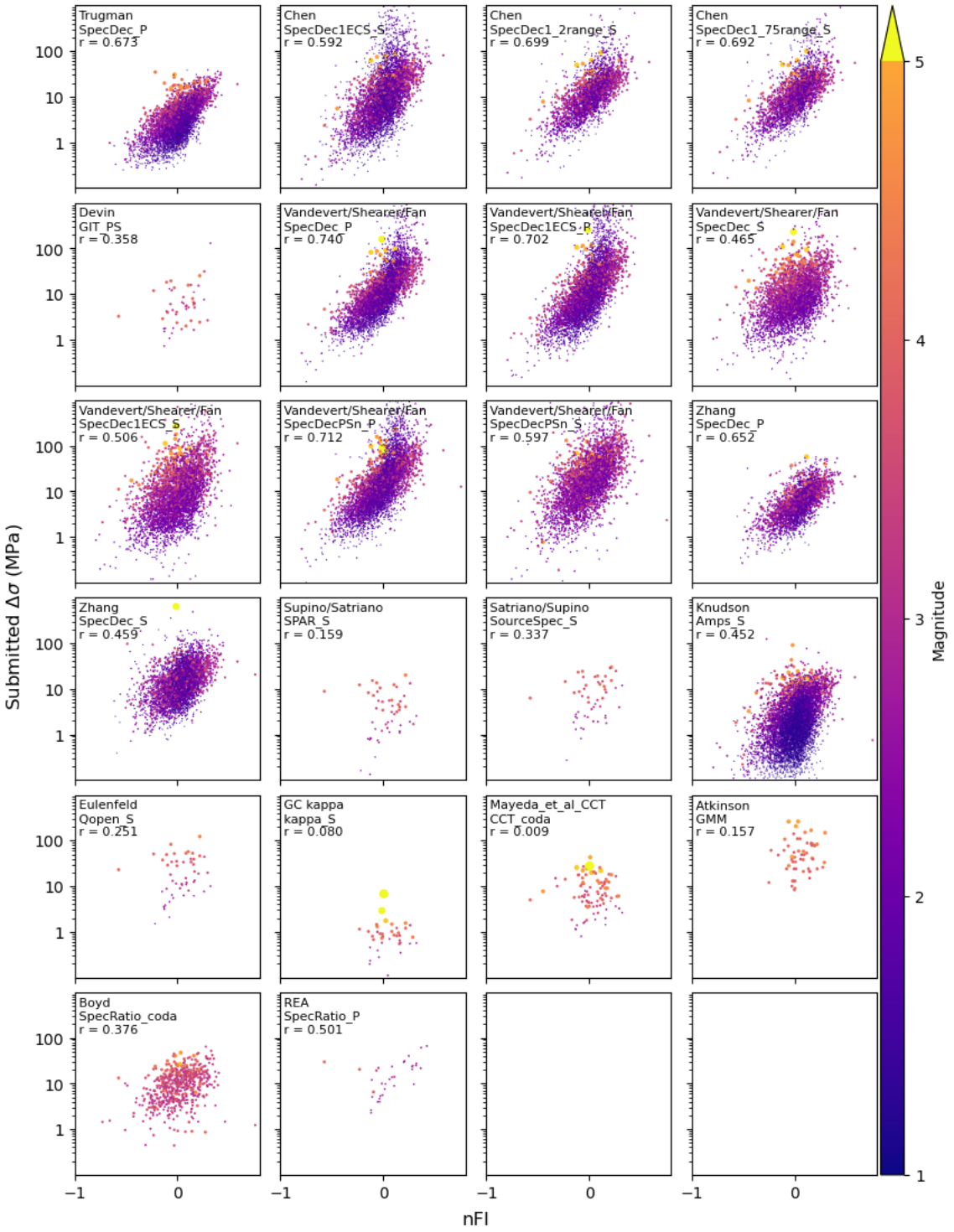


Figure 3.S3. Correlation between the computed P-wave nFI values and various datasets included in *Abercrombie et al.* (2025a). We do not show comparisons here that have fewer than 30 events in common with our dataset. Author names and methods correspond to those in the study. *Abercrombie et al.* (2025a) for more details.

Chapter 4

Distinguishing Spatial Variations in California Earthquake Dynamics Using a High- to Low-Frequency Spectral Ratio

4.1 Introduction

Strong ground motions generated during earthquakes cause damage to property and infrastructure, so characterizing their origin is important in assessing seismic hazard. Earthquake displacement spectra reflect aspects of rupture mechanics: the low-frequency level scales with seismic moment, a principal measure of earthquake size, while high-frequency amplitudes are sensitive to rupture complexity, source duration, rupture velocity, and other factors. On average, larger earthquakes produce stronger ground motion across all frequencies. However, earthquakes of similar moment regularly produce substantially different amounts of high-frequency radiation (e.g., *Aki*, 1967). Understanding the origin and spatial distribution of this variability has direct implications for ground motion prediction and seismic hazard assessment.

Stress drop, the average amount of shear stress released across a fault during an earthquake, is one parameter that quantifies the expected amount of high-frequency energy, albeit indirectly. Stress drop is related to both earthquake moment and the fault rupture

dimension (*Kanamori and Anderson*, 1975), so it is relatively straightforward to compute for large earthquakes with exposed surface offsets or geodetic constraints on rupture area. For smaller earthquakes, spectral stress drop is computed by fitting a theoretical source model to observed spectra (*Brune*, 1970; *Madariaga*, 1976), but is subject to large uncertainties and modeling bias (e.g., *Abercrombie et al.*, 2025a; *Abercrombie*, 2021). Even when source spectra are estimated from many records, they are frequently complex and deviate from smooth theoretical models. In addition, uncertainties in path corrections and model parameter tradeoffs hamper reliable determination of absolute stress drop (e.g., *Shearer et al.*, 2019, 2024). Recent results from the Ridgecrest Stress Drop Validation Exercise (e.g., *Baltay et al.*, 2024) have shown large scatter in absolute stress drop estimates, but much better agreement in relative stress drops between events (*Abercrombie et al.*, 2025a). This implies that while the absolute level of stress drop is often highly uncertain, it does capture some of the variability in rupture behavior.

Despite decades of study on earthquake source mechanics, exactly what controls high-frequency variability remains unclear. Part of the difficulty lies in the large uncertainties in stress drop estimates, which are sensitive to modeling choices and difficult to compare across studies. Parameter choices that produce reasonable results in one dataset or region might produce unrealistic ones in another. Moreover, most stress drop studies have been regional in scope (e.g., *Shearer et al.*, 2006; *Hauksson*, 2015; *Shearer et al.*, 2022; *Trugman and Shearer*, 2018), and to our knowledge no statewide characterization of relative high-frequency variability has been published for California.

Vandevert et al. (2026) introduced the normalized frequency index (nFI), an empirical quantity that characterizes the relative high-frequency content of observed earthquake spectra without relying on a spectral model. Rather than estimating corner frequency and stress drop, nFI measures the spectral ratio between two fixed frequency bands, corrected for path, station, and magnitude effects, to yield a direct comparison of high-frequency enrichment between events. Applied to the 2019 Ridgecrest aftershock

sequence, nFI revealed coherent spatial patterns that strongly correlated with stress drop variations reported by multiple other studies (*Trugman*, 2020; *Vandevert et al.*, 2024; *Abercrombie et al.*, 2025a). nFI is similar in spirit to empirical high-frequency parameters used in ground-motion studies, such as the spectral decay parameter κ (*Anderson and Hough*, 1984), but is explicitly referenced to nearby calibration events to isolate source-controlled variability.

In this study, we extend the nFI method to seismicity across California over a 30-year period (1995–2024), producing the first statewide characterization of relative high-frequency source variability. We leverage California's dense seismic network coverage and diverse tectonic settings to investigate which physical factors correlate with the spatial distribution of relative high-frequency energy. Regardless of their origin or the method used, resolving these spatial differences has the potential to improve ground motion models.

4.2 Data

We analyze seismicity spanning 1995–2024 recorded by the Northern and Southern California Seismic Networks (Fig. 4.1), archived at the NCEDC (*NCEDC*, 2014) and SCEDC (*SCEDC*, 2013), respectively. Because these catalogs overlap spatially in certain regions, some events appear in both catalogs. We draw a line separating California at a natural break in NCEDC-dominated and SCEDC-dominated regions, retaining only NCEDC earthquakes in northern California, and SCEDC earthquakes in southern California. We retain events with magnitudes $M \geq 1$, yielding $776,860$ events: $401,304$ from the NCEDC and $375,556$ from the SCEDC. We also obtain station metadata from both services. Station metadata is mostly consistent, but we use the NCEDC values when they differ slightly.

Where available, we adopt relocated event hypocenters so that smaller-scale patterns may be resolved. For southern California earthquakes, we use the relocated catalog of

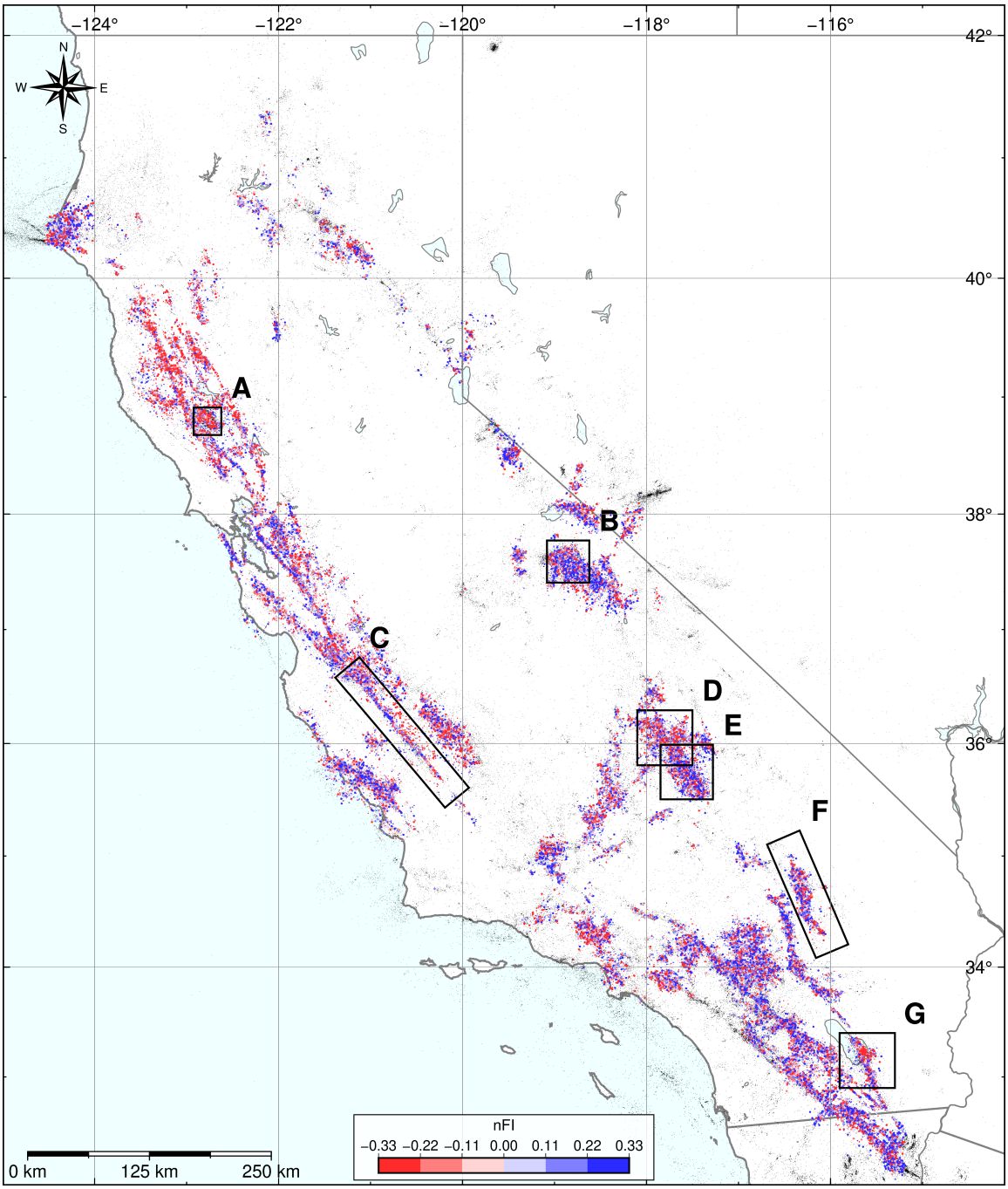


Figure 4.1. Map of the California seismicity analyzed in this study, comprising 776,860 M $\geq$ 1 events from 1995 to 2024. Events that have a computed nFI (N=491,304) are plotted as dots and colored according to their nFI, while those without an nFI are shown as black dots. The outlined subregions are shown in greater detail in later figures: A: The Geysers; B: Long Valley Caldera; C: Central San Andreas Fault; D: Coso Geothermal Field; E: Ridgecrest Sequence; F: Hector Mine Sequence; and G: Salton Trough.

Hauksson et al. (2012), originally based on waveform cross-correlation, with recent updates using GrowClust (*Trugman and Shearer*, 2017b). For northern California, we use the waveform cross-correlation and double-difference relocated catalog of *Waldhauser and Schaff* (2008), which covers events through 2021. Events not appearing in either relocated catalog retain their original location and origin time. In total, about 90% of events have relocated hypocenters. See the Data Availability Statement section for more information.

Event-based waveforms are downloaded from NCEDC and SCEDC cloud services (see the Data Availability Statement section). We retain velocity and acceleration seismograms from broadband and short-period channels with sampling rates of at least 80 Hz to ensure adequate bandwidth at the highest frequencies, and require epicentral distances to be less than 100 km. Approximately 96% of NCEDC catalog events and 97% of SCEDC catalog events have available records that satisfy these requirements. We uniformly resample all waveforms to 100 Hz.

We compute adaptive multitapered spectra (*Prieto et al.*, 2009) of about 12 million P-wave records, using 5 tapers and a time-bandwidth product of 3.5. P-wave arrival times are determined from catalog picks. Signal windows begin 0.15 seconds before the phase arrival. Window length scales with magnitude to accommodate the longer source durations of larger earthquakes: 1.5 seconds for $M \leq 3.5$, increasing linearly to 4.5 seconds for $M \geq 4.5$. Corresponding noise windows are of equal length and directly precede their signal window. Resulting spectra are resampled to $\Delta f = 2/3$ Hz, matching the frequency resolution of a 1.5 second, 100 Hz time series. About 92% of records have a cataloged instrument response; we correct for this instrument response and discard records without an available response. Spectra with signal-to-noise ratios (SNR) of < 3 in the 2.67–6 Hz band are discarded, but we do not apply a minimum high-frequency SNR to avoid selection bias toward events with relatively more high frequencies (*Shearer and Abercrombie*, 2021). In total, about 9.4 million (78%) spectra that pass these criteria remain.

4.2.1 Station Gain Changes

This dataset spans a wide temporal range, and changes in station instrumentation are inevitable over three decades. The previous study that introduced nFI (*Vandevert et al.*, 2026) spanned only two weeks of data, so changes in instrumentation, whether by defect or instrument replacement, were less likely than over the 30-year span of this study. To identify undocumented changes in station response, we follow a procedure similar to that of *Shearer et al.* (2022): for each station we compute the average spectral amplitude of the noise window between 3.33 and 4.67 Hz and compare these values over time. We extend this approach by automatically detecting significant changes in average noise levels using a binary segmentation change-point detection algorithm (e.g., *Fryzlewicz*, 2014). Nearby major events generally cause an increase in average noise levels because of frequent aftershocks. These can trigger erroneous apparent changes in station response (false positives), so we discard change points within a short time interval of a nearby major event. To avoid correcting for real differences in noise levels, we require a minimum difference of 1% between subsequent segment averages of log noise level. This corresponds to requiring the noise levels in any two consecutive periods to change by 20–40% to be flagged as an undocumented change in instrument gain.

Once change points are screened, we apply a correction to the signal and noise spectra of all records within each segment. The downstream methods are not affected by vertical shifts applied uniformly to all records from a single station, so we compute each segment's correction to shift the segment to the mean noise of all records from that station.

4.3 Methods

The method to compute the normalized frequency index (nFI) was introduced in *Vandevert et al.* (2026), where it was applied to the 2019 M 7.1 Ridgecrest aftershock

sequence in California. Here we review the fundamental steps of the method, referring to the original study for more details.

Our approach is based on computing the spectral ratio of a high-frequency band to a low-frequency band. This is effectively equivalent to the frequency index (FI) used in volcano seismology (e.g., *Buurman et al.*, 2010), except that FI computes this ratio using mean band amplitude rather than median. We distinguish $\log \beta$ from FI because it serves as an intermediate quantity rather than the final metric. For all spectra, we compute:

$$\log \beta = \log_{10}(\mathrm{A_{HF}}) - \log_{10}(\mathrm{A_{LF}}), \tag{4.1}$$

where $\mathrm{A_{HF}}$ and $\mathrm{A_{LF}}$ represent the median spectral amplitudes in predefined high- and low-frequency windows, illustrated in Figure 4.2. Here, $\log \beta$ represents the "richness" of high frequencies relative to low frequencies for a single observed spectrum. Ideally, $\mathrm{A_{LF}}$ should sample the flat portion of a displacement spectrum below the corner frequency, while $\mathrm{A_{HF}}$ should sample the high-frequency decay above it. When this condition is not met, between-event variability in high-frequency content becomes difficult to resolve. Moreover, adjusting the high or low frequency bands within the same dataset (e.g., using a lower low-frequency band for larger events) affects $\log \beta$ and ultimately nFI nonlinearly. We choose 1.33–5.33 Hz for the low band and 15.33–20.0 Hz for the high band in this dataset, and explore the effect of frequency band choice on effective magnitude range in the Discussion section. The $\log \beta$ values for the entire dataset are shown in Figure 4.3, panels (a) and (d).

The $\log \beta$ derived from observed spectra contain path and station effects that must be corrected. We model these effects additively in logarithmic space, following spectral decomposition approaches (e.g., *Shearer et al.*, 2006):

$$\log \beta_{ij} = \Delta \log \beta_i + S_j + P_{q(i,j)}. \tag{4.2}$$

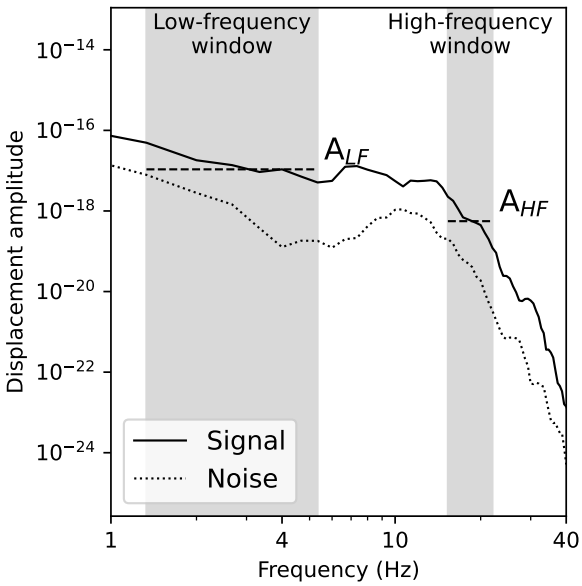


Figure 4.2. Example spectrum showing $\log \beta$ computation. A_{LF} and A_{HF} are the median amplitudes of bands 1.33–5.33 Hz and 15.33–20.0 Hz, respectively.

Here, $\log \beta_{ij}$ is the $\log \beta$ of event i measured at station j; S_j is the station term; $P_{q(i,j)}$ is the path term along ray path q; and $\Delta \log \beta_i$ is the source term representing event-specific variability that we seek to isolate.

To empirically correct for path and station effects, we identify small "calibration" earthquakes near each target event that are also recorded by at least some of the same stations. We make three assumptions: (1) records at the same station have an equal station term S_j; (2) ray paths from a target and calibration event to the same station produce equivalent path effects, such that $P_{q(i,j)} \approx P_{q(k,j)}$; and (3) the calibration magnitude range is narrow enough to minimize moment-related variability among calibration events. Under these assumptions, for a calibration event k near target event i, the difference $\log \beta_{ij} - \log \beta_{kj}$ cancels the station and path terms. For each station, we take the median of this difference over all calibration events; we then take the median across stations to obtain $\Delta \log \beta_i$:

$$\Delta \log \beta_i = \text{median}_j(\text{median}_k(\log \beta_{ij} - \log \beta_{kj})) \tag{4.3}$$

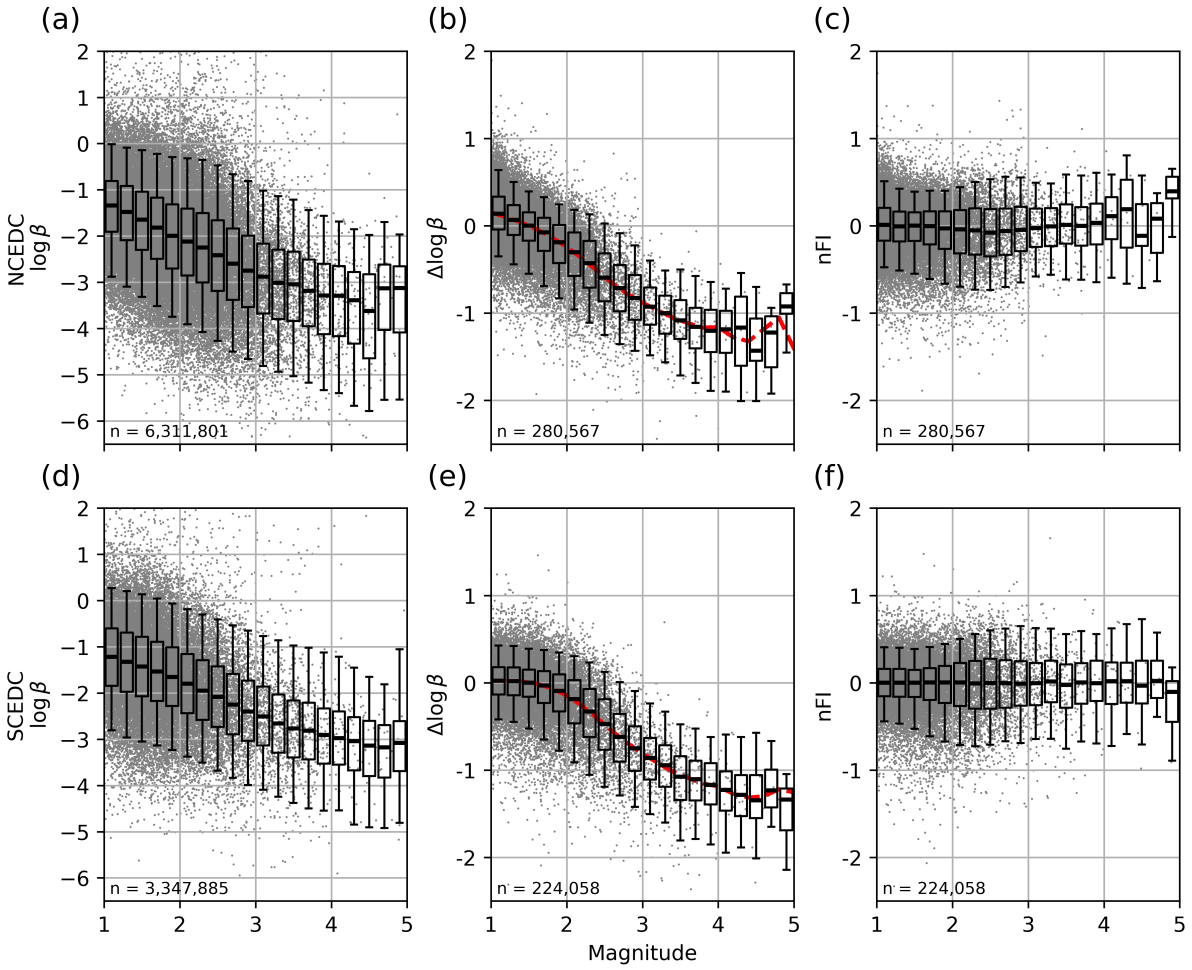


Figure 4.3. Different processing stages to obtain nFI from individual $\log \beta$ measurements, separated for NCEDC events (top row) and SCEDC events (bottom row). Left column: $\log \beta$ results for each spectrum passing the signal-to-noise criteria. Middle column: $\Delta \log \beta$ for each event after applying path and station corrections, and the magnitude correction (red dashed line) applied to get nFI. Right column: nFI after applying magnitude corrections. Box extent denotes 25th and 75th percentiles of data in bins of width M 0.2, and whiskers represent 5th and 95th percentiles. Note the wider scale in the $\log \beta$ panels ((a) and (d)).

We select calibration events with magnitudes between M 1.4 and M 1.6, located within 10 km horizontally and 2 km vertically of the target event. The tighter vertical constraint reflects the greater sensitivity of path effects to depth variations (*Abercrombie et al.*, 2021). To ensure robust estimation of $\Delta \log \beta$, we require a minimum of 10 calibration events per station. Events tagged as quarry blasts or explosions are excluded as calibration events,

but not as target events. The source code (see the Data Availability Statement section) allows calibration events to be restricted to a time window around each target event. Results computed using a ±180 day window are included in the Supporting Information for reference.

The resulting $\Delta \log \beta$ values represent relative source variability. Naturally, the relative amount of high-frequency energy is magnitude-dependent, as larger earthquakes have longer source durations and proportionally less high-frequency energy. We remove this magnitude dependence using a single, global correction; however, we perform this correction separately for the NCEDC and SCEDC results to reduce the effect that differences in catalog magnitude might have on our results (*Pinilla-Ramos et al.*, 2026).

We compute the median $\Delta \log \beta$ in magnitude bins of width M 0.2 and smooth the result with a Savitzky-Golay filter of order 3 (see Fig. 4.3 panels b and e). We interpolate this smoothed curve to each event's magnitude and subtract it from the corresponding $\Delta \log \beta$ to obtain nFI. This allows us to analyze source variability relative to the average earthquake of the same magnitude. By construction, nFI has roughly zero median at any magnitude: positive values indicate high-frequency enrichment, and negative values indicate depletion.

4.4 Results

Out of 776,860 cataloged earthquakes, we obtain nFI estimates for 491,304 events (58%), of which about 17% are calibration-sized events. The majority of M $\geq$ 2 events without an nFI estimate are located offshore, outside California borders, or deeper than 20 km, where station coverage is poorer and calibration-sized earthquakes are less well recorded. The nFI distribution is approximately Gaussian with a slight negative skew; median nFI is about zero to within 10^{-3} (as expected by construction), and the standard deviation is 0.310. The distribution does not differ significantly between the northern

and southern California catalogs. Since about 95% of cataloged events are shallower than 20 km in depth, we refer to events deeper than 20 km as "deep" events.

Non-tectonic events show systematically lower nFI than tectonic earthquakes (Fig. 4.4). Event type classifications in the NCEDC and SCEDC catalogs distinguish tectonic earthquakes from long-period volcanic events, quarry blasts, and chemical explosions. Long-period volcanic events, located in the Long Valley Caldera, Geysers, and Lassen Peak regions, have a median nFI of -0.29 (N=79). Quarry blasts and chemical explosions have a median nFI of -0.29 (N=1,445) and are distributed widely across California. These findings are in agreement with *Allmann et al.* (2008), who found that quarry blast spectra have a steeper falloff rate than earthquakes in southern California.

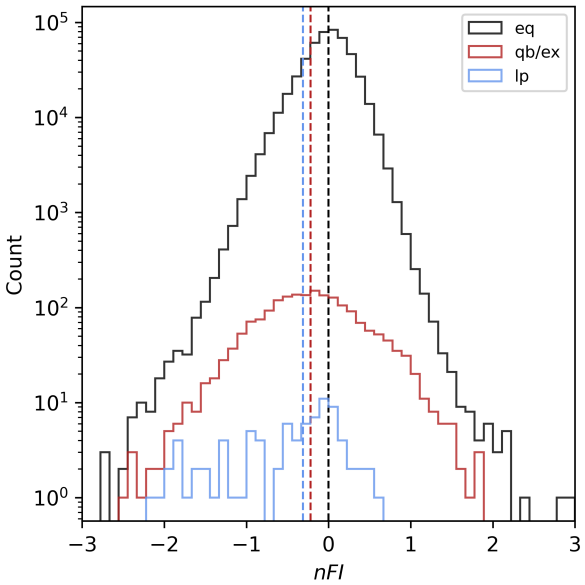


Figure 4.4. Histograms of nFI for different catalog-identified event types: eq = tectonic earthquake, qb = quarry blast, ex = chemical explosion, and lp = long-period volcanic event.

Unless otherwise stated, all further results presented are for natural earthquakes (including long-period volcanic events) of at least M 2 because spatial variation is less apparent in the smaller events as they approach the size of the M $\sim$ 1.5 calibration events. By normalizing the results relative to calibration events within 10 km epicentral

distance, our method naturally suppresses nFI variations at 10-km and longer scales for near-calibration event magnitudes, but has the advantage of ensuring that spatial nFI variations seen in larger events must indicate real differences in source properties rather than uncorrected attenuation or other path effects.

4.4.1 Stress drop comparison

The normalized frequency index quantifies an earthquake's relative high-frequency content. Stress drop does this indirectly, so the two should correlate as they did in *Vandevert et al.* (2026) for the Ridgecrest aftershocks. We compare nFI to San Francisco Bay Area stress drop estimates from *Trugman and Shearer* (2018) and southern California estimates from *Shearer et al.* (2022) (Fig. 4.5). The nFI and $\log_{10} \Delta\sigma$ estimates exhibit a positive correlation, but with considerable scatter. The scatter is unsurprising given differences in how the two parameters are computed, and reinforces that nFI is not intended to be a proxy for stress drop (*Vandevert et al.*, 2026).

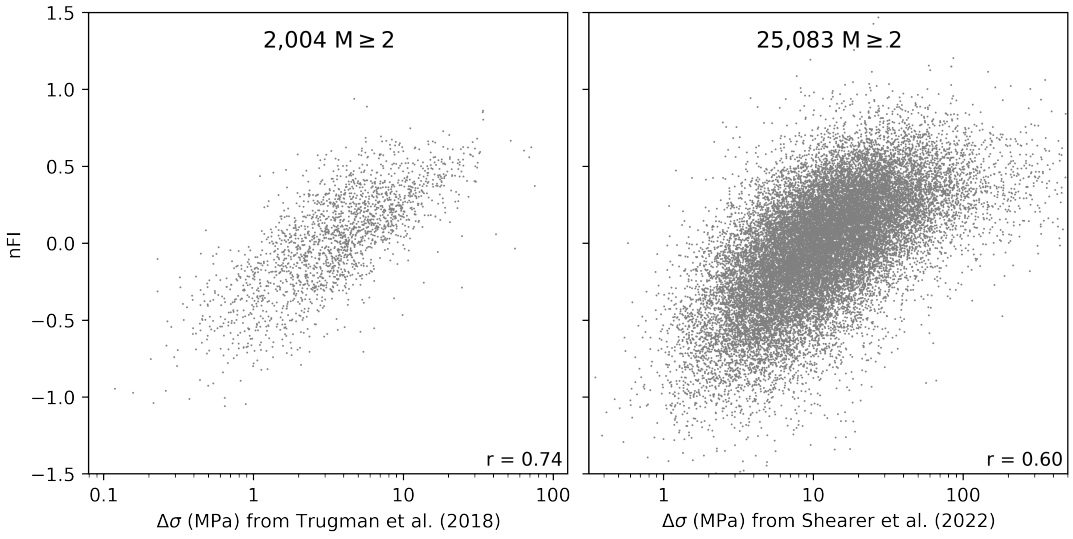


Figure 4.5. nFI plotted against stress drop from: (a) *Trugman and Shearer* (2018) for events in the San Francisco Bay Area; and (b) *Shearer et al.* (2022) for events in Southern California. The log width of each plot is the same, but note the different x-axis range due to varying average $\Delta\sigma$ in each study.

4.4.2 Hypocentral depth

In both the NCEDC and SCEDC catalogs, nFI rises sharply with depth in the upper few kilometers, followed by a gradual increase in nFI with depth down to about 10–12 km (Fig. 4.6). Median values below 14 km are less certain because only about 4% of events fall in this range. The shallow increase in the NCEDC catalog reflects a concentration of very low nFI events in the Geysers region, a shallow geothermal field. Excluding Geysers events dampens the sharp increase but preserves the gradual increase across the remaining depth range. Increasing normal stress with depth has been proposed as a mechanism for the depth dependence of stress drop (*Marone*, 1998), but this is not always observed. Our results are in agreement with *Abercrombie et al.* (2021), who reported increasing spectral high-frequency content with depth for all magnitudes.

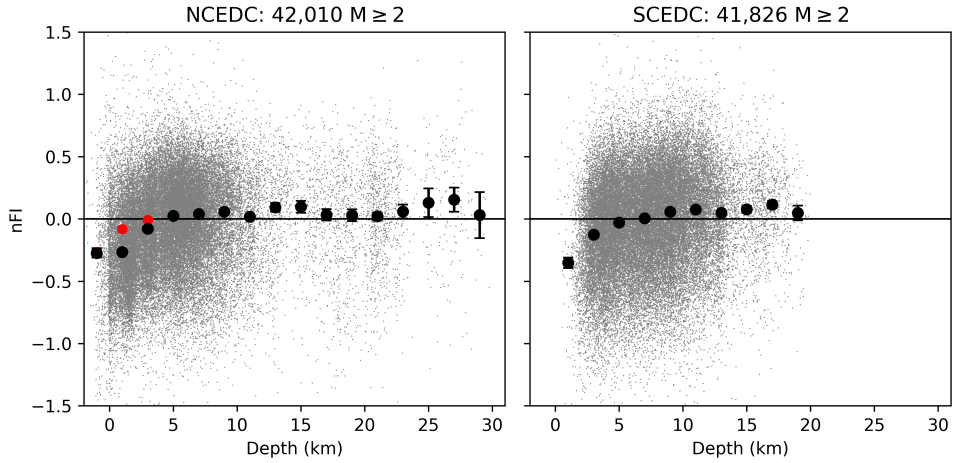


Figure 4.6. nFI versus earthquake depth for earthquakes M $\geq$ 2. Circles represent median nFI in bins of 2 km. Red circles are computed identically but without events in the Geysers region (see Fig. 4.1 subregion A). Bars denote 2× the standard error.

4.4.3 Focal mechanism

We compare nFI to focal mechanisms from *Cheng et al.* (2025) for 1995–2021, restricting the comparison to M $\geq$ 2 events with focal mechanism uncertainty below 20°. Using the method from *Shearer et al.* (2006), we parameterize faulting style on a

continuous scale from −1 (normal faulting) to +1 (reverse faulting), with 0 representing strike-slip faulting. This dataset is dominated by strike-slip events because of California's transform boundary, with about 3× as many events as either normal or reverse. In both the NCEDC and SCEDC catalogs, median nFI is higher for reverse-faulting events than for strike-slip events (Fig. 4.7). In contrast, nFI for normal-faulting earthquakes relative to strike-slip earthquakes is lower in the NCEDC catalog but higher in the SCEDC catalog.

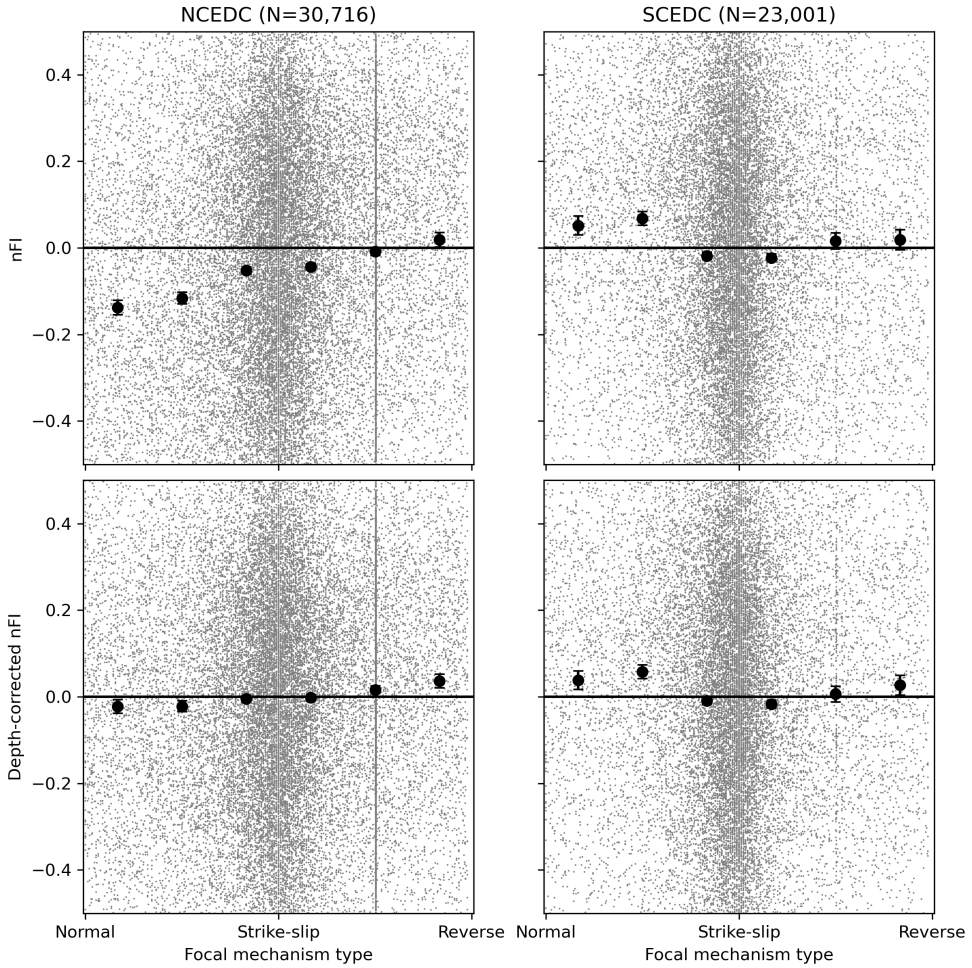


Figure 4.7. nFI (top row) and a depth-corrected nFI (bottom row) plotted against focal mechanisms from *Cheng et al.* (2025) for earthquakes M $\geq$ 2. Depth-corrected nFI is computed by subtracting the median nFI at the depth of each earthquake (see Fig. 4.6 for median nFI at depth). Bars denote 2× the standard error. Faulting style is parameterized on a continuous scale from −1 to +1 using the method from *Shearer et al.* (2006).

The focal mechanism dependence appears to be affected by the specific depths

at which the faulting types occur: normal-fault events are systematically deeper in the SCEDC catalog (median depth = 7.5 km) compared to the NCEDC catalog (median depth = 3.1 km). To quantify this disparity, we compute a depth-corrected nFI by subtracting from each earthquake's nFI the median nFI of events at that depth (Fig. 4.7). This is done separately for the two catalogs. Compared to strike-slip events, SCEDC normal events still have a higher depth-corrected nFI. However, the difference between faulting styles among NCEDC events is greatly reduced, though a small difference remains. Depth alone does not account for all the difference, but dampens the effect. For reverse-faulting events, we again find that depth alone does not account for all the difference, and reverse events have higher nFI than strike-slip.

4.4.4 Heat flow

The surface heat flow compilation of *Lucazeau* (2019) provides heat flow on a global $0.5° \times 0.5°$ grid. The highest values in California occur at the Geysers, the Salton Trough, the Coso Geothermal Field, the Long Valley Caldera, offshore San Diego, and near Lassen Peak; the lowest values occur in the Central Valley and the Los Angeles Basin.

We interpolate the heat flow grid to a finer ∼1 km grid using a radial basis interpolator and assign the interpolated heat flow value at each event's epicenter. In both catalogs, nFI is approximately constant at low to moderate heat flows and drops sharply at high heat flow (Fig. 4.8). The drop-off threshold is near 100 mW/m^2 in the NCEDC and 140 mW/m^2 in the SCEDC. However, the NCEDC events have a slightly elevated nFI at moderate heat flows (about 80–100 mW/m^2). These results are in agreement with stress drop observations in *Hauksson* (2015), who attributed low stress drops at high heat flow to a shortened fault healing time. In any case, the observations suggest that earthquakes that occur in regions with high surficial heat flow are relatively depleted, on average, of high-frequency content.

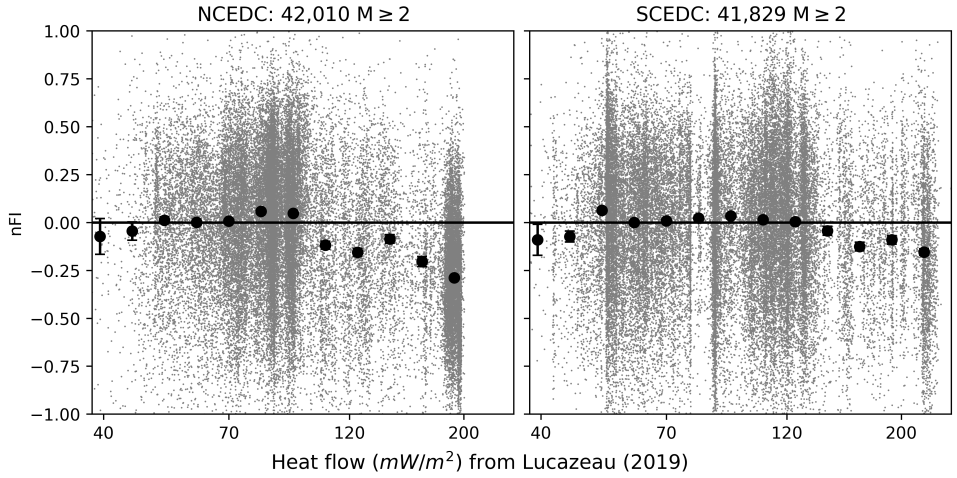


Figure 4.8. nFI plotted against surface heat flow at the location of each event. Heat flow data are from *Lucazeau* (2019). Bars denote 2× the standard error.

4.4.5 Spatial variation

While there is no significant difference in average nFI between the NCEDC and SCEDC catalogs, we do identify many spatial variations. In northern California, the northwest-southeast trending faults north of San Francisco produce low-nFI earthquakes on average (Fig. 4.1). This region includes the Geysers, a seismically and geothermally active region with about 87,000 M ≥ 1 earthquakes and a very low average nFI of about -0.3. Near San Francisco, the San Andreas and Hayward faults appear to have higher-than-average nFI. East of the Sierra Nevada, three regions that have low- and high-nFI clusters in close proximity are Mammoth Lakes, near Walker, and the Coso Geothermal Field. In southern California, larger-scale spatial patterns include a low-average nFI near the Salton Sea and high-nFI earthquakes along the San Jacinto fault zone.

4.5 Discussion

The large-scale spatial patterns, including the low-nFI region north of San Francisco and the high-nFI region southeast of Los Angeles, appear to be robust features of California seismicity. Earthquakes in the low-nFI region are shallower than those in the high-nFI

region, and while we have observed increasing nFI with depth, the nFI anomalies in both regions exceed what the depth trend alone predicts. Because our analysis combines events from two independent data centers with their own magnitude and origin conventions, a systematic difference in $\Delta \log \beta$ versus magnitude between catalogs could, in principle, result in an artifact resembling spatial variation. We tested this possibility by computing nFI two ways: with a single statewide magnitude correction applied to all events, and with separate corrections applied to each catalog. The resulting spatial patterns are visually indistinguishable at this scale and the low- and high-nFI regions persist in both cases. We nonetheless adopt the catalog-specific corrections in our preferred results to accommodate any residual differences between catalogs that the joint correction might not account for.

We observe a gradual increase in relative high-frequency radiation with depth across the dataset down to about 10 km after removing the shallow Geysers seismicity (discussed above). In the upper few kilometers, this trend could in principle be biased by how calibration events are selected. Sharp velocity gradients in the upper few kilometers, combined with the increasing scarcity of earthquakes closer to the surface (Fig. 4.6), mean that calibration events for a shallow target are drawn disproportionately from deeper, faster material. The raw $\log \beta$ of those calibration events would be systematically higher than that of events at the target's depth, so the calibration step would over-correct and bias the target nFI downward. We tested the plausibility of this by recomputing nFI with a tighter vertical calibration window of ± 1 km instead of ± 2 km. Doing this, the sharp increase in shallow events is only slightly dampened and the remaining depth profile is largely unchanged, so this effect is likely not controlling the sharp increase.

Stronger normal stress at depth has been proposed as a mechanism for increasing stress drop with depth (*Marone*, 1998). Some studies have observed increasing stress drop with depth (*Boyd et al.*, 2017; *Hardebeck and Aron*, 2009; *Trugman*, 2020), while others have found no increase with depth (e.g., *Shearer et al.*, 2006; *Allmann and Shearer*, 2009). *Abercrombie et al.* (2021) found that the apparent increase in stress drop with depth is

largely removed when a depth-dependent empirical correction is made, observing that: (1) earthquakes of all magnitudes are more enriched in high-frequency energy with increasing depth; (2) in all regions, earthquakes of a similar size increase in high-frequency energy with depth; and (3) this increase is more pronounced in regions with a steeper change in the local velocity structure. Our observations are consistent with (1) and (2). We do observe different amounts of depth dependence in different regions, however we do not quantitatively compare with velocity structures.

Our results show a great deal of coherent variability in median nFI over a wide range of spatial scales. As discussed above, our empirical calibration method using nearby small-magnitude calibration events ensures that these variations reflect differences in source spectral content; that is, they are not caused by near-source attenuation structure. Although some of the nFI variations correlate with depth, focal mechanism, and heat flow, these factors account for only a fraction of the observed signal.

In the following subsections, we discuss results for selected regions of interest in more detail. However, there are many intriguing signals in other areas that we encourage other researchers to explore using our archived interactive maps (See Data Availability Statement).

4.5.1 nFI in geothermal regions

Our results show that median nFI has some dependence on heat flow (Fig. 4.8), especially in regions of high heat flow, where nFI is very low. Wells used for geothermal energy are more likely to be located in areas of higher heat flow. Three regions that contain many geothermal wells, the Geysers, the Coso Geothermal Field, and the Salton Trough, also tend to have low nFI within a short distance of the wells (Fig. 4.9). Statewide, the median nFI of M ≥ 2 earthquakes within 0.01° of a geothermal well is very low, at -0.19.

The Long Valley Caldera is a volcanic caldera formed by a large eruption about 750 ka and has experienced activity since (*Bailey et al.*, 1976; *Biondi et al.*, 2023). As a

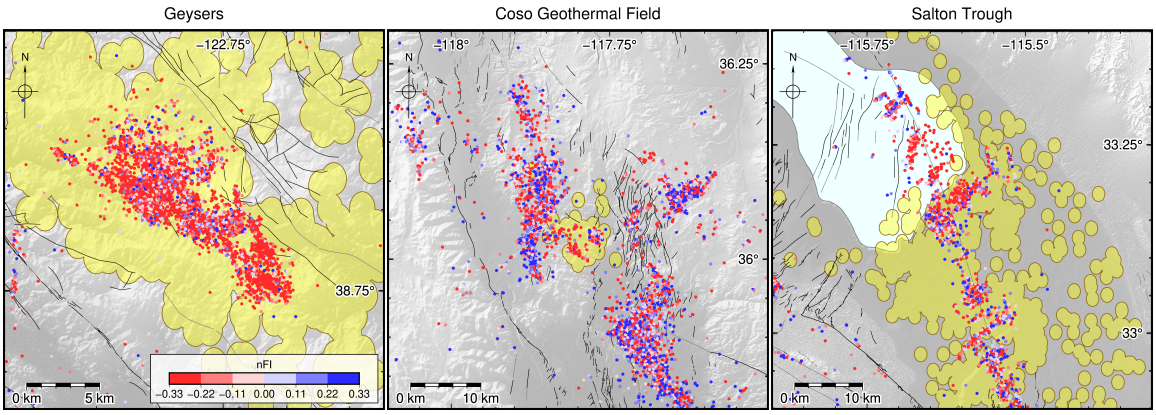


Figure 4.9. Zoomed map views of M $\geq$ 2 seismicity in three California geothermal regions, colored by nFI: (a) the Geysers (N=7,578), (b) the Coso Geothermal Field (N=5,621), and (c) the Salton Sea Trough (N=3,406). Yellow shaded areas mark regions within 1 km of geothermal wells. Well-constrained fault traces are plotted as dark gray lines, all others are light gray. See Figure 4.1 for subregion locations.

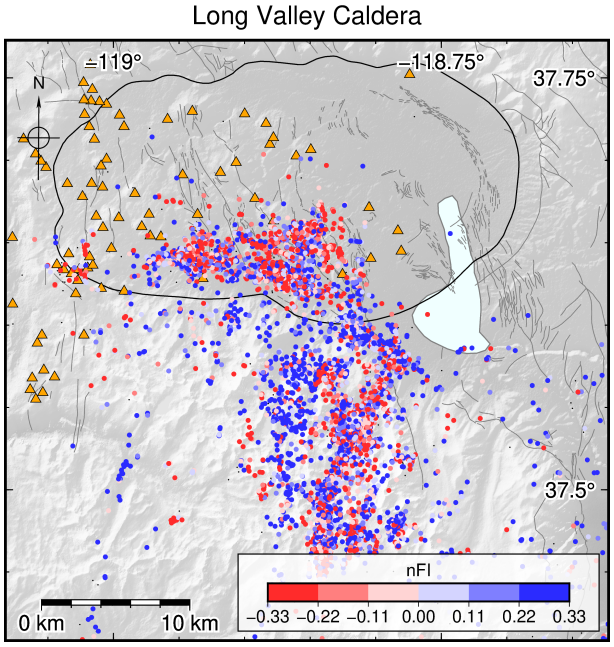


Figure 4.10. Map of seismicity in the Long Valley Caldera region colored by nFI (N=6,283), with mapped volcanic vents shown as orange triangles. Events within the caldera ring fault (black line) and near vents display lower nFI. All other faults are shown as gray lines.

result, there are many shallow and surficial geothermal features in the region including volcanic vents and hot springs (*Bailey*, 1989). We show our nFI results, volcanic vent locations, and caldera ring in Figure 4.10. Active vent locations are mostly inside the

caldera and to the west and southwest. There are also many geothermal wells inside the caldera that are not shown. Earthquakes inside the caldera exhibit lower nFI (median $= -0.01$) than those outside (median $= +0.14$). Extending from the southern rim of the caldera, we also note two parallel north-south trending features: one high-nFI and one low-nFI to its east. These spatial variations may reflect differences in underground structure.

4.5.2 Ridgecrest sequence

The 2019 Ridgecrest sequence began on 4 July when a M 6.4 earthquake ruptured on a northeast-trending strike-slip fault about 15 km WNW of Ridgecrest, California. The M 7.1 mainshock followed ~ 34 hours later on a perpendicular, northwest-trending fault about 17 km NNW of Ridgecrest (*Ross et al.*, 2019). Roughly 13,000 M ≥ 1 aftershocks followed within two weeks, well recorded by California's dense regional network. The sequence has spurred numerous studies, including the Community Stress Drop Validation Study (*Abercrombie et al.*, 2025a). *Vandevert et al.* (2026) introduced nFI using this catalog; here we examine the post-M 6.4 sequence within our statewide context, which contains roughly 3$\times$ as many events over five years.

The Ridgecrest sequence's nFI structure is consistent with prior characterizations of this region. The statewide nFI values correlate with those of *Vandevert et al.* (2026) ($r = 0.67$) with broader spread that reflects the different magnitude calibrations between studies. In map view, nFI reproduces the spatial pattern described in *Vandevert et al.* (2026) (Fig. 4.11): a region of low average nFI near the northwestern end of the aftershock zone (east of point A in Fig. 4.11) and higher nFI in the central region where the two main fault traces intersect; similar patterns have been reported in other studies (e.g., *Trugman*, 2020; *Knudson et al.*, 2025; *Abercrombie et al.*, 2025a). The low-nFI region is adjacent to the Coso geothermal field, so heat flow and geothermal activity may control nFI in this region. In cross section, depth dependence mirrors the statewide trend (Fig. 4.6),

exhibiting a sharp increase in nFI at shallow depths followed by a gradual increase below.

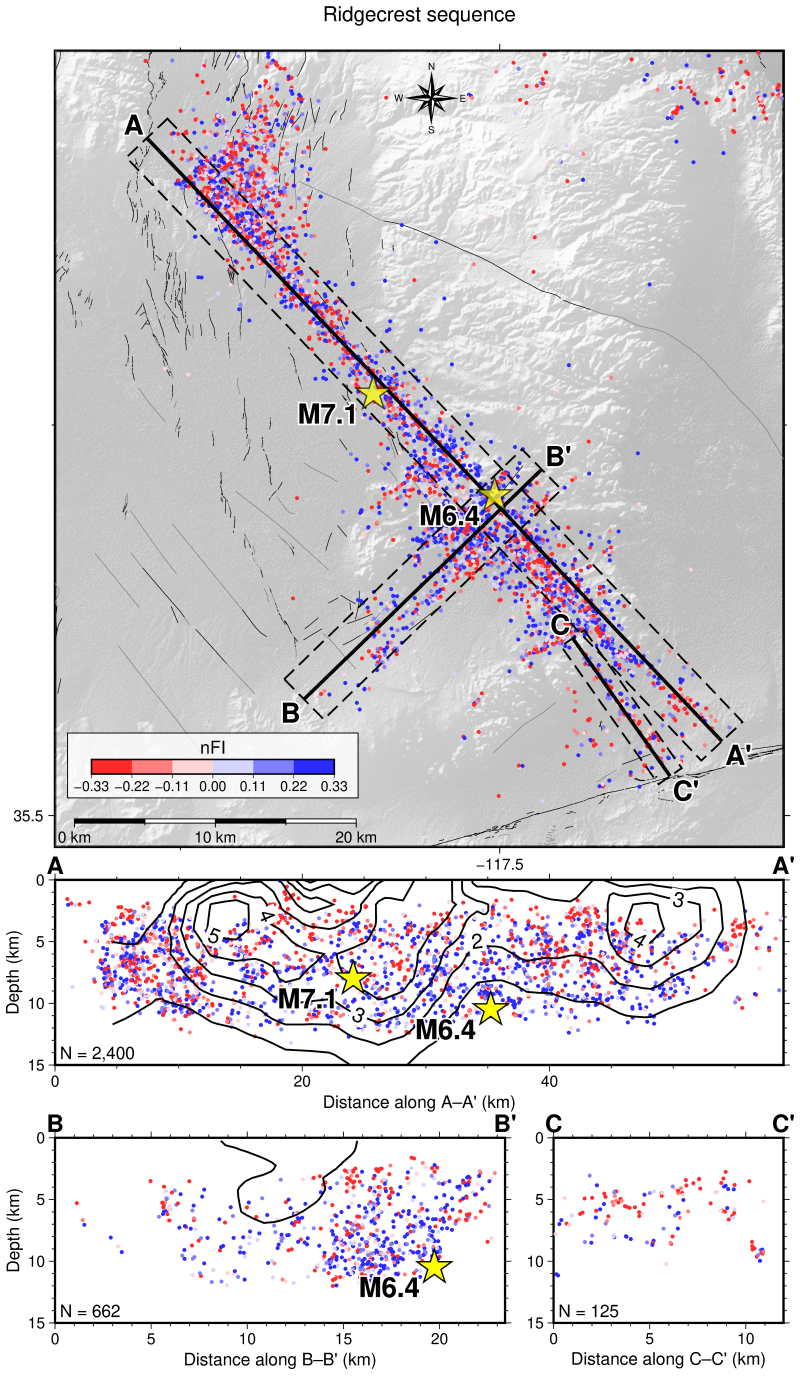


Figure 4.11. Map view (top) and three cross sections of the 2019 Ridgecrest, California, aftershock sequence, with events colored by nFI. Well-constrained fault locations are plotted as dark gray lines, all others are light gray. Only M $\geq$ 2 events after the M 6.4 event on 4 July 2019 are shown. Contours in A and B cross sections are meters of slip from the joint inversion model in *Wang et al.* (2020).

It is uncertain whether mainshock slip distribution controls the source parameters of aftershocks. Patches with higher slip generally have fewer aftershocks (*Das and Henry*, 2003), and lower aftershock stress drops in these patches have been hypothesized, but recent studies remain inconclusive (e.g., *Shearer et al.*, 2006; *Woessner et al.*, 2006; *Ruhl et al.*, 2023; *Folesky et al.*, 2024). The overlain joint seismic-geodetic slip inversion of *Wang et al.* (2020) (Fig. 4.11) shows no apparent correlation with nFI. This is consistent with an analogous stress drop comparison in *Vandevert et al.* (2024). Possible interpretations include: (1) coseismic slip does not strongly affect the high-frequency content of aftershocks, and other fault zone properties are more controlling; (2) nFI at this scale lacks the resolution or certainty to identify such a relationship; (3) inversion models smooth over small-scale heterogeneities so any correlation would be undetectable; (4) some combination of these.

4.5.3 Hector Mine sequence

The M 7.1 Hector Mine mainshock ruptured a northwest-trending strike-slip fault complex about 190 km ENE of Los Angeles, California, on 16 October 1999 (*Hauksson et al.*, 2002). Through 2024, over 21,000 M $\geq$ 1 events have been recorded by SCEDC within the region shown in Figure 4.12, concentrated along the complex branching fault zone. The depth dependence of nFI in this region mirrors the statewide trend (Fig. 4.6): a sharp shallow increase followed by a gradual increase below.

Few studies have computed stress drops for the Hector Mine sequence on a large scale, but some have done so for a small subset. Both *Chen and Shearer* (2013) and *Yoon et al.* (2019) found that foreshocks had lower stress drops than aftershocks, consistent with our observations; M $\geq$ 2 foreshocks within 5 days of the mainshock have a slightly lower median nFI (-0.09, N=7) than aftershocks within 5 days ($+0.11$, N=840). However, the foreshock sample is small, and it is unclear whether this reflects selection bias; networks are less likely to identify small earthquakes with relatively less high-frequency energy

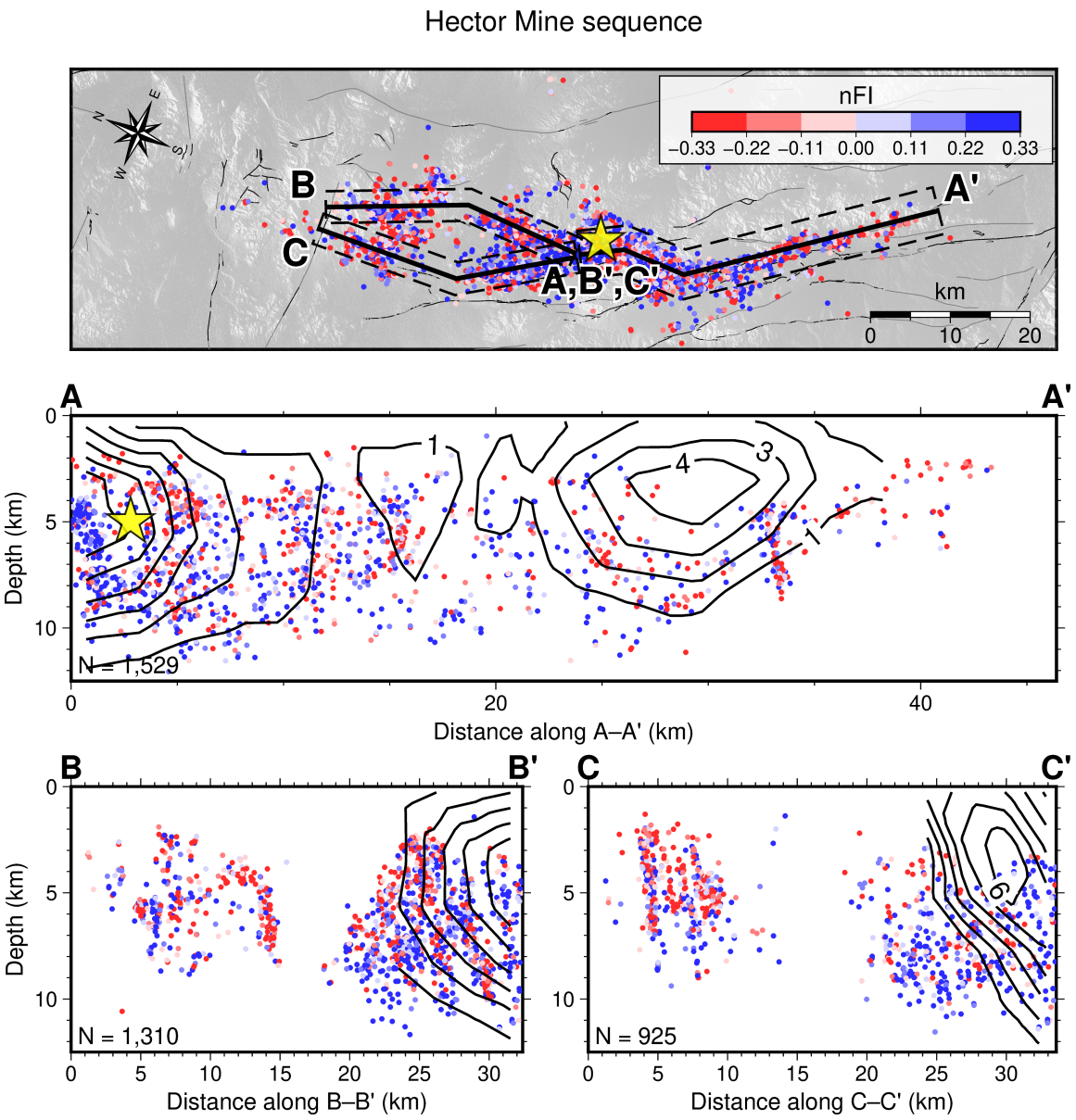


Figure 4.12. Map view (top) and three cross sections of aftershocks of the Hector Mine earthquake on 16 October 1999. Well-constrained fault locations are plotted as dark gray lines, all others are light gray. Only M $\geq$ 2 events after the mainshock are shown. Slip contour lines are projected onto the cross sections using results from *Ji et al.* (2002) but may differ slightly because of the complex fault geometry. The M 7.1 mainshock (yellow star) uses the depth computed in *Hauksson et al.* (2002) (5 ± 4 km) rather than the SCEDC catalog depth (13.7 ± 31.6 km) because of its lower uncertainty.

immediately following a large mainshock because of the increased seismic activity. Within a year of the mainshock, aftershocks return to a negative average nFI in the same region;

it is equally uncertain whether this observed increase in nFI is a network artifact or a real change in high-frequency content.

Spatial variation is clearer than temporal variation, and we identify structure in nFI along the three cross sections. Along A–A', the M 7.1 hypocenter is bounded by a high-nFI region towards A and a low-nFI region towards A'. Multiple vertically-elongated low-nFI clusters are apparent in all three cross sections, including one ∼35 km along A–A' that is capped by high-nFI events. These features are on the scale of a few kilometers, but their cause is unclear. *Hauksson et al.* (2002) identified several low-Vp/Vs anomalies around 5–12 km in depth that might correlate with some of these anomalous clusters, but a direct comparison is difficult.

As with the Ridgecrest sequence, we find no general correlation between mainshock slip and nFI. We compare our nFI to the slip from *Ji et al.* (2002), computed using a joint seismic-geodetic inversion. While the patch of highest slip has events with higher nFI on average, this does not translate into a statistically significant correlation.

4.5.4 Central San Andreas Fault

The central San Andreas Fault is one of the most-studied fault zones in the world. A 60 km long creeping section (Fig. 4.13, gold region) is flanked by two zones that transition from creeping to locked behavior. The 1989 Loma Prieta earthquake ruptured a locked segment about 100 km northwest of A in Figure 4.13, and the 2004 M 6.0 Parkfield earthquake ruptured parts of the southern transition and locked zones (*Liu et al.*, 2022).

As in the Ridgecrest and Hector Mine sequences, we identify clear spatial variation in nFI with depth. Notably, earthquakes along the central San Andreas Fault (those in A–A' in Figure 4.13) exhibit a higher median nFI of +0.11. nFI is highest in the northern transition zone and creeping section (+0.14 and +0.13, respectively) but lower in the southern transition zone (+0.07). The locked section in Figure 4.13 also has a high nFI (+0.18), but only contains 9 earthquakes. Further, while much of the creeping zone

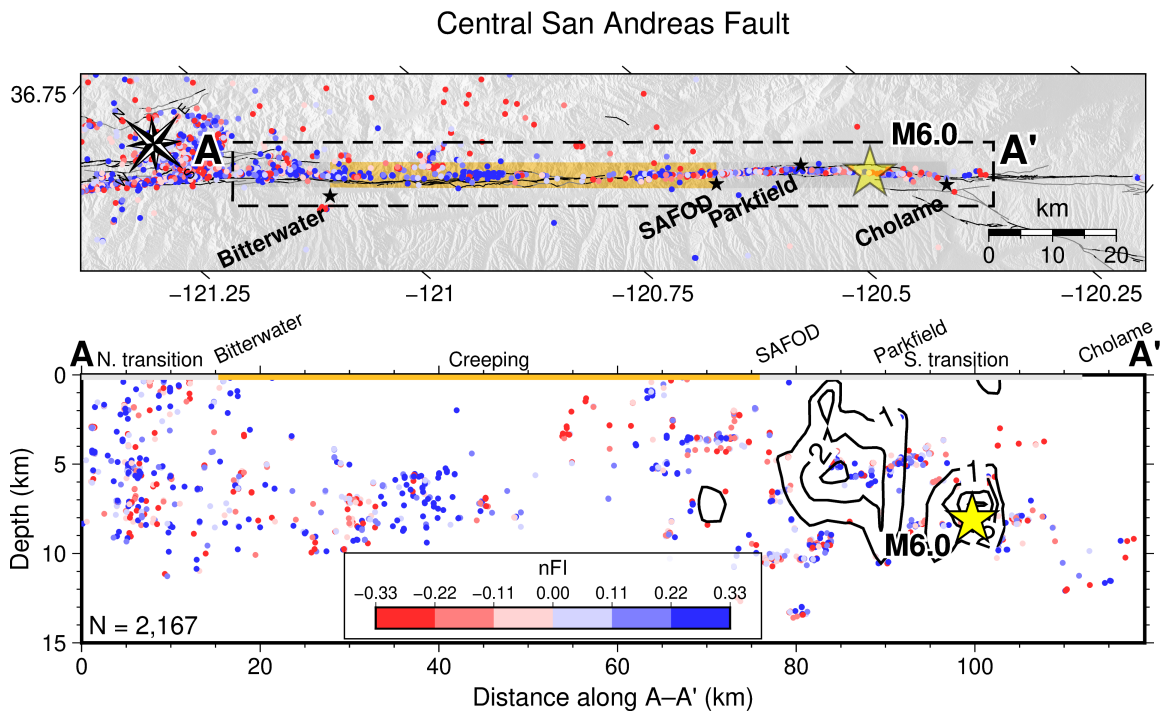


Figure 4.13. Map view (top) and fault-parallel cross section (bottom) of seismicity along the central San Andreas Fault, with events colored by nFI. Well-constrained fault locations are plotted as dark gray lines, all others are light gray. Only M $\geq$ 2 events are shown. Cross-section events are projected onto the section line (A–A') from within $\pm$5 km. Shaded bands mark the fault's approximate segmentation (from *Liu et al.* (2022)): a central creeping section (Bitterwater to the San Andreas Fault Observatory at Depth [SAFOD]), flanking transition zones to the north and south, and locked sections beyond. The 2004 M 6.0 Parkfield earthquake is shown as a yellow star. Contours denote its finite-source slip model in decimeters, from *Ji et al.* (2004).

has sparse seismicity between the more active patches, this sparse seismicity tends to have higher nFI. The shallow cluster ($\sim$2–4 km) of low-nFI events below the central creeping section could be related to material properties. *Moore and Rymer* (2007) identified a large horizontal serpentinite body, extending approximately 45 km northwest from the San Andreas Fault Observatory at Depth (SAFOD). They suggest that talc, a mineral of very low shear strength, could be responsible for the creeping section. Whether this results in lower nFI, however, remains unclear.

We find no relation between slip from the 2004 Parkfield earthquake and nFI. Slip is determined from an interpolated finite-source model (*Ji et al.*, 2004) projected onto

A–A' (Fig. 4.13). This is consistent with findings of *Zhang et al.* (2022), who computed stress drops along the San Andreas fault and found no correlation with mainshock slip.

4.5.5 Temporal variation

At the statewide scale, we observe no clear temporal variation in average nFI in any region. Because nFI is computed relative to the average of small nearby calibration events occurring over the entire 30-year study period, it should be sensitive to temporal changes in absolute spectral ratios, i.e., to changes in the M 1.4–1.6 calibration event average spectral properties as well as to changes in relative spectral shapes. However, to test for robustness with respect to possible changes in network properties unrelated to source properties, we also performed nFI calculations in which calibration events were restricted to being within ± 180 days of the target events. This reduced the number of target events with the required 10 calibration events, but did not change the observed pattern of higher and lower nFI regions or introduce temporal variations.

At Parkfield, some studies have reported temporal variation in source parameters. *Allmann and Shearer* (2007) examined a section of the San Andreas Fault similar to that in Figure 4.13 and found resolvable temporal changes in stress drop in some fault patches following the 2004 Parkfield earthquake, but noted the large scatter in these measurements. *Abercrombie* (2014) also reported a gradual increase in stress drop within some earthquake clusters on the San Andreas Fault, followed by a drop after the 2004 Parkfield event. *Zhang et al.* (2022) found small amounts of temporal variation in the same area, but only on fault patches with higher numbers of well-recorded events, and noted the difficulty in interpreting these patterns because of the high uncertainty. Our nFI values exhibit apparent temporal variation on smaller scales, but the high variability of these measurements leaves our results inconclusive; resolving whether this variation is real will require further work.

4.5.6 Other possible sources of variation

Beyond those examined above, several other physical mechanisms have been proposed to explain spatial variability in high-frequency radiation. Explanations relating to interseismic fault healing have been proposed, which are supported by stress drop observations. Stress drop has been observed to correlate with recurrence time (e.g., *Kanamori and Allen*, 1986; *Marone et al.*, 1995; *Karner and Marone*, 2000) and shear strain rate (*Hauksson*, 2015). Intraplate earthquakes tend to have higher stress drops than interplate earthquakes near tectonic plate edges (*Kanamori and Anderson*, 1975). These observations have been interpreted as frictional strengthening during the interseismic period (*Kanamori and Allen*, 1986; *Marone et al.*, 1995). *Li et al.* (2003) found evidence of fault zone healing through an increase in wave velocity before and after the Hector Mine earthquake, but because of the difficulty in resolving temporal variation, it is unclear whether nFI could be used in this way.

Fault strength and maturity could also have a role in high-frequency variability, both of which have been proposed as controls on stress drop (*Cao and Aki*, 1986). *Manighetti et al.* (2007) reproduced the stress-drop versus maturity relationship with a model in which mature faults rupture as multiple linked segments. Numerical experiments have also shown that fault gouge reduces stress drop (*Mora and Place*, 1998). Rupture kinematics may contribute as well. In large earthquakes, stress drop anticorrelates with rupture velocity (*Chounet et al.*, 2018; *Causse and Song*, 2015), but this is difficult to measure in smaller earthquakes. Faulting style may also affect high-frequency variability; *Allmann and Shearer* (2009) observed that strike-slip earthquakes have higher stress drops on average, though this has not been universally observed (*Scholz et al.*, 1986).

Certain near-source conditions have also been proposed to affect high-frequency energy output rather than fault properties itself. Several studies document a change in high-frequency energy with depth (e.g., *Trugman*, 2020; *Hardebeck and Aron*, 2009),

though *Abercrombie et al.* (2021) showed that much of this trend may be an artifact of depth-dependent attenuation rather than a true source effect. Higher heat flow has been proposed to facilitate fault healing and correlate with stress drop in regions with low to medium heat flow (*Hauksson*, 2015), but regions of very high heat flow such as the Salton Trough and Coso Geothermal Field, conversely show lower average stress drops, consistent with our nFI estimates. Pore pressure likely also influences high-frequency content: reduced frequency content has been observed near fluid injection sites (*Salvage and Eaton*, 2022; *Goertz-Allmann et al.*, 2011) and in volcanic settings with elevated fluid pressures (e.g., *Chouet*, 1996), consistent with our nFI results in the Long Valley Caldera (Fig. 4.10).

4.6 Conclusions

We compute the normalized frequency index (nFI) for 30 years of California seismicity, producing the first statewide characterization of relative high-frequency source variability. The nFI measures the relative amount of high-frequency content in an earthquake, using small-magnitude calibration events near each target event to remove path and station effects. Because it requires few modeling assumptions concerning attenuation or earthquake rupture properties, nFI is not subject to spectral modeling bias and remains closely tied to observational data. The resulting spatial patterns are robust to nFI parameter choices and persist across two independently maintained catalogs, indicating that they reflect real variability rather than artifacts.

Our nFI values quantify the relative high-frequency radiation that contributes to ground motion, and they correlate with stress-drop estimates from previous studies, while being easier to compute across a catalog of this size. No single mechanism accounts for the observed variability, consistent with the large-scale stress drop comparison of *Hauksson* (2015). We do, however, resolve several robust associations. Our main findings are:

1. California exhibits both large-scale (on the order of hundreds of kilometers) and small-scale (on the order of a few kilometers) spatial variation in the relative high-frequency content of earthquakes. This variation is robust to the choice of magnitude correction and consistent between the NCEDC and SCEDC catalogs.

2. nFI correlates with independent stress drop estimates. While the scatter is high, nFI captures real variability in rupture mechanics but is not intended as a stress drop proxy.

3. Relative high-frequency content increases with depth: a sharp rise in the upper few kilometers is followed by a gradual increase to about 10–12 km. This depth dependence varies between regions but is, on average, a gradual increase.

4. Regions of high surface heat flow produce earthquakes with depleted high-frequency content, especially where heat flow is above 100–140 $\mathrm{mW/m^2}$. The geothermal and volcanic regions of the Geysers, Coso, Salton Trough, and Long Valley Caldera all produce earthquakes with less high-frequency content.

The statewide results presented here identify the regions and structures where this variability is concentrated. Some regions produce earthquakes with systematically stronger or weaker high-frequency amplitudes than average. Connecting these spatial patterns quantitatively to other geophysical parameters like velocity structure, fault maturity, and the presence of fluids remains the task of future work. In the near term, maps of median nFI could inform regionally varying stress-drop or high-frequency adjustments in ground motion models, offering a direct observational path toward improved hazard estimates.

4.7 Data Availability Statement

The installable *py-nfi* package used to compute nFI is available on GitHub (https://github.com/ivandevert/py-nfi). Scripts and Jupyter Notebooks that reproduce the

results and figures in this study are available in a separate GitHub repository (https://github.com/ivandevert/california-nfi).

The NCEDC and SCEDC earthquake catalogs, waveforms, and catalog picks used in this study are hosted in cloud repositories: the northern California dataset and metadata are described at https://ncedc.org/db/cloud.html (last accessed February 2026), and the southern California dataset and metadata are described at https://scedc.caltech.edu/data/cloud.html (last accessed February 2026). Station metadata are available through FDSN requests: https://service.ncedc.org/fdsnws/station/1/ and https://service.scedc.caltech.edu/fdsnws/station/1/ for the NCEDC and the SCEDC, respectively (last accessed February 2026).

The 1984–2021 northern California relocated earthquake catalog (*Waldhauser and Schaff*, 2008) is available at https://nocaldd.ldeo.columbia.edu/catalog/ (version NCAeqDD.v202112.1, last accessed 1 June 2026). The 1981–2025 southern California relocated catalog (*Hauksson et al.*, 2012) is available at https://scedc.caltech.edu/data/alt-2011-dd-hauksson-yang-shearer.html (last accessed 1 June 2026). Finite-source rupture models for the Hector Mine and 2004 Parkfield earthquakes are obtained from the SRCMOD database (*Mai and Thingbaijam*, 2014) located at http://equake-rc.info/srcmod (last accessed 31 May 2026).

Acknowledgments

Chapter 4, in full, is a reproduction of the material submitted to *Journal of Geophysical Research: Solid Earth*. Vandevert, I., Shearer, P. M., & Fan, W. (2026). Distinguishing Spatial Variations in California Earthquake Dynamics Using a High- to Low-Frequency Spectral Ratio.

Chapter 5

Conclusion

Earthquakes are among the most devastating of natural disasters, but their origins and properties are not fully understood despite years of study. Because earthquake ruptures initiate and and propagate at depths largely inaccessible to direct observation, seismologists rely on surface seismic recordings of their radiation. These seismograms are then interpreted in terms of theoretical source models, which are prone to high uncertainty (*Abercrombie*, 2021) and can introduce bias (*Abercrombie and Baltay*, 2025). There are many challenges to this process, notably oversimplified source models and uncertainties in path corrections (attenuation) between source and receiver.

Stress drop is the parameter conventionally invoked in explaining why some earthquakes produce more high-frequency energy than others, but the link between the two is indirect and often unreliable. Lacking more detailed knowledge, the earthquake rupture plane is often assumed circular with rupture occurring smoothly as an expanding crack. Assuming a fixed rupture velocity, P- and S-wave displacement spectra can be predicted as a function of seismic moment and stress drop. Thus, in principle, both moment and stress drop can be estimated from observed displacement spectra. However, stress drop estimates are highly model dependent, with complex crack geometries, rupture type (crack-like or pulse-like), rupture velocity, and rupture complexity affecting results. In general, ruptures with higher stress drop produce more high-frequency radiation, but earthquakes vary

widely in their properties and individual earthquake spectra often are much more irregular than the smooth spectra predicted by idealized models. It cannot safely be assumed that an earthquake that radiates more high-frequency energy than another earthquake of equal moment is a higher stress drop event.

Comparing observed spectra to source models requires correcting for path effects and attenuation, but these methods have tradeoffs and can be unstable. Theoretical models predict the seismic radiation leaving the source, but attenuation along the source-receiver path acts as a low-pass filter that preferentially removes high-frequency radiation. Thus, to compare observed spectra to source models, the lost high frequencies must be restored by correcting for path attenuation. Unfortunately, Earth's crustal attenuation structure is usually not known well enough to compute accurate corrections, forcing seismologists to apply empirical ones. These methods vary, but generally compare an event to one or more colocated earthquakes such that effects along the source-receiver path can be assumed identical, and impose assumptions about the expected form of the source spectra. Although widely applied for many years, it has recently been shown that these empirical approaches are unstable and have too many free parameters to yield stable attenuation corrections (*Shearer et al.*, 2019, 2024).

Given the uncertainties in both the appropriate physical source model and the size of attenuation corrections, it is not surprising that the recent Ridgecrest Stress Drop Validation Exercise (*Baltay et al.*, 2024; *Abercrombie et al.*, 2025a) showed widely different stress drop estimates among different groups and methods for the same earthquakes (e.g., *Vandevert et al.*, 2024; *Calderoni and Abercrombie*, 2024; *Bindi et al.*, 2025; *Knudson et al.*, 2025). However, the validation exercise suggested that the *relative* variations in stress drop between events were much better resolved. That is, if one group found that Event A has a much higher stress drop than Event B, then it is very likely that other groups would agree that the Event A stress drop is higher, regardless of any disagreements regarding the absolute value of the Event A stress drop. This suggests that variations

in high-frequency radiation among earthquakes are real even if stress drop for individual events cannot be reliably determined. The projects in this thesis are motivated by these results and aim to chart a new path forward.

Chapter 2 applies a stabilized version of the spectral decomposition method (similar to *Shearer et al.* (2022)) to the 2019 Ridgecrest, California, aftershock sequence of over 10,000 events and provides reliable stress drop differences over the entire Ridgecrest aftershock zone. Separate analyses using both P and S waves yield highly correlated results with similar spatial variations. Earthquakes near the Coso geothermal field tend to have lower stress drops, and earthquakes near the M 7.1 hypocenter have higher stress drops. However, we found no strong correlation between our stress-drop estimates and the M 7.1 Ridgecrest earthquake slip distribution, suggesting a complex, heterogeneous stress environment in this region.

Chapter 3 introduces a new empirical method to measure high-frequency radiation differences among earthquakes that is directly tied to the observations and requires no theoretical modeling assumptions. The method yields the normalized frequency index (nFI) for each earthquake, measuring relative differences in high-frequency radiation compared to the median for earthquakes of the same magnitude. These nFI are easy to compute and are ideally suited to the analysis of large sets that contain dense clouds of seismicity with many small earthquakes that can serve as calibration events to remove lateral differences in attenuation corrections. Although not intended as a proxy for stress drop, the nFI values are, unsurprisingly, correlated with stress-drop estimates for the Ridgecrest aftershocks.

Chapter 4 extends the nFI approach to over 750,000 California earthquakes spanning 30 years, revealing striking spatial variations in average nFI values that indicate systematic differences in earthquake radiation and dynamics. These variations correlate to varying degrees with heat flow, depth, focal mechanism, timing of last fault slip, and geothermal activity, suggesting a complex dependence on multiple geophysical processes.

The nFI values show no resolvable correlation with other parameters, such as strain rate, fault complexity, and maximum seismic depth. We did not observe any large-scale temporal variations, but there are suggestive but not conclusive smaller-scale variations. Regardless of their origin, our nFI results reveal spatially coherent differences in high-frequency radiation from earthquakes in many regions where such variations had not previously been observed.

Given the large scatter in individual earthquake source spectra, comprehensive analysis of large datasets using a consistent approach is essential for identifying robust variations in earthquake dynamics and linking them to other physical processes. To support this effort, we are making our nFI code publicly available for application to other earthquake catalogs and anticipate testing whether other seismically active regions, such as Japan, New Zealand, and Italy, exhibit spatial variations in earthquake radiation comparable to those seen in California.

Moving forward, we must develop new observational tools that keep pace with modeling advances. High-performance computing allows us to capture more of the rupture physics and dynamics of earthquakes (e.g., *Gabriel et al.*, 2024; *Kaneko et al.*, 2019), and new observational approaches can ensure these increasingly detailed models remain grounded in what we can measure. The existence of robust yet largely unexplained spatial variations in average spectral content in earthquake radiation points to unresolved questions in earthquake physics and motivates future work toward improving ground motion models.

Bibliography

Abercrombie R.E. (1995). Earthquake source scaling relationships from -1 to 5 ML using seismograms recorded at 2.5-km depth. *Journal of Geophysical Research: Solid Earth*, 100(B12):24015–24036. ISSN 2156-2202. doi: 10.1029/95JB02397.

Abercrombie R.E. (2014). Stress drops of repeating earthquakes on the San Andreas Fault at Parkfield. *Geophysical Research Letters*, 41(24):8784–8791. ISSN 1944-8007. doi: 10.1002/2014GL062079.

Abercrombie R.E. (2021). Resolution and uncertainties in estimates of earthquake stress drop and energy release. *Philosophical Transactions of the Royal Society A: Mathematical, Physical and Engineering Sciences*, 379(2196):20200131. doi: 10.1098/rsta.2020.0131.

Abercrombie R.E., Baltay A., Chu S., Taira T., Bindi D., Boyd O.S., Chen X., Cochran E.S., Devin E., Dreger D., Ellsworth W., Fan W., Harrington R.M., Huang Y., Kemna K.B., Liu M., Oth A., Parker G.A., Pennington C., Picozzi M., Ruhl C.J., Shearer P., Spallarossa D., Trugman D., Vandevert I., Wu Q., Yoon C., Yu E., Beroza G.C., Eulenfeld T., Knudson T., Mayeda K., Morasca P., Neely J.S., Roman-Nieves J., Satriano C., Supino M., Walter W.R., Archuleta R., Atkinson G.M., Calderoni G., Ji C., Yang H., and Zhang J. (2025a). Overview of the SCEC/USGS Community Stress Drop Validation Study using the 2019 Ridgecrest earthquake sequence. *Bulletin of the Seismological Society of America*, 115(3):734–759. ISSN 0037-1106. doi: 10.1785/0120240158.

Abercrombie R.E. and Baltay A.S. (2025). Magnitude, depth, and methodological variations of spectral stress drop within the SCEC/USGS Community Stress Drop Validation Study using the 2019 Ridgecrest earthquake sequence. *Bulletin of the Seismological Society of America*, 115(6):2741–2768. ISSN 0037-1106. doi: 10.1785/0120250056.

Abercrombie R.E., Bannister S., Ristau J., and Doser D. (2017). Variability of earthquake stress drop in a subduction setting, the Hikurangi Margin, New Zealand. *Geophysical Journal International*, 208(1):306–320. ISSN 0956-540X. doi: 10.1093/gji/ggw393.

Abercrombie R.E., Chen X., Huang Y., and Chu S. (2025b). Comparison of EGF methods for Ridgecrest sequence: Can EGFs help resolve ambiguity in isolating source spectra? *Bulletin of the Seismological Society of America*, 115(3):1132–1148. ISSN 0037-1106.

doi: 10.1785/0120240161.

Abercrombie R.E., Trugman D.T., Shearer P.M., Chen X., Zhang J., Pennington C.N., Hardebeck J.L., Goebel T.H.W., and Ruhl C.J. (2021). Does earthquake stress drop increase with depth in the crust? *Journal of Geophysical Research: Solid Earth*, 126(10):e2021JB022314. ISSN 2169-9356. doi: 10.1029/2021JB022314.

Ahn B.S., Kang T.S., and Yoo H.J. (2025). Source parameter estimation using site-corrected source spectra for the 2019 Ridgecrest earthquake sequence in southern California. *Bulletin of the Seismological Society of America*, 115(3):927–946. ISSN 0037-1106. doi: 10.1785/0120240157.

Aki K. (1967). Scaling law of seismic spectrum. *Journal of Geophysical Research (1896-1977)*, 72(4):1217–1231. ISSN 2156-2202. doi: 10.1029/JZ072i004p01217.

Allmann B.P. and Shearer P.M. (2007). Spatial and temporal stress drop variations in small earthquakes near Parkfield, California. *Journal of Geophysical Research: Solid Earth*, 112(B4). ISSN 2156-2202. doi: 10.1029/2006JB004395.

Allmann B.P. and Shearer P.M. (2009). Global variations of stress drop for moderate to large earthquakes. *Journal of Geophysical Research: Solid Earth*, 114(B1):1–22. ISSN 2156-2202. doi: 10.1029/2008JB005821.

Allmann B.P., Shearer P.M., and Hauksson E. (2008). Spectral discrimination between quarry blasts and earthquakes in southern California. *Bulletin of the Seismological Society of America*, 98(4):2073–2079. ISSN 0037-1106. doi: 10.1785/0120070215.

Anderson J.G. and Hough S.E. (1984). A model for the shape of the fourier amplitude spectrum of acceleration at high frequencies. *Bulletin of the Seismological Society of America*, 74(5):1969–1993. ISSN 0037-1106. doi: 10.1785/BSSA0740051969.

Andrews D.J. (1986). Objective determination of source parameters and similarity of earthquakes of different size. In S. Das, J. Boatwright, and C.H. Scholz, editors, *Earthquake Source Mechanics*, number 37 in Geophysical Monograph, pages 259–267. American Geophysical Union, Washington D.C. ISBN 978-1-118-66486-5. doi: 10.1029/GM037p0259.

Atkinson G.M. and Beresnev I. (1997). Don't call it stress drop. *Seismological Research Letters*, 68(1):3–4. ISSN 0895-0695. doi: 10.1785/gssrl.68.1.3.

Atkinson G.M. and Hanks T.C. (1995). A high-frequency magnitude scale. *Bulletin of the Seismological Society of America*, 85(3):825–833. ISSN 0037-1106. doi: 10.1785/BSSA0850030825.

Bailey R.A. (1989). Geologic map of Long Valley caldera.

Bailey R.A., Dalrymple G.B., and Lanphere M.A. (1976). Volcanism, structure, and geochronology of Long Valley Caldera, Mono County, California. *Journal of Geophysical Research (1896-1977)*, 81(5):725–744. ISSN 2156-2202. doi: 10.1029/JB081i005p00725.

Baltay A., Abercrombie R., Chu S., and Taira T. (2024). The SCEC/USGS community stress drop validation study using the 2019 Ridgecrest earthquake sequence. *Seismica*, 3(1):1–12. ISSN 2816-9387. doi: 10.26443/seismica.v3i1.1009.

Baltay A.S. and Hanks T.C. (2014). Understanding the magnitude dependence of PGA and PGV in NGA-West 2 data. *Bulletin of the Seismological Society of America*, 104(6):2851–2865. ISSN 0037-1106. doi: 10.1785/0120130283.

Baltay A.S., Hanks T.C., and Beroza G.C. (2013). Stable stress-drop measurements and their variability: Implications for ground-motion prediction. *Bulletin of the Seismological Society of America*, 103(1):211–222. ISSN 0037-1106. doi: 10.1785/0120120161.

Bindi D., Pacor F., Luzi L., Massa M., and Ameri G. (2009). The Mw 6.3, 2009 L'Aquila earthquake: Source, path and site effects from spectral analysis of strong motion data. *Geophysical Journal International*, 179(3):1573–1579. doi: 10.1111/j.1365-246X.2009.04392.x.

Bindi D., Picozzi M., Oth A., and Spallarossa D. (2025). Impact of seismic attenuation corrections on source parameter estimation. *Seismica*, 4(2). doi: 10.26443/seismica.v4i2.1651.

Bindi D., Razafindrakoto H.N.T., Picozzi M., and Oth A. (2021). Stress drop derived from spectral analysis considering the hypocentral depth in the attenuation model: Application to the Ridgecrest region, California. *Bulletin of the Seismological Society of America*, 111(6):3175–3188. ISSN 0037-1106. doi: 10.1785/0120210039.

Bindi D., Spallarossa D., Picozzi M., and Morasca P. (2020a). Reliability of source parameters for small events in central Italy: Insights from spectral decomposition analysis applied to both synthetic and real data. *Bulletin of the Seismological Society of America*, 110(6):3139–3157. ISSN 0037-1106. doi: 10.1785/0120200126.

Bindi D., Zaccarelli R., and Kotha S.R. (2020b). Local and moment magnitude analysis in the Ridgecrest region, California: Impact on interevent ground-motion variability. *Bulletin of the Seismological Society of America*, 111(1):339–355. ISSN 0037-1106. doi: 10.1785/0120200227.

Biondi E., Zhu W., Li J., Williams E.F., and Zhan Z. (2023). An upper-crust lid over the Long Valley magma chamber. *Science Advances*, 9(42):eadi9878. doi: 10.1126/sciadv.

adi9878.

Boatwright J. (1980). A spectral theory for circular seismic sources; simple estimates of source dimension, dynamic stress drop, and radiated seismic energy. *Bulletin of the Seismological Society of America*, 70(1):1–27. ISSN 0037-1106. doi: 10.1785/BSSA0700010001.

Boore D.M. (1983). Stochastic simulation of high-frequency ground motions based on seismological models of the radiated spectra. *Bulletin of the Seismological Society of America*, 73(6A):1865–1894. ISSN 0037-1106. doi: 10.1785/BSSA07306A1865.

Boyd O.S., McNamara D.E., Hartzell S., and Choy G. (2017). Influence of lithostatic stress on earthquake stress drops in North America. *Bulletin of the Seismological Society of America*, 107(2):856–868. ISSN 0037-1106. doi: 10.1785/0120160219.

Brune J.N. (1970). Tectonic stress and the spectra of seismic shear waves from earthquakes. *Journal of Geophysical Research (1896-1977)*, 75(26):4997–5009. ISSN 2156-2202. doi: 10.1029/JB075i026p04997.

Buurman H., West M.E., and Power J.A. (2010). Seismic precursors to volcanic explosions during the 2006 eruption of Augustine Volcano. In J.A. Power, M.L. Coombs, and J.T. Freymueller, editors, *The 2006 Eruption of Augustine Volcano, Alaska*, number 1769 in U.S. Geological Survey Professional Paper, pages 41–57. U.S. Geological Survey, Reston, VA.

Calderoni G. and Abercrombie R.E. (2024). Combining two distinct methods to resolve spatial variation in attenuation and earthquake source parameters. *Bulletin of the Seismological Society of America*, 115(3):875–889. ISSN 0037-1106. doi: 10.1785/0120240160.

Cao T. and Aki K. (1986). Effect of slip rate on stress drop. *pure and applied geophysics*, 124(3):515–529. ISSN 1420-9136. doi: 10.1007/BF00877214.

Causse M. and Song S.G. (2015). Are stress drop and rupture velocity of earthquakes independent? Insight from observed ground motion variability. *Geophysical Research Letters*, 42(18):7383–7389. ISSN 1944-8007. doi: 10.1002/2015GL064793.

Chen K., Avouac J.P., Aati S., Milliner C., Zheng F., and Shi C. (2020). Cascading and pulse-like ruptures during the 2019 Ridgecrest earthquakes in the Eastern California Shear Zone. *Nature Communications*, 11(1):22. ISSN 2041-1723. doi: 10.1038/s41467-019-13750-w.

Chen X. and Abercrombie R.E. (2020). Improved approach for stress drop estimation and its application to an induced earthquake sequence in Oklahoma. *Geophysical Journal*

International, 223(1):233–253. ISSN 0956-540X. doi: 10.1093/gji/ggaa316.

Chen X. and Shearer P.M. (2013). California foreshock sequences suggest aseismic triggering process. *Geophysical Research Letters*, 40(11):2602–2607. ISSN 1944-8007. doi: 10.1002/grl.50444.

Cheng Y., Bürgmann R., Allen R.M., Taira T., and Liao Z. (2025). Stress model of California: Interaction between faults and stress along the transform boundary inferred from focal mechanisms of small earthquakes. *ESS Open Archive*. doi: 10.22541/essoar.175104974.48345381/v1.

Chouet B.A. (1996). Long-period volcano seismicity: Its source and use in eruption forecasting. *Nature*, 380(6572):309–316. ISSN 1476-4687. doi: 10.1038/380309a0.

Chounet A., Vallée M., Causse M., and Courboulex F. (2018). Global catalog of earthquake rupture velocities shows anticorrelation between stress drop and rupture velocity. *Tectonophysics*, 733:148–158. ISSN 0040-1951. doi: 10.1016/j.tecto.2017.11.005.

Cotton F., Archuleta R., and Causse M. (2013). What is sigma of the stress drop? *Seismological Research Letters*, 84(1):42–48. ISSN 0895-0695. doi: 10.1785/0220120087.

Das S. and Henry C. (2003). Spatial relation between main earthquake slip and its aftershock distribution. *Reviews of Geophysics*, 41(3). ISSN 1944-9208. doi: 10.1029/2002RG000119.

Denolle M.A. and Shearer P.M. (2016). New perspectives on self-similarity for shallow thrust earthquakes. *Journal of Geophysical Research: Solid Earth*, 121(9):6533–6565. ISSN 2169-9356. doi: 10.1002/2016JB013105.

Doocy S., Daniels A., Packer C., Dick A., and Kirsch T.D. (2013). The human impact of earthquakes: A historical review of events 1980-2009 and systematic literature review. *PLoS Currents*, 5:ecurrents.dis.67bd14fe457f1db0b5433a8ee20fb833. ISSN 2157-3999. doi: 10.1371/currents.dis.67bd14fe457f1db0b5433a8ee20fb833.

DuRoss C.B., Gold R.D., Dawson T.E., Scharer K.M., Kendrick K.J., Akciz S.O., Angster S.J., Bachhuber J., Bacon S., Bennett S.E.K., Blair L., Brooks B.A., Bullard T., Burgess W.P., Chupik C., DeFrisco M., Delano J., Dolan J.F., Frost E., Graehl N., Haddon E.K., Hatem A.E., Hernandez J.L., Hitchcock C., Hudnut K., Thompson Jobe J., Koehler R., Kozaci O., Ladinsky T., Madugo C., McPhillips D.S., Milliner C., Morelan A., Olson B., Patton J., Philibosian B., Pickering A.J., Pierce I., Ponti D.J., Seitz G., Spangler E., Swanson B., Thomas K., Treiman J., Valencia F., Williams A., and Zinke R. (2020). Surface displacement distributions for the July 2019 Ridgecrest, California, earthquake ruptures. *Bulletin of the Seismological Society of America*, 110(4):1400–1418. ISSN 0037-1106. doi: 10.1785/0120200058.

Eshelby J.D. (1957). The determination of the elastic field of an ellipsoidal inclusion, and related problems. *Proceedings of the Royal Society of London. Series A. Mathematical and Physical Sciences*, 241(1226):376–396. ISSN 0080-4630, 2053-9169. doi: 10.1098/rspa.1957.0133.

Fan W. and McGuire J.J. (2018). Investigating microearthquake finite source attributes with IRIS community wavefield demonstration experiment in Oklahoma. *Geophysical Journal International*, 214(2):1072–1087. ISSN 0956-540X. doi: 10.1093/gji/ggy203.

Field E.H., Arrowsmith R.J., Biasi G.P., Bird P., Dawson T.E., Felzer K.R., Jackson D.D., Johnson K.M., Jordan T.H., Madden C., Michael A.J., Milner K.R., Page M.T., Parsons T., Powers P.M., Shaw B.E., Thatcher W.R., Weldon II R.J., and Zeng Y. (2014). Uniform California Earthquake Rupture Forecast, Version 3 (UCERF3)—The Time-Independent Model. *Bulletin of the Seismological Society of America*, 104(3):1122–1180. ISSN 0037-1106. doi: 10.1785/0120130164.

Folesky J., Pennington C.N., Kummerow J., and Hofman L.J. (2024). A comprehensive stress drop map from trench to depth in the northern Chilean subduction zone. *Journal of Geophysical Research: Solid Earth*, 129(1):e2023JB027549. ISSN 2169-9356. doi: 10.1029/2023JB027549.

Fryzlewicz P. (2014). Wild binary segmentation for multiple change-point detection. *The Annals of Statistics*, 42(6):2243–2281. ISSN 0090-5364, 2168-8966. doi: 10.1214/14-AOS1245.

Gabriel A.A., Garagash D.I., Palgunadi K.H., and Mai P.M. (2024). Fault size–dependent fracture energy explains multiscale seismicity and cascading earthquakes. *Science*, 385(6707):eadj9587. doi: 10.1126/science.adj9587.

Goebel T., Hauksson E., Shearer P., and Ampuero J. (2015). Stress-drop heterogeneity within tectonically complex regions: A case study of San Gorgonio pass, southern California. *Geophysical Journal International*, 202(1):514–528. ISSN 0956-540X. doi: 10.1093/gji/ggv160.

Goertz-Allmann B.P., Goertz A., and Wiemer S. (2011). Stress drop variations of induced earthquakes at the Basel geothermal site. *Geophysical Research Letters*, 38(9). ISSN 1944-8007. doi: 10.1029/2011GL047498.

Hadley D. and Kanamori H. (1977). Seismic structure of the transverse ranges, California. *GSA Bulletin*, 88(10):1469–1478. ISSN 0016-7606. doi: 10.1130/0016-7606(1977)88⟨1469:SSOTTR⟩2.0.CO;2.

Hanks T.C. (1979). B values and $\omega - \gamma$ seismic source models: Implications for tectonic stress variations along active crustal fault zones and the estimation of high-frequency

strong ground motion. *Journal of Geophysical Research: Solid Earth*, 84(B5):2235–2242. ISSN 2156-2202. doi: 10.1029/JB084iB05p02235.

Hanks T.C. and Kanamori H. (1979). A moment magnitude scale. *Journal of Geophysical Research: Solid Earth*, 84(B5):2348–2350. ISSN 2156-2202. doi: 10.1029/JB084iB05p02348.

Hanks T.C. and McGuire R.K. (1981). The character of high-frequency strong ground motion. *Bulletin of the Seismological Society of America*, 71(6):2071–2095. ISSN 0037-1106. doi: 10.1785/BSSA0710062071.

Hardebeck J.L. (2020). Are the stress drops of small earthquakes good predictors of the stress drops of moderate-to-large earthquakes? *Journal of Geophysical Research: Solid Earth*, 125(3):e2019JB018831. ISSN 2169-9356. doi: 10.1029/2019JB018831.

Hardebeck J.L. and Aron A. (2009). Earthquake stress drops and inferred fault strength on the Hayward fault, east San Francisco Bay, California. *Bulletin of the Seismological Society of America*, 99(3):1801–1814. ISSN 0037-1106. doi: 10.1785/0120080242.

Harris R.A. (1998). Introduction to special section: Stress triggers, stress shadows, and implications for seismic hazard. *Journal of Geophysical Research: Solid Earth*, 103(B10):24347–24358. ISSN 2156-2202. doi: 10.1029/98JB01576.

Hauksson E. (2015). Average stress drops of southern California earthquakes in the context of crustal geophysics: Implications for fault zone healing. *Pure and Applied Geophysics*, 172(5):1359–1370. ISSN 1420-9136. doi: 10.1007/s00024-014-0934-4.

Hauksson E., Jones L.M., and Hutton K. (2002). The 1999 Mw 7.1 Hector Mine, California, earthquake sequence: Complex conjugate strike-slip faulting. *Bulletin of the Seismological Society of America*, 92(4):1154–1170. ISSN 0037-1106. doi: 10.1785/0120000920.

Hauksson E., Yang W., and Shearer P.M. (2012). Waveform relocated earthquake catalog for southern California (1981 to June 2011). *Bulletin of the Seismological Society of America*, 102(5):2239–2244. ISSN 0037-1106. doi: 10.1785/0120120010.

Hough S.E. (1997). Empirical Green's function analysis: Taking the next step. *Journal of Geophysical Research: Solid Earth*, 102(B3):5369–5384. ISSN 2156-2202. doi: 10.1029/96JB03488.

Huang Y., Beroza G.C., and Ellsworth W.L. (2016). Stress drop estimates of potentially induced earthquakes in the Guy-Greenbrier sequence. *Journal of Geophysical Research: Solid Earth*, 121(9):6597–6607. ISSN 2169-9356. doi: 10.1002/2016JB013067.

Huang Y., Ellsworth W.L., and Beroza G.C. (2017). Stress drops of induced and tectonic

earthquakes in the central United States are indistinguishable. *Science Advances*, 3(8):e1700772. doi: 10.1126/sciadv.1700772.

Ji C. and Archuleta R.J. (2022). A source physics interpretation of nonself-similar double-corner-frequency source spectral model JA19_2S. *Seismological Research Letters*, 93(2A):777–786. ISSN 0895-0695. doi: 10.1785/0220210098.

Ji C., Choi K.K., King N., Larson K.M., and Hudnut K.W. (2004). Co-seismic slip history and early afterslip of the 2004 Parkfield earthquake. In *AGU Fall Meeting Abstracts*, volume 2004, pages S53D–04. San Francisco, CA.

Ji C., Wald D.J., and Helmberger D.V. (2002). Source Description of the 1999 Hector Mine, California, earthquake, part II: Complexity of slip history. *Bulletin of the Seismological Society of America*, 92(4):1208–1226. ISSN 0037-1106. doi: 10.1785/0120000917.

Jin Z. and Fialko Y. (2020). Finite slip models of the 2019 Ridgecrest earthquake sequence constrained by space geodetic data and aftershock locations. *Bulletin of the Seismological Society of America*, 110(4):1660–1679. ISSN 0037-1106. doi: 10.1785/0120200060.

Kanamori H. (1977). The energy release in great earthquakes. *Journal of Geophysical Research (1896-1977)*, 82(20):2981–2987. ISSN 2156-2202. doi: 10.1029/JB082i020p02981.

Kanamori H. and Allen C.R. (1986). Earthquake repeat time and average stress drop. In S. Das, J. Boatwright, and C.H. Scholz, editors, *Earthquake Source Mechanics*, number 37 in Geophysical Monograph, pages 227–235. American Geophysical Union, Washington D.C. ISBN 978-1-118-66486-5. doi: 10.1029/GM037p0227.

Kanamori H. and Anderson D.L. (1975). Theoretical basis of some empirical relations in seismology. *Bulletin of the Seismological Society of America*, 65(5):1073–1095. ISSN 0037-1106. doi: 10.1785/BSSA0650051073.

Kaneko Y., Ito Y., Chow B., Wallace L.M., Tape C., Grapenthin R., D'Anastasio E., Henrys S., and Hino R. (2019). Ultra-long duration of seismic ground motion arising from a thick, low-velocity sedimentary wedge. *Journal of Geophysical Research: Solid Earth*, 124(10):10347–10359. ISSN 2169-9356. doi: 10.1029/2019JB017795.

Kaneko Y. and Shearer P.M. (2014). Seismic source spectra and estimated stress drop derived from cohesive-zone models of circular subshear rupture. *Geophysical Journal International*, 197(2):1002–1015. doi: 10.1093/gji/ggu030.

Karner S.L. and Marone C. (2000). Effects of loading rate and normal stress on stress drop and stick-slip recurrence interval. In J.B. Rundle, D.L. Turcotte, and W. Klein, editors, *Geocomplexity and the Physics of Earthquakes*, number 120 in Geophysical Monograph, pages 187–198. American Geophysical Union, Washington D.C. ISBN 978-1-118-66837-5.

doi: 10.1029/GM120p0187.

Ketner D. and Power J. (2013). Characterization of seismic events during the 2009 eruption of Redoubt Volcano, Alaska. *Journal of Volcanology and Geothermal Research*, 259:45–62. ISSN 0377-0273. doi: 10.1016/j.jvolgeores.2012.10.007.

Knudson T.C., Ellsworth W.L., and Beroza G.C. (2025). Source parameter analysis using maximum amplitudes in the time domain. *Bulletin of the Seismological Society of America*, 115(3):839–849. ISSN 0037-1106. doi: 10.1785/0120240198.

Li Y.G., Vidale J.E., Day S.M., Oglesby D.D., and Cochran E. (2003). Postseismic fault healing on the rupture zone of the 1999 M 7.1 Hector Mine, California, earthquake. *Bulletin of the Seismological Society of America*, 93(2):854–869. ISSN 0037-1106. doi: 10.1785/0120020131.

Lin G. and Fan W. (2024). Spatiotemporal variations of in situ Vp/Vs ratios during the 2019 Ridgecrest earthquake sequence suggest fault zone condition changes. *Geophysical Research Letters*, 51(10):e2024GL109171. ISSN 1944-8007. doi: 10.1029/2024GL109171.

Lior I. and Ziv A. (2017). The relation between ground acceleration and earthquake source parameters: Theory and observations. *Bulletin of the Seismological Society of America*, 107(2):1012–1018. ISSN 0037-1106. doi: 10.1785/0120160251.

Liu C., Lay T., Brodsky E.E., Dascher-Cousineau K., and Xiong X. (2019). Coseismic rupture process of the large 2019 Ridgecrest earthquakes from joint inversion of geodetic and seismological observations. *Geophysical Research Letters*, 46(21):11820–11829. ISSN 1944-8007. doi: 10.1029/2019GL084949.

Liu M., Huang Y., and Ritsema J. (2020). Stress drop variation of deep-focus earthquakes based on empirical Green's functions. *Geophysical Research Letters*, 47(9):e2019GL086055. ISSN 1944-8007. doi: 10.1029/2019GL086055.

Liu Y.K., Ross Z.E., Cochran E.S., and Lapusta N. (2022). A unified perspective of seismicity and fault coupling along the San Andreas Fault. *Science Advances*, 8(8):eabk1167. doi: 10.1126/sciadv.abk1167.

Lucazeau F. (2019). Analysis and mapping of an updated terrestrial heat flow data set. *Geochemistry, Geophysics, Geosystems*, 20(8):4001–4024. ISSN 1525-2027. doi: 10.1029/2019GC008389.

Madariaga R. (1976). Dynamics of an expanding circular fault. *Bulletin of the Seismological Society of America*, 66(3):639–666. ISSN 0037-1106. doi: 10.1785/BSSA0660030639.

Mai P.M. and Thingbaijam K.K.S. (2014). SRCMOD: An online database of finite-fault

rupture models. *Seismological Research Letters*, 85(6):1348–1357. ISSN 0895-0695. doi: 10.1785/0220140077.

Manighetti I., Campillo M., Bouley S., and Cotton F. (2007). Earthquake scaling, fault segmentation, and structural maturity. *Earth and Planetary Science Letters*, 253(3):429–438. ISSN 0012-821X. doi: 10.1016/j.epsl.2006.11.004.

Marone C. (1998). Laboratory-derived friction laws and their application to seismic faulting. *Annual Review of Earth and Planetary Sciences*, 26(Volume 26, 1998):643–696. ISSN 0084-6597, 1545-4495. doi: 10.1146/annurev.earth.26.1.643.

Marone C., Vidale J.E., and Ellsworth W.L. (1995). Fault healing inferred from time dependent variations in source properties of repeating earthquakes. *Geophysical Research Letters*, 22(22):3095–3098. ISSN 1944-8007. doi: 10.1029/95GL03076.

Matoza R.S., Shearer P.M., and Okubo P.G. (2014). High-precision relocation of long-period events beneath the summit region of Kilauea Volcano, Hawai'i, from 1986 to 2009. *Geophysical Research Letters*, 41(10):3413–3421. ISSN 1944-8007. doi: 10.1002/2014GL059819.

Moore D.E. and Rymer M.J. (2007). Talc-bearing serpentinite and the creeping section of the San Andreas Fault. *Nature*, 448(7155):795–797. ISSN 1476-4687. doi: 10.1038/nature06064.

Mora P. and Place D. (1998). Numerical simulation of earthquake faults with gouge: Toward a comprehensive explanation for the heat flow paradox. *Journal of Geophysical Research: Solid Earth*, 103(B9):21067–21089. ISSN 2156-2202. doi: 10.1029/98JB01490.

Mueller C.S. (1985). Source pulse enhancement by deconvolution of an empirical Green's function. *Geophysical Research Letters*, 12(1):33–36. ISSN 1944-8007. doi: 10.1029/GL012i001p00033.

Nakajima J. and Hasegawa A. (2021). Prevalence of shallow low-frequency earthquakes in the continental crust. *Journal of Geophysical Research: Solid Earth*, 126(4):e2020JB021391. ISSN 2169-9356. doi: 10.1029/2020JB021391.

NCEDC (2014). Northern California Earthquake Data Center. doi: 10.7932/NCEDC.

Oth A., Bindi D., Parolai S., and Di Giacomo D. (2011). Spectral analysis of k-NET and KiK-net data in Japan, part II: On attenuation characteristics, source spectra, and site response of borehole and surface stations. *Bulletin of the Seismological Society of America*, 101(2):667–687. ISSN 0037-1106. doi: 10.1785/0120100135.

Oth A., Bindi D., Parolai S., and Wenzel F. (2008). S-wave attenuation characteristics

beneath the Vrancea region in Romania: New insights from the inversion of ground-motion spectra. *Bulletin of the Seismological Society of America*, 98(5):2482–2497. ISSN 0037-1106. doi: 10.1785/0120080106.

Parker G.A., Baltay A.S., Rekoske J., and Thompson E.M. (2020). Repeatable source, path, and site effects from the 2019 M 7.1 Ridgecrest earthquake sequence. *Bulletin of the Seismological Society of America*, 110(4):1530–1548. ISSN 0037-1106. doi: 10.1785/0120200008.

Pennington C.N., Chen X., Abercrombie R.E., and Wu Q. (2021). Cross validation of stress drop estimates and interpretations for the 2011 Prague, OK, earthquake sequence using multiple methods. *Journal of Geophysical Research: Solid Earth*, 126(3):e2020JB020888. ISSN 2169-9356. doi: 10.1029/2020JB020888.

Pinilla-Ramos C.I., Abrahamson N.A., Marcou S., Dreger D.S., Savvaidis A., Atkinson G.M., Hassani B., Sung C.H., and Youngs R. (2026). Examining the causes of regional differences in California based on ground motions from small to moderate earthquakes. *Bulletin of the Seismological Society of America*, 116(3):1145–1160. ISSN 0037-1106. doi: 10.1785/0120250239.

Prieto G.A. (2022). The multitaper spectrum analysis package in Python. *Seismological Research Letters*, 93(3):1922–1929. ISSN 0895-0695. doi: 10.1785/0220210332.

Prieto G.A., Parker R.L., Thomson D.J., Vernon F.L., and Graham R.L. (2007). Reducing the bias of multitaper spectrum estimates. *Geophysical Journal International*, 171(3):1269–1281. ISSN 0956-540X. doi: 10.1111/j.1365-246X.2007.03592.x.

Prieto G.A., Parker R.L., and Vernon III F.L. (2009). A Fortran 90 library for multitaper spectrum analysis. *Computers & Geosciences*, 35(8):1701–1710. ISSN 0098-3004. doi: 10.1016/j.cageo.2008.06.007.

Prieto G.A., Shearer P.M., Vernon F.L., and Kilb D. (2004). Earthquake source scaling and self-similarity estimation from stacking P and S spectra. *Journal of Geophysical Research: Solid Earth*, 109(B8):1–13. ISSN 2156-2202. doi: 10.1029/2004JB003084.

Richter C.F. (1935). An instrumental earthquake magnitude scale*. *Bulletin of the Seismological Society of America*, 25(1):1–32. ISSN 0037-1106. doi: 10.1785/BSSA0250010001.

Ross Z.E., Ben-Zion Y., White M.C., and Vernon F.L. (2016). Analysis of earthquake body wave spectra for potency and magnitude values: Implications for magnitude scaling relations. *Geophysical Journal International*, 207(2):1158–1164. ISSN 0956-540X. doi: 10.1093/gji/ggw327.

Ross Z.E., Idini B., Jia Z., Stephenson O.L., Zhong M., Wang X., Zhan Z., Simons

M., Fielding E.J., Yun S.H., Hauksson E., Moore A.W., Liu Z., and Jung J. (2019). Hierarchical interlocked orthogonal faulting in the 2019 Ridgecrest earthquake sequence. *Science*, 366(6463):346–351. doi: 10.1126/science.aaz0109.

Ruhl C.J., Abercrombie R.E., and Shearer P.M. (2023). Spatially consistent small-scale stress heterogeneity revealed by the 2008 Mogul, Nevada, earthquakes. *The Seismic Record*, 3(3):239–248. ISSN 2694-4006. doi: 10.1785/0320230026.

Salvage R.O. and Eaton D.W. (2022). The influence of a transitional stress regime on the source characteristics of induced seismicity and fault activation: Evidence from the 30 November 2018 Fort St. John ML 4.5 induced earthquake sequence. *Bulletin of the Seismological Society of America*, 112(3):1336–1355. ISSN 0037-1106. doi: 10.1785/0120210210.

SCEDC (2013). Southern California Earthquake Data Center. doi: 10.7909/C3WD3xH1.

Scholz C.H., Aviles C.A., and Wesnousky S.G. (1986). Scaling differences between large interplate and intraplate earthquakes. *Bulletin of the Seismological Society of America*, 76(1):65–70. ISSN 0037-1106. doi: 10.1785/BSSA0760010065.

Shaw B.E., Ellsworth W.L., Yoshimitsu N., Huang Y., and Beroza G.C. (2016). Precise relative stress drops.

Shearer P.M. (2019). *Introduction to Seismology*. Cambridge University Press, Cambridge, U.K. ISBN 978-1-107-18447-3.

Shearer P.M. and Abercrombie R.E. (2021). Calibrating spectral decomposition of local earthquakes using borehole seismic records—results for the 1992 Big Bear aftershocks in southern California. *Journal of Geophysical Research: Solid Earth*, 126(3):e2020JB020561. ISSN 2169-9356. doi: 10.1029/2020JB020561.

Shearer P.M., Abercrombie R.E., and Trugman D.T. (2022). Improved stress drop estimates for M 1.5 to 4 earthquakes in southern California from 1996 to 2019. *Journal of Geophysical Research: Solid Earth*, 127(7):e2022JB024243. ISSN 2169-9356. doi: 10.1029/2022JB024243.

Shearer P.M., Abercrombie R.E., Trugman D.T., and Wang W. (2019). Comparing EGF methods for estimating corner frequency and stress drop from P wave spectra. *Journal of Geophysical Research: Solid Earth*, 124(4):3966–3986. ISSN 2169-9356. doi: 10.1029/2018JB016957.

Shearer P.M., Prieto G.A., and Hauksson E. (2006). Comprehensive analysis of earthquake source spectra in southern California. *Journal of Geophysical Research: Solid Earth*, 111(B6):1–21. ISSN 2156-2202. doi: 10.1029/2005JB003979.

Shearer P.M., Vandevert I., Fan W., Abercrombie R.E., Bindi D., Calderoni G., Chen X., Ellsworth W., Harrington R., Huang Y., Knudson T., Roßbach M., Satriano C., Supino M., Trugman D.T., Yang H., and Zhang J. (2024). Earthquake source spectra estimates vary widely for two Ridgecrest aftershocks because of differences in attenuation corrections. *Bulletin of the Seismological Society of America*, 115(3):777–791. ISSN 0037-1106. doi: 10.1785/0120240134.

Shimmoto S. (2022). Stress drop estimates for small to moderate earthquakes in Tohoku, Japan considering rupture geometry, speed, and directivity. *Journal of Geophysical Research: Solid Earth*, 127(8):e2022JB025157. ISSN 2169-9356. doi: 10.1029/2022JB025157.

Sundod C. (2024). *First identification and characterization of long-period earthquakes in the Larderello-Travale Geothermal field*. Ph.D. thesis, University of Padua, Padua, Italy.

Trugman D.T. (2020). Stress-drop and source scaling of the 2019 Ridgecrest, California, earthquake sequence. *Bulletin of the Seismological Society of America*, 110(4):1859–1871. ISSN 0037-1106. doi: 10.1785/0120200009.

Trugman D.T. and Shearer P.M. (2017a). Application of an improved spectral decomposition method to examine earthquake source scaling in southern California. *Journal of Geophysical Research: Solid Earth*, 122(4):2890–2910. ISSN 2169-9356. doi: 10.1002/2017JB013971.

Trugman D.T. and Shearer P.M. (2017b). GrowClust: A hierarchical clustering algorithm for relative earthquake relocation, with application to the Spanish Springs and Sheldon, Nevada, earthquake sequences. *Seismological Research Letters*, 88(2A):379–391. ISSN 0895-0695. doi: 10.1785/0220160188.

Trugman D.T. and Shearer P.M. (2018). Strong correlation between stress drop and peak ground acceleration for recent M 1–4 earthquakes in the San Francisco Bay area. *Bulletin of the Seismological Society of America*, 108(2):929–945. ISSN 0037-1106. doi: 10.1785/0120170245.

Tsuchiyama A., Taira T., Nakajima J., and Bürgmann R. (2022). Emergence of low-frequency aftershocks of the 2019 Ridgecrest earthquake sequence. *Bulletin of the Seismological Society of America*, 112(2):750–762. ISSN 0037-1106. doi: 10.1785/0120210206.

Utsu T. (2002a). Relationships between magnitude scales. In W.H.K. Lee, H. Kanamori, P.C. Jennings, and C. Kisslinger, editors, *International Geophysics*, volume 81 of *International Handbook of Earthquake and Engineering Seismology, Part A*, pages 733–746. Academic Press, San Diego, CA. doi: 10.1016/S0074-6142(02)80247-9.

Utsu T. (2002b). Statistical features of seismicity. In W.H.K. Lee, H. Kanamori, P.C. Jennings, and C. Kisslinger, editors, *International Geophysics*, volume 81 of *International Handbook of Earthquake and Engineering Seismology, Part A*, pages 719–732. Academic Press, San Diego, CA. doi: 10.1016/S0074-6142(02)80246-7.

Vandevert I., Shearer P.M., and Fan W. (2024). Ridgecrest aftershock stress drops from P- and S-wave spectral decomposition. *Bulletin of the Seismological Society of America*, 115(3):792–804. ISSN 0037-1106. doi: 10.1785/0120240133.

Vandevert I., Shearer P.M., and Fan W. (2026). Using a high- to low-frequency spectral ratio to distinguish variations in earthquake source properties. *Bulletin of the Seismological Society of America*. doi: 10.1785/0120250171.

Waldhauser F. and Schaff D.P. (2008). Large-scale relocation of two decades of northern California seismicity using cross-correlation and double-difference methods. *Journal of Geophysical Research: Solid Earth*, 113(B8). ISSN 2156-2202. doi: 10.1029/2007JB005479.

Wang K., Dreger D.S., Tinti E., Bürgmann R., and Taira T. (2020). Rupture process of the 2019 Ridgecrest, California Mw 6.4 foreshock and Mw 7.1 earthquake constrained by seismic and geodetic data. *Bulletin of the Seismological Society of America*, 110(4):1603–1626. ISSN 0037-1106. doi: 10.1785/0120200108.

Wesnousky S.G. (1986). Earthquakes, quaternary faults, and seismic hazard in California. *Journal of Geophysical Research: Solid Earth*, 91(B12):12587–12631. ISSN 2156-2202. doi: 10.1029/JB091iB12p12587.

Woessner J., Schorlemmer D., Wiemer S., and Mai P.M. (2006). Spatial correlation of aftershock locations and on-fault main shock properties. *Journal of Geophysical Research: Solid Earth*, 111(B8). ISSN 2156-2202. doi: 10.1029/2005JB003961.

Xu X., Sandwell D.T., and Smith-Konter B. (2020). Coseismic displacements and surface fractures from Sentinel-1 InSAR: 2019 Ridgecrest earthquakes. *Seismological Research Letters*, 91(4):1979–1985. ISSN 0895-0695. doi: 10.1785/0220190275.

Yenier E. and Atkinson G.M. (2014). Equivalent point-source modeling of moderate-to-large magnitude earthquakes and associated ground-motion saturation effects. *Bulletin of the Seismological Society of America*, 104(3):1458–1478. ISSN 0037-1106. doi: 10.1785/0120130147.

Yoon C.E., Yoshimitsu N., Ellsworth W.L., and Beroza G.C. (2019). Foreshocks and mainshock nucleation of the 1999 Mw 7.1 Hector Mine, California, earthquake. *Journal of Geophysical Research: Solid Earth*, 124(2):1569–1582. ISSN 2169-9356. doi: 10.1029/2018JB016383.

Yue H., Sun J., Wang M., Shen Z., Li M., Xue L., Lu W., Zhou Y., Ren C., and Lay T. (2021). The 2019 Ridgecrest, California earthquake sequence: Evolution of seismic and aseismic slip on an orthogonal fault system. *Earth and Planetary Science Letters*, 570:117066. ISSN 0012-821X. doi: 10.1016/j.epsl.2021.117066.

Zhang J., Chen X., and Abercrombie R.E. (2022). Spatiotemporal variability of earthquake source parameters at Parkfield, California, and their relationship with the 2004 M6 earthquake. *Journal of Geophysical Research: Solid Earth*, 127(6):e2021JB022851. ISSN 2169-9356. doi: 10.1029/2021JB022851.

Zhang Q. and Lin G. (2014). Three-dimensional Vp and Vp/Vs models in the Coso geothermal area, California: Seismic characterization of the magmatic system. *Journal of Geophysical Research: Solid Earth*, 119(6):4907–4922. ISSN 2169-9356. doi: 10.1002/2014JB010992.